# DESIGN AND OPTIMIZATION OF A MULTI-PARTICLE ACCELERATOR BEAM TRANSPORT AND DELIVERY SYSTEM FOR MATERIAL IRRADIATION IN NUCLEAR AND FUSION SCIENCE

By

Tyler Christopher Sordelet

B.S., Mechanical Engineering (2010)

United States Naval Academy

ARCHIVES

MASSACHUSETTS INSTITUTE OF TECHNOLOGY

JUL 25 2012

LIBRARIES

SUBMITTED TO THE DEPARTMENT OF NUCLEAR SCIENCE
AND ENGINEERING
IN PARTIAL FULFILLMENT OF THE REQUIREMENTS FOR THE DEGREE OF

MASTER'S OF SCIENCE IN NUCLEAR SCIENCE AND ENGINEERING
AT THE
MASSACHUSETTS INSTITUTE OF TECHNOLOGY

DECEMBER 2011

[February 2012]

© 2011 Massachusetts Institute of Technology
All rights reserved

Signature of Author_____
Tyler Christopher Sordelet
Department of Nuclear Science and Engineering
December 15, 2011

Certified by_____
Ronald Ballinger, Sc.D.
Professor, Nuclear and Material Science and Engineering
Thesis Supervisor

Certified by_____
Dennis Whyte, Ph.D.
Professor, Nuclear Science and Engineering
Thesis Reader

Accepted by_____
Mujid S. Kazimi, Ph.D.
TEPCO Professor of Nuclear Engineering
Chair, Department Committee on Graduate Students

Design and Optimization of a Multi-Particle Accelerator Beam Transport and Delivery System for Material Irradiation in Nuclear and Fusion Science

By

Tyler Christopher Sordelet

Submitted to the Department of Nuclear Science and Engineering
On December 15, 2011, in partial fulfillment of the
Requirements for the degree of
Master's of Science in Nuclear Science and Engineering

# Abstract

A beam delivery and transport system were designed for the use in MIT Materials Test Facility ($M^2TF$). The purpose of this beam delivery system was to design a 36 MeV Proton Cyclotron for DPA accumulation and a 100 MeV Helium Cyclotron for irradiation failure and volumetric helium accumulation simulation. The purpose of the beam transport system was to incorporate the two cyclotrons into the beam transport system and transport their beams to the target chamber, the location of the target sample.

The cyclotrons were designed using Opera-3D and *Acfields*. The beam transport system was designed using TRANSPORT. The shielding analysis for the entire facility was designed using SolidWorks and calculated with MCNP/X. The design specification of $M^2TF$ with respect to beam energy, current density, and control were achieved based on these design tools and previously developed analytic methods.

The design process for the cyclotrons resulted in a 4.3T Isochronous Proton Cyclotron and 3.9T Isochronous Helium Cyclotron. A beam transport system connected the cyclotrons to the target chamber with three doublet quadrupoles and one dipole bending magnet. The shielding calculation proved the total effect dose rate in rem/year for the final design facility was safe for operational workers.

Thesis Supervisor: Ronald Ballinger
Title: Professor, Nuclear and Material Science and Engineering

Thesis Reader: Dennis Whyte
Title: Professor, Nuclear Science and Engineering

# Acknowledgments

I would like to thank my thesis advisor, Professor Ballinger, for his academic support, guidance and feedback. I could not have asked for a better advisor. Having been from the military himself, Professor Ballinger understood the United States Navy requirements and deadlines and worked hard to make sure I was on track and well prepared to graduate on time. His involvement with the science community and enthusiasm in creating MIT Materials Test Facility were of great help when we hit a "fence." Without my advisor, it would have been a rough two years at MIT.

I would like to truly thank Professor Dennis Whyte for being my thesis reader on such a short notice. His insights and timely feedback improved my thesis quality and allowed me to still graduate on time. Thank you for the invaluable discussions on proton and neutron simulations and important information about fusion materials and their environment.

It is difficult to express the significance of Dr. Timothy Antaya's contribution to my thesis. I am grateful to have shared a building with a leading cyclotron expert and proven engineer. He is always open to discussion, guidance, and questions on any topic. Without his expertise, inspiration, and feedback my thesis would not have existed.

I am indebted to many of my professors and classmates who supported me through the important details of my thesis. I would like to thank Harold Bernard for his help in python and heat transfer calculations, Professor Forget and Josh Richard for tutoring lessons in MCNP, and Robert Block for allowing me to use his hybrid cyclotron and beam analysis codes.

I owe it to my fiancée Kelli Reed and all my friends and family for the constant support that I have received over the past few years; I could not have done it alone. Finally, I would like to thank that United States Navy for its financial support and for providing me the opportunity to earn a masters degree at MIT before starting my wonderful and adventurous journey as an officer in the submarine force, "Go Navy!"

# Contents

# List of Figures

# List of Tables

# 1 Introduction

## 1.1 Motivation

Considering that the capital cost of nuclear reactors is in the billions of dollars, the nuclear industry cannot afford to shut down for unscheduled operational maintenance or material degradation issues; however, there is often no other option. Today's nuclear power plants in the United States have, on average, been in operation for over 25 years. With the United States' 30 year hiatus on the construction of new plants, several plants are running or have requested permission to run on life extensions twice as long as their original licenses [Raj & Vijayalakshmi, 2009]. Materials originally selected for structural components are now being operated at conditions beyond their original design, in many cases due to increased radiation dose. Irradiation displaces atoms from their lattice sites greatly increasing the concentration of point defects within the material, affecting the material structure and properties [Was G. S., 2007]. Effects include, but are not limited to, reduction in fracture strength, swelling, helium embrittlement, growth, phase instability and a wide array of surface effects [Was G. S., 2007]. Materials operated in fusion environments have similar radiation induced effects but must also operate in high temperatures and withstand a stronger and harder neutron spectrum.

While computer modeling methods utilizing Molecular Dynamics (MD) and Binary Collision Approximation (BCA) are becoming increasingly sophisticated, they are still unable to provide a true macroscopic representation of material damage [Adams, 1994]. The best simulation of these effects is done through a combination of experiments coupled with modeling and simulation. Test facilities for the evaluation of radiation effects due to neutron damage are few in number and very expensive to operate. Additionally, the ability of existing neutron sources to provide accelerated testing is very limited. It is difficult for these facilities to match the effect of radiation damage on materials for fusion applications which is several orders of magnitude more severe.

Experimental data is crucial and in high demand for resolving the effects of radiation damage on long term operation of Light Water Reactors (LWR) and the design of advanced reactors and fusion systems. Figure 1-1 illustrates the temperature versus expected radiation damage, defined as displacements per atom (DPA) for Generation II and Generation IV reactors and fusion systems. It is

not only the accumulation of DPA that is important but also its associated temperature range over which the damage occurs [Zinkle, 2007].

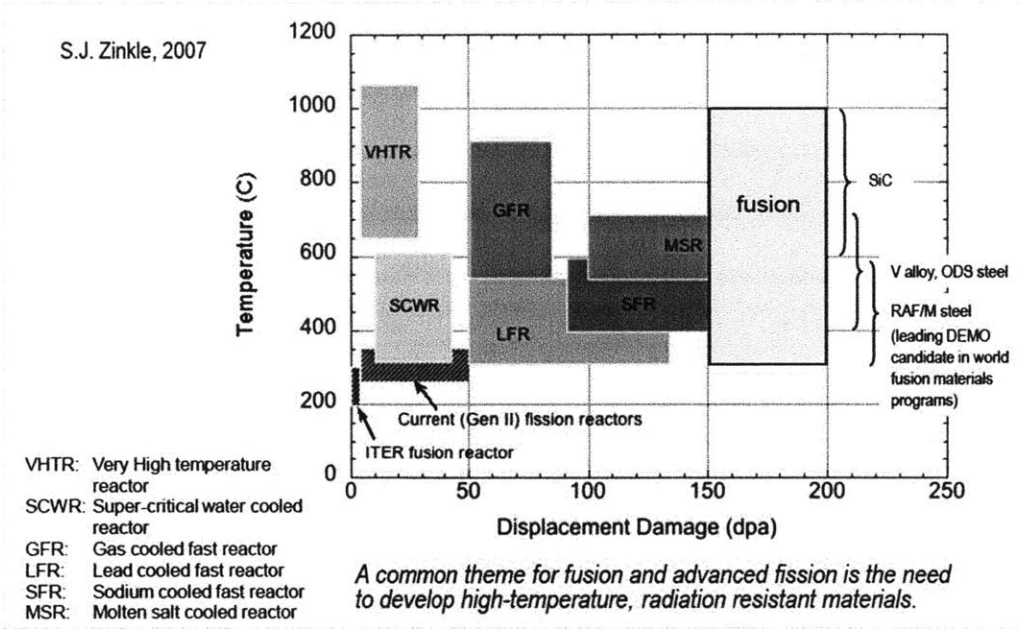


**Figure 1-1: Temperature vs. displacement damage for different reactors and fusion systems. Figure adapted from [Zinkle, 2007].**

There is a need for helium effects data for fusion first wall exposure and LWR end-of-life conditions. The helium, when combined with displacement damage, can embrittle the material explicitly and greatly aggravate void swelling. Neutrons damage materials through two mechanisms: the displacement of atoms in the material and the accumulation of helium from the alpha decay of activated nuclei and (n, α) reactions. The solubility of helium is low in most materials so helium precipitates as bubbles in the matrix creating three dimensional (3D) defects or stabilized voids. Helium bubbles are also very immobile compared to vacancies or interstitials in the temperature range of void formation. Once helium bubbles precipitate, they are unlikely to diffuse [Was G. S., 2007]. Helium bubbles or helium stabilized voids alter the material structure, reducing its strength. These detrimental effects include swelling, hardening, and embrittlement [Was G. S., 2007]. Figure 1-2 illustrates the importance of the ratio of atomic parts per million (appm) of helium and its associated displacement damage. The figure also stresses the relationship of the helium/DPA ratio, not just the accumulation of one or the other. Due to the hard spectrum of neutrons in fusion systems and thus higher (n, α) cross-sections, fusion materials experience several orders of magnitude higher helium concentrations than LWRs.

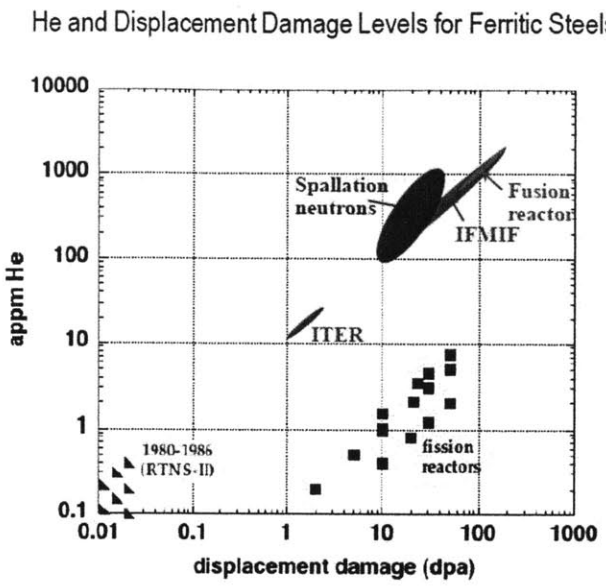


**Figure 1-2: Helium/DPA ratios for nuclear reactors and fusion systems. Figure adapted from [Whyte, 2010].**

With the research and development for the Generation IV reactors and the study of fusion first wall materials, it has become obvious that there is a need for a materials testing facility that can accurately and quickly assess material properties. Experimental data is lacking, especially for the specific temperatures of operation for these systems as well as helium/DPA ratios described above [Whyte, 2010]. Currently, there are no fast spectrum and only two thermal spectrum test facilities: the Advance Test Reactor (ATR) and the High Flux Isotope Reactor (HFIR). Until, the proposed International Fusion Materials Irradiation Facility (IFMIF) becomes a reality in a decade, there will be no fast spectrum neutron test facility that can duplicate the fusion energy spectrum. IFMIF's mission will be to produce high energy neutrons (up to ~30 MeV) at sufficient intensity and irradiation volume, to expose samples of candidate materials to an anticipated full lifetime exposure in fusion energy reactors [IEA, 2011]. However, IFMIF will cost several billion dollars to build and several million dollars annually for operation, yet only capable of exposures of 10-20 DPA per year. Thus, testing end-of-life materials in a fusion device with IFMIF would take years. Clearly, a facility that could achieve at least 40-50+ DPA per year and be capable of simultaneous volumetric deposition of helium would be of enormous value to the scientific community.

## 1.2 Background

The objective of accelerated irradiation tests using ion irradiation is to simulate accumulated lifetime damage that a material would experience from a reactor in a shorter time than actual exposure lifetime. Ion-based accelerated irradiation has many advantages over neutron irradiation but also some significant issues that must be adequately addressed. Light ion (proton) irradiation decreases induced radioactivation of the test equipment and instrumentation, increases the reliability of the experiment allowing it to be interrupted without disturbing the sample, and the energy of the ion beam is variable. Most importantly, proton irradiation time and associated operational costs are substantially less compared to neutrons [Was G. S., 2007]. These advantages stem mainly from the fact that proton irradiation is performed by impinging a tightly defined proton beam from a particle accelerator on the target rather than placing the target (sample) in the core of a nuclear reactor. Accelerated damage results from Coulomb collisions of the charged particles creating more damage per particle. A typical neutron irradiation experiment in a test reactor requires a year for sample preparation, cooling analysis and capsule design before it is tested, followed by 1-2 years (or more) of neutron exposure in the reactor [Sickafus, Kotomin, & Uberuaga, 2007]. Additional time is needed because of the safety and regulatory issues for the handling of radioactive materials in the vicinity of a nuclear reactor and because of the high activation level of the irradiated sample. This time period, as well as the high overall cost of the test, does not allow for multiple campaigns and timely turn around due to schedule and budget restrictions. Proton irradiation time periods are 1/10 that of a neutrons and 1/100 of the cost [Sickafus, Kotomin, & Uberuaga, 2007]. Since time and cost are closely related, proton irradiation generates drastic savings but at the possible cost of not exactly replicating the damage in a neutron environment. Nonetheless, the cost and schedule advantages of light ion irradiation clearly motivate further study.

Linear particle accelerators (LINACs) accelerate charged particles by subjecting them to a series of oscillating electric potentials along a linear beam line. As the particle increases in energy and in mass, the length of the required electrodes increases, creating longer and longer electrical potential segments. To achieve 36 MeV protons and 100 MeV helium ions would require a LINAC comparable to a football field in length. The length of a linear accelerator restricts the locations it can be placed. LINACs also contain a number of stabilizing, steering, and accelerating components that require immense amounts of power, increasing construction, operational, and maintenance costs. With the advent of the Lawrence Cyclotron in the 1930s, cyclotrons have been utilized in

many research environments instead of their counterpart, linear accelerators. Cyclotrons use a magnetic field to accelerate particles in a circle, in order to send them through the same accelerating electrode repeatedly to gradually increase the particles' energy. This technique greatly reduces the space needed to accelerate ions to high energies and allows irradiation facilities to be much smaller in size. Other benefits of a cyclotron included low weight, low power, small size, and ease of operation [Griffiths, 1989]. Cyclotrons and superconducting cyclotrons (cyclotrons that use superconducting coils to generate a magnetic field) are becoming very common in universities and research labs due to their benefits over larger, heavier linear accelerators.

## 1.3 Mission Statement

In order to address the issues discussed above, a novel accelerator based materials test facility, MIT Materials Test Facility ($M^2TF$), is being designed for the simulation of high energy, high DPA rate bulk radiation damage with simultaneous helium volumetric implantation in samples up to 1 mm thick. Radiation damage will be simulated by inducing displacement damage with protons in an irradiation facility that will allow the accumulation of dose in advanced materials in a reasonable amount of time, tens of DPA/month. The simultaneous presence of a helium beam allows for the uniform volumetric implantation of helium in the sample to simulate a second materials damage effect that occurs in nuclear reactors. Independent control of helium/DPA ratio will allow for fast fission, fusion and fission material irradiation simulations. The overall size of the facility will be addressed by making use of superconducting cyclotrons. $M^2TF$ will use two superconducting cyclotrons to accelerate the required helium and proton beams, which are a key feature of the facility. Compact cyclotrons will make the $M^2TF$ university-sized and lower cost than equivalent facilities, of which none currently exist.

## 1.4 Thesis Objective

The required accelerator system characteristics are defined in Table 1-1 and the required $M^2TF$ specifications are defined in Table 1-2. Given the energy range, intensity, time structure, operating modes, and type of irradiation, the purpose of this thesis is to develop an optimized cyclotron and beam transport system for a nuclear materials irradiation test facility. This will also

include a geometric layout and proper shielding for all operating systems that meet M²TF design parameters.

**Table 1-1: Required accelerator specifications for M²TF.**

| | |
|---|---|
| Number | 2 (Helium, Proton) |
| Ions | Helium (Z/A=0.5)<br>Protons (Z/A=1) |
| Beam Intensity | 0.1 mA/cm² |
| Beam Type | High Intensity or CW |
| Beam Energy (Max) | 100 MeV Helium<br>36 MeV Proton |
| Final Beam Size | 2 mm vertical<br>5 mm horizontal |
| Degrader Range | 0-100 MeV Helium<br>12-36 MeV Proton |
| Cyclotron Field Range | 3-7T<br>(Optimized design to limit overall size and cost) |

**Table 1-2: Required M²TF design parameters.**

| | |
|---|---|
| Facility Size | Less than 225m² to allow placement into a typical lab room |
| Radiation Requirements | Less than the Total Effective Dose Rate (TEDE) limits (per 105 CMR 120.211) of 5 rem/year |
| Facility Layout | Separate shielding for each cyclotron and target chamber to allow for safe individual chamber maintenance during facility operation |

## 1.5 Facility Characteristics

M²TF is a new and different irradiation test facility that hopes to accomplish many of the problems encountered during accelerated proton irradiation testing. It is unique in that it will use gas jet impingement cooling to cool the target sample. A higher heat removal allows for a higher beam current, therefore, higher damage rates can be achieved. A target sample thickness of 1 mm will allow a 36 MeV proton beam to generate uniform damage throughout the sample. The benefit of using of compact superconducting cyclotrons is the entire beam transport and required shielding can be scaled down to a university-size, reducing overall cost.

The challenges to the achievement of the design include: constructing a valid argument to affirm that protons are a reliable and useful tool in simulating neutron damage, addressing the concern of damage cascade timescales, designing a compact, cost-effective cyclotrons for two separate ion species, creating proper radiation shielding for the target chamber and cyclotrons, and developing a beam transport design to direct two beams of different energy to the target chamber. Issues related to heat removal restrictions and its effect on DPA rates, sample thickness, and jet impingement cooling design are not discussed in this thesis but are further discussed in TSTARC [Barnard, Ferry, & Payne, 2010].

## 1.6 Thesis Outline

Chapter 2 provides an overview of accelerated irradiation, irradiation studies, and arguments.
Chapter 3 details the design and design process for both cyclotrons.
Chapter 4 describes the shielding calculations necessary for the proposed $M^2TF$ facility.
Chapter 5 includes complete 2 Dimensional (2D) beam transport design and simulation.
Chapter 6 presents conclusion of this work as well as suggestions for future work.
Chapter 7 lists the references used in this thesis.

# 2 Irradiation Overview

The objective of this chapter is twofold: to support and explain the claims in the M²TF mission statement and to construct a valid argument to affirm that protons are a reliable and useful tool in simulating neutron damage.

## 2.1 Achieving High DPA Rates

Heinisch and Martinez's experiment with radiation induced strengthening of 316 Stainless Steel proved, by the comparison of yield strength change subjected to different incident particle fluences, that the use of displacements per atom (DPA) to represent radiation damage was a viable method[Heinisch & Martinez, 1986]. Their result led to the NRC support of the DPA method of damage assessment as the acceptable standard and as a result has been universally adopted in the scientific community [NRC, 1988]. One DPA represents that every atom in the material has been displaced once from its original lattice site as a result from incident particle fluence [Was G. S., 2007]. The basic formula for calculating DPA for a given system can be derived from the damage rate equation seen in Equation (2.1). If N is the atomic number density, $\phi(E_i)$ is the incident particle flux, and $\sigma_D(E_i)$ is the displacement cross section at energy $E_i$, then the radiation damage $R_d$ in $cm^{-3}$-s is given by:

$$R_d = N \int_{\check{E}}^{\hat{E}} \phi(E_i)\sigma_D(E_i)dE_i \tag{2.1}$$

Equation (2.1) provides the rate of "primary" displacements, those caused directly by collision of the incoming particle and target atom. Accurate calculations of "total" DPA, however, are much more complex. For instance, the consideration of the production of primary knock-on atoms (PKA) following damage cascades and the subsequent migration of vacancies and interstitials in the lattice must be evaluated [Was G. S., 2007]. For complicated models, such as that used in the design of M²TF, DPA rates were calculated through computer simulations and modeling. Computer calculations were then checked with a detailed analytical calculation for accuracy and continuity.

Stopping and Range of Ions in Matter (SRIM) is a Binary Collision Approximation (BCA) based Monte Carlo code that is used for displacement calculation [Ziegler & Biersack, 1984]. BCA is a very complex process and only a brief discussion will be provided. The principle assumption of BCA is that the interactions of all particles can be separated into a series of distinct two-body encounters [Was G. S., 2007]. By doing so, changes in the relative energy can be confined to the immediate vicinity of the target atoms. Figure 2-1 illustrates the BCA assumption.

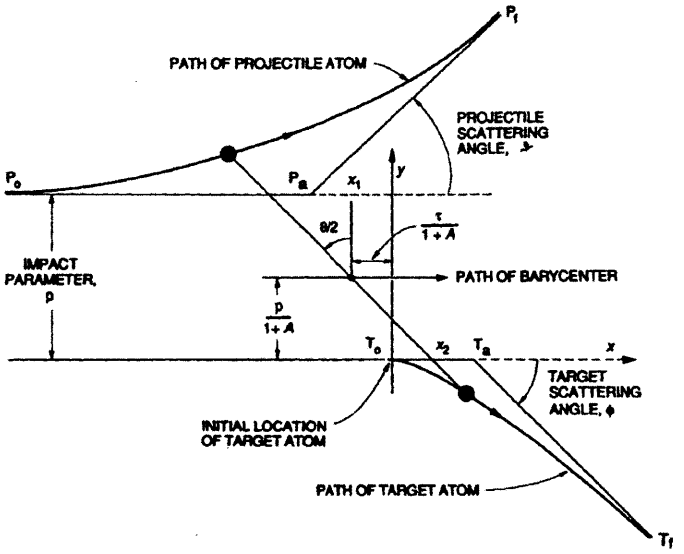


**Figure 2-1: Illustration of BCA interaction of atoms. Figure adapted from [Robinson & Torrens, 1974].**

The BCA method involves the following steps adapted from [Robinson & Torrens, 1974] and [Was G., 2002].

1. Primary recoil energy, position, and direction are provided as input to the program.
2. The PKA is followed through the series of binary Coulombic atomic collisions.
3. The classical scattering integral between the two particles for the impact parameter (recall Figure 2-1) is solved.
4. Solution gives the scattering angle and associated electronic energy loss.
5. If the energy transferred is greater than the displacement energy, displacement is assumed to occur and the atom will be added to the cascade.
6. When the energy of the particle becomes very small or escapes from the target it is dropped from the cascade.
7. The model is stopped and various analysis and calculations are performed.

As stated earlier, BCA only accounts for potentials within the vicinity of the target atom. This assumption is valid for high energy particles because many-body interactions have little contribution to changing the atoms trajectories at energies well above the atom's displacement energies [Robinson & Norgett, 1975]. Monte Carlo (MC) codes, like SRIM, use a random probability for the impact parameter, whereas other codes use pre-determined values. Since MC codes follow individual particles trajectories and paths until completion, SRIM is very accurate when large samples are used. Large samples allow particles to experience all possible outcomes and hence provide a more accurate and better simulation.

An analytical method for DPA calculation was adapted from Was' *Fundamentals of Radiation Materials Science* [Was G. S., 2007]. Was derived Equation (2.2) from the initial damage rate Equation (2.1) and applied the following principles and assumptions:

1. Neglect (n,2n) and (n,γ) reactions.
2. Isotropic scattering.
3. Rutherford Scattering for σ (E,T).
4. Lindhard Treatment for ν(T).
5. A damage energy efficiency, ξ, of 50%.

The above assumptions were adapted from the energy loss by electronic excitation presented by Lindhard but applied for charged particle irradiation.[1] Applying the above assumptions, the result is Equations (2.2) and (2.3), with units of DPA per ion flux. Table 2-1 lists the meaning of each symbol represented in the equations.

$$\frac{R_d}{NI} = \frac{\pi Z_i^2 Z_2^2 \in^4}{4E_1 E_d}\left[\frac{M_i}{N}\right] ln\left(\frac{\gamma E_i}{E_d}\right) \quad \frac{dpa}{ion/cm^2} \tag{2.2}$$

$$\gamma = \frac{4M_1 M_2}{(M_1 + M_2)^2} \tag{2.3}$$

[1] More detail regarding the choice and validation of each assumption can be found in [Was G. S., 2007] and [Lindhard & Scharff, 1963].

**Table 2-1: Symbol explanation of Was' DPA Equation (2.2).**

| Symbol | Meaning |
|---|---|
| N | Number Density of Sample Material |
| I | Incident particle Flux of Beam |
| $M_i$ | Mass of particle of material |
| $E_i$ | Energy of Incoming Particle |
| $E_d$ | Displacement Energy of Material |
| $R_d$ | Damage/Displacement Rate |
| $Z_i$ | Charge of particle or material |
| $\epsilon$ | Unit Charge equivalent |
| $\xi$ | Damage Efficiency |

The results of DPA calculation for iron using the Monte Carlo (SRIM) method can be seen in Figure 2-2. A total of five energies (10, 20, 30, 40, 50 MeV) were used in SRIM to compute the DPA per year normalized to a 0.1 mA/cm$^2$ beam current density; a line of best fit was applied to those points. Two lines were generated based on default displacement energy values for SRIM (25 eV, green line) and ASTM E521-96 (40 eV, red line). The analytical method can be seen in Figure 2-3. Figure 2-3 has three lines plotted: the blue line represents the minimum displacement energy (20 eV), the green line represents the SRIM default displacement energy (25 eV), and the red line represents the average displacement energy (40 eV). For both figures, the x-axis is the energy of the incoming particle. Since M$^2$TF will be an accelerated damage rate facility, the y-axis was labeled in DPA per year normalized to a 0.1 mA/cm$^2$ beam current density (recall Table 1-1).

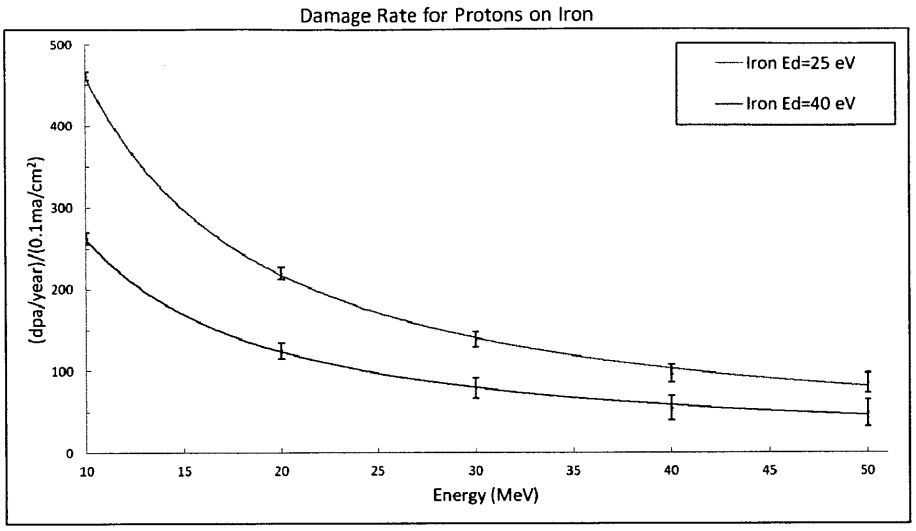


**Figure 2-2: SRIM DPA calculation for Protons on Iron. Proton energies of 10, 20, 30, 40, and 50 MeV were solved in SRIM. Two runs were completed: displacement energy of 25 eV (green) and 40 eV (red). A line of best fit was drawn between the points.**

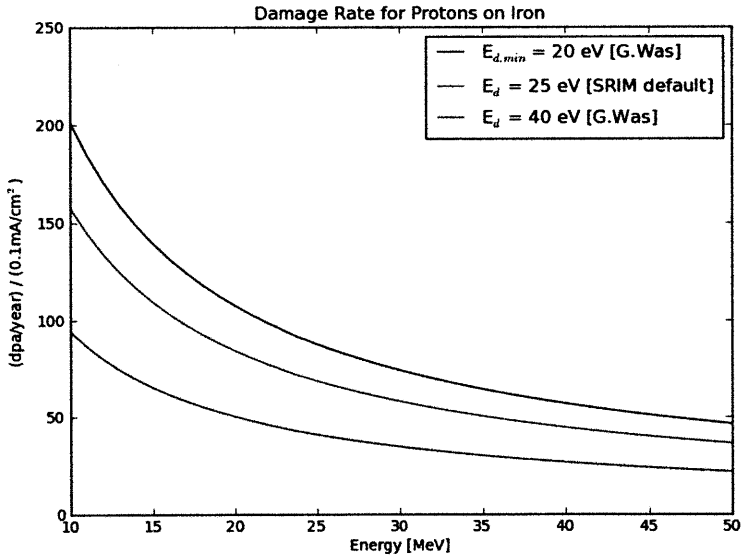


**Figure 2-3: Equation (2.1) DPA calculation with displacement energies of 20 (blue), 25 (green), and 40 (red) eV.**

By comparing the DPA estimation for iron in both figures at 36 MeV, the SRIM calculation predicts higher DPA rates than the analytical method. The disagreement arises partially from the selection of the displacement energy; $E_d$. $E_d$ not only varies with material but also is dependent on crystallographic effects, focusing, tunneling, and angle of impact [Was G. S., 2007]. In the selection of $E_d$, SRIM defaults to minimum displacement energies, usually around 25eV for metals. A lower

displacement energy accounts for higher damage rates (observed in Figure 2-2). ASTM E521 *Standard Practice for Neutron Radiation Damage Simulation by Charged-Particle Irradiation* has published a table, provided here in Table 2-2, with accepted values of $E_d$ for common materials [ASTM E521-96, 2000]. For clarification, ASTM substitutes $T_d$ for $E_d$. ASTM recommends the value of 40 eV for steels based on its computer simulation of low-energy cascades, rather than directly on displacement threshold measurements [ASTM E521-96, 2000]. Thus, taking in account of the difference of displacement energy selection, the two methods of DPA calculation are in agreement by a factor of two.

**Table 2-2: ASTM E521-96 displacement energies for common materials. Notice the variance between the minimum and average displacement energy in iron. Table adapted from [ASTM E521-96, 2000].**

| Metal | $T^{min}$(eV)[A] | $T_d$(eV) |
|---|---|---|
| Al | 16 | 25 |
| Ti | 19 | 30 |
| V | — | 40 |
| Cr | 28[B] | 40 |
| Mn | — | 40 |
| Fe | 20[B] | 40 |
| Co | 22 | 40 |
| Ni | 23 | 40 |
| Cu | 19 | 30 |
| Zr | 21 | 40 |
| Nb | 36[B] | 60 |
| Mo | 33 | 60 |
| Ta | 34 | 90 |
| W | 40 | 90 |
| Pb | 14 | 25 |

[A] See review by P. Lucasson in *Proceedings of International Conference on Fundamental Aspects of Radiation Damage in Metals*, Gatlinburg, Tenn., October 1975.
[B] An effective threshold measured in a polycrystalline specimen.

As seen in Figure 2-2 and Figure 2-3 large DPA can be accumulated in short periods of time depending on the materials thickness, stopping power, and material properties. Accepting the recommendation of a displacement energy of 40eV from ASTM will result in 40-50 DPA/year accumulation for 36 MeV protons on iron at 0.1 mA/cm$^2$ incident flux rate. This allows the M$^2$TF to simulate PWR lifetime damage in a few years. However, there are some limitations in damage accumulation due to heat removal and temperature difference restraints. Those constraints in the targets will not be discussed here but can be read in TSTARC [Barnard, Ferry, & Payne, 2010].

## 2.2 Proton vs. Neutron Damage

As described above, light ion irradiation using an accelerator has significant advantages over neutron irradiation. These advantages include reduced activation, increased reliability, ease of availability, reduced cost, and faster accumulation of damage. Light ion irradiation does have its disadvantages. In recent years there has been an ongoing debate on whether light ion irradiation can accurately simulate neutron irradiation because of the inherent difference between a charged particle and a neutron. Arguments include the differences in the ion's Bragg Peak and mean free path of a neutron, differences in nuclear interaction and given recoil spectrum, and the comparison of materials effects such as radiation induced segregation, swelling, dislocation loop population and density, and much more. These topics will be discussed below along with actions that are necessary to provide more accurate damage simulation and accumulation.

Simulating neutron damage with ion irradiation is an established technique with well documented ASTM procedures [ASTM E521-96, 2000]. However, their use to date for materials testing has largely been limited by low energy beams which cannot produce uniform bulk damage in materials. When the beam energy is too low or the materials stopping power is too high, the ions will not be able to penetrate beyond a surface interaction of several tens of μm. When this event occurs, the particle will create a Bragg Peak a point where the peak in energy loss occurs [Nelson, 1970]. The Bragg Peak occurs because the interaction cross section increases as the particle's energy decreases. Examples of Bragg Peaks (red circles) are illustrated on Figure 2-4. As illustrated in Figure 2-4, neutrons do not exhibit a Bragg Peak because of their high mean free path for interaction. Due to this phenomenon, uniformity is important in simulating neutron irradiation effects. In order to simulate bulk effects with protons, high energy beams (30-40 MeV) are required to penetrate thicknesses greater 1 mm for common reactor materials, which results in the location of the Bragg Peak beyond the sample (Figure 2-5) [Ziegler & Biersack, 1984]. A proton beam, at high energy, will have a more uniform damage profile throughout the sample thickness. For most materials, if the sample is thinner than 2-3 mm, the Bragg Peak energy will not be deposited within the sample. The solution to bulk and uniform damage requirement is to adopt a sample thickness of 1 mm (marked on Figure 2-5). A sample thickness of 1 mm also allows for accurate tensile and

hardness properties based on bulk properties. Grain sizes in metals range from 10-100 $\mu m$. With 10 grains of maximum size (100 $\mu m$), the sample would need to be 1 mm thick [Callister, 2010].[2]

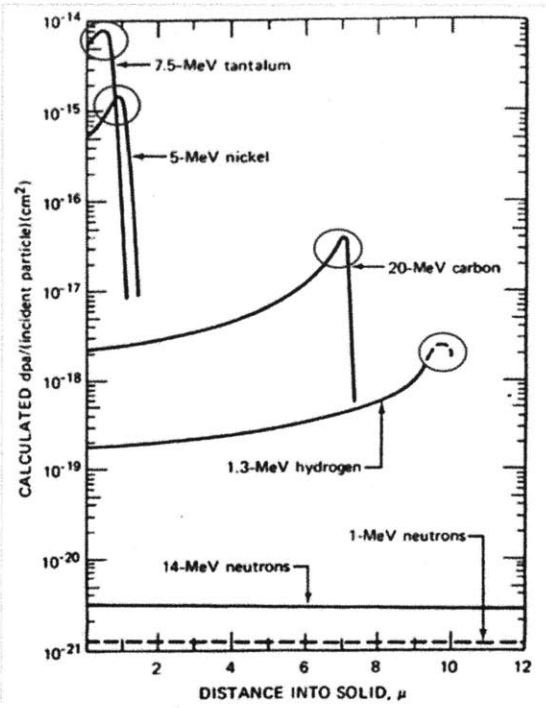


**Figure 2-4: Damage profile comparison of protons, neutrons, and heavy ions. The y-axis is the DPA per incident particle. The x-axis is the distance into the solid in micrometers. The red circles note the particles Bragg Peak. Figure adapted from [Kulcinsji, Brimhall, & Kissinger, 1972].**

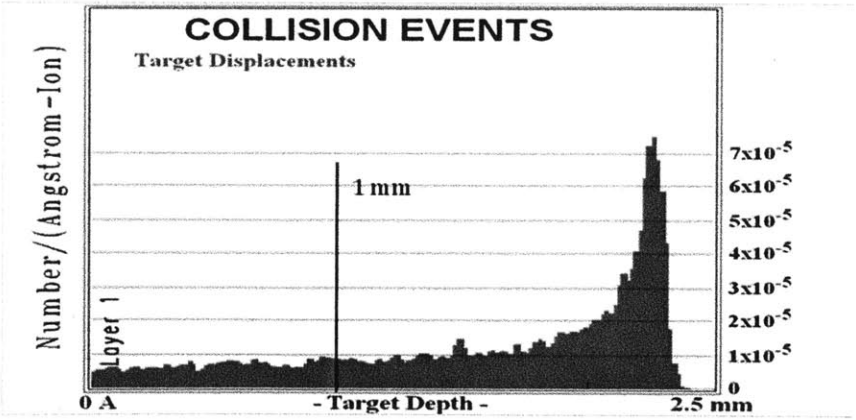


**Figure 2-5: Uniform interaction of 36 MeV Proton Beam on an Iron sample with 1 mm marked line. Note location of Bragg Peak outside of sample. Figure generated using SRIM.**

[2] Since every metal has a different grain size, the sample thickness could be less than 1 mm and still consist of 10+ grains.

During irradiation, the positively charged protons have two probable interactions within the crystal structure: proton-electron or proton-nucleus. The proton-electron interactions occur between the impinging protons and the atomic electrons of the metals in the crystal lattice. This 'coulomb' interaction slows the protons and heats the sample. This interaction is different than that of neutron irradiation because the neutron experiences no coulomb interactions with orbital electrons because of its net charge neutrality. This difference can be ignored and deemed insignificant if the ratio of incident energy to energy transferred to the sample is maximized but this still leads to the heating of the sample [Logan, 1973]. A high energy proton beam creates significantly less energy loss in the sample because stopping power decreases with particle energy in coulomb collisions. Achieving high energy is also essential to duplicating neutron PKA energy spectrum. At long distances, the proton-nucleus interaction is also a coulomb interaction and at short distances (nuclear radii) the interaction is due to the nuclear strong force. These interactions inelastically transfer energy to the lattice structure. The transfer of energy will be dominated by screened-Rutherford, classical-Rutherford, or nuclear forces and result in small, widely spaced cascades [Logan, 1973]. As the ion slows down, electronic screening of the nuclear charge will become more important and the Rutherford collision approximation will lose validity [Nelson, 1970]. In comparison, since the masses are nearly identical, an elastically scattered proton at a given energy and angle will create identical PKAs to that of a neutron with the same initial conditions. Damage from protons is caused by long range coulomb scattering in addition to large angle nuclear scattering. Damage from neutrons, however, is dominated by large angle nuclear scattering only, causing higher average recoil energies than equivalent large angle proton scattering [Was G. S., 2007]. The recoil spectra for mono-energetic protons versus neutrons can have similar distributions for high energy recoils, but may vary substantially for low energy recoils as seen in Figure 2-6 [Logan, 1973]. With the use of higher energy protons, above 14 MeV, the difference in recoil spectra can be minimized. This is because the angular region where the scattering mechanism is different for the proton is where Rutherford scattering predominates. "Since the Rutherford differential cross section is inversely proportional to the square of the incident energy, proton scattering at these angles is suppressed by increasing the incident energy" [Logan, 1973]. In addition, for realistic material exposure in nuclear-energy applications the neutrons have a continuum of down-scattered energy, which is a better match to the intrinsically broader PKA spectrum of mono-energetic ions than mono-energetic neutrons. In summary, while protons do not provide perfect simulation of neutron damage, these differences can be greatly reduced by

elevating the proton energy to provide uniform volumetric damage and better matching PKA spectrum.

If ion irradiation is to be used to emulate neutrons, it must match in both processes of magnitude and dose evolution. In a very detailed experiment performed by Was, materials were selected that had sufficient neutron irradiation data and compared to that of proton irradiation at similar energies. After irradiation, the areas compared where grain boundary composition and composition profiles, microstructure, hardness and stress corrosion cracking susceptibility, and creep [Was G., 2002]. Was et. al concluded that proton irradiation results were in excellent agreement with neutron irradiation data proving that ion irradiation can simulate neutron irradiation effects.[3] However, other experiments have shown that certain material damage characteristics, such as swelling and the creation of interstitials are not the same for proton and neutron irradiation. The testing of the swelling process in stainless steels in the EBR-II versus a proton accelerator resulted in a difference between the final peak swelling temperatures [Abromeit, 1994]. Low energy proton irradiation allows the inhomogeneous creation of interstitials that change the swelling behavior at the depth where the particle comes to rest. The use of high energy proton beams, such as that with the design of the M²TF, that penetrate through the sample will minimize this effect but not eliminate it. In an important fusion study, C.M. Logan proved that 16.4 MeV incident protons simulated 14 MeV neutrons in the total number of PKAs and comparison of recoil and damage spectra [Logan, 1973]. The simulation of 14 MeV neutrons with protons is essential when testing fusion materials. In a D-T based fusion reactor, the T(d, n)He reaction carries 14.1 MeV or 80% of the net reaction energy. This high neutron flux of energy is of great concern due to its effect on structural materials [Logan, 1973].

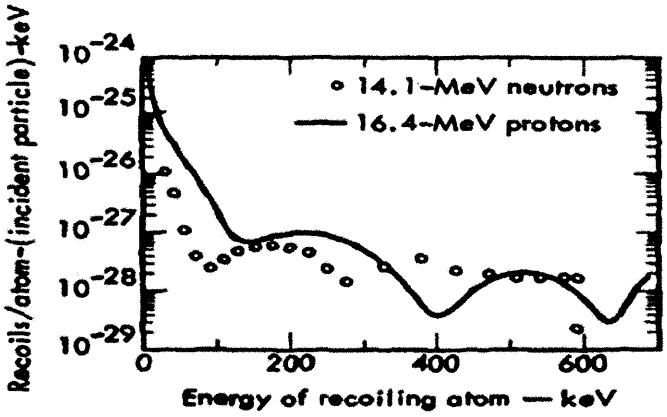


[3] Detailed figures can be seen in reference [Was G., 2002]

**Figure 2-6: Recoil Spectrum for 16.4 MeV protons and 14.1 MeV neutrons in Nb. The recoil spectrums of the two particles are similar at higher energies but vary at lower energies. Figure adapted from [Logan, 1973].**

Considering ion irradiation is relatively new, there are many arguments for and against its uses to simulate neutron irradiation effects. Ion irradiation in careful experiments has been proven to simulate most material effects, but not all. Overall, ion irradiation's advantages seem to outweigh its disadvantages in providing an inexpensive, fast simulation of neutron damage and damage physics. Such disadvantageous can be minimized, as described above or noted when analyzing results. Most important is to design a radiation facility with maximum flexibility so that various self-consistency checks can be made, for example the effect of flux versus fluence.

## 2.3 Helium Implantation Technique and Rates

Employing simultaneous helium volumetric implantation using a helium cyclotron in conjunction with a proton cyclotron has three benefits when compared with many existing proton or other radiation simulation facilities: achievement of highly flexible helium/DPA ratios, rapid and controlled production of helium accumulation, and simulation end-of-life helium concentrations for reactor materials. With a highly flexible helium/DPA ratio achievable by the use of separate proton and helium cyclotrons, the M²TF can accurately test most fission or fusion materials. Annual helium accumulation for fission metals range from 10-100 atomic parts per million per year (appm/year) and fusion systems can be well above 1000 appm/year [Whyte, 2010]. With the anticipated current density of helium beam ($J_{He}$), the thickness of the sample ($\Delta x$) and the number density of the target sample ($n_t$), the helium implantation rate ($R_{He}$) can be calculated in appm/hr in Equation (2.4) [Barnard, Ferry, & Payne, 2010].

$$R_{He} = 3.6E9 * \frac{J_{He}}{e * n_t * \Delta x} \quad \frac{\left[\frac{A}{m^2}\right]}{[coul] * \left[\frac{atoms}{m^3}\right] * [m]} \tag{2.4}$$

A representative normalized rate of helium implantation as a function of target thickness is displayed graphically in Figure 2-7 in appm/hr and in Figure 2-8 in appm/day for Graphite, Stainless Steel 204, Inconel 600 and Tungsten. Each figure is plotted against the sample thickness in mm (x-axis). Recall that the design sample thickness for M²TF is 1 mm for most materials. Since all the energy from the helium beam is implanted into the specimen, important issues of heat removal arise. A modest heat removal rate of 1 MW/m² is generally considered not too challenging for

helium jet impingement cooling and was therefore chosen as the normalization constant for both figures [San, Huang, & Shu, 1997]. Therefore the figure displays the implantation rate in appm/time per 1 MW/m$^2$.

Equation (2.4) and Figure 2-7 illustrate that helium accumulation in fission reactors can be accomplished in hours and for fusion systems within days in M$^2$TF. It is also possible to simulate end-of-life effects on materials with helium implantation at high temperatures. Since the solubility of helium is low in most materials, and the bubbles are relatively immobile, most materials will ultimately be limited by helium accumulation [K, Katoh, Ando, & Kohyama, 2003]. Defects caused by radiation damage due to protons can be thermally annealed at high temperatures. Thermal annealing has been explored in steels, silicon carbide, and tungsten [Kleuh, Ehrlich, & Abe, 1992]. As a result, for certain materials at high temperature, it is possible to simulate radiation damage at much higher rates with only helium implantation, assuming the removal of damage occurs by annealing. Typical end-of-life DPA values for a fission reactor are 100+ DPA [Was G. S., 2007]. Given a Helium/DPA ratio, the amount of helium needed can be determined for an end-of-life simulation. With a separate operating helium cyclotron, only days are needed to simulate the end-of-life of materials absorption of helium as opposed to months and years when using light ion based DPA studies.

For a profile test, it is best to have helium energies of 15-60 MeV because the elastic scattering cross section is highest and remains relatively constant as the beam loses energy [ASTM E942-96, 2011]. For M$^2$TF, penetration of a 1 mm sample cannot be accomplished with the recommend ASTM energy range. Only helium ions above 100 MeV have ranges around 1 mm for most reactor materials [Ziegler & Biersack, 1984]. In order to achieve uniform helium implantation the cyclotron must operate at full energy while the beam energy is reduced with an energy degrader, thus controlling the depth of the helium implant. This method of uniformity is different than that of the proton irradiation. For proton irradiation, the goal is to subject the test material to a uniform dose of the proton beam throughout the cross-section (refer to section 2.2 and Figure 2-5), whereas the helium beam's Bragg Peak will be rastered throughout the depth of the sample to implant the material with helium. While this simultaneously damages the materials, the cumulative damage will be small because end-of-lifetime accumulation can be achieved in such a short period of time.

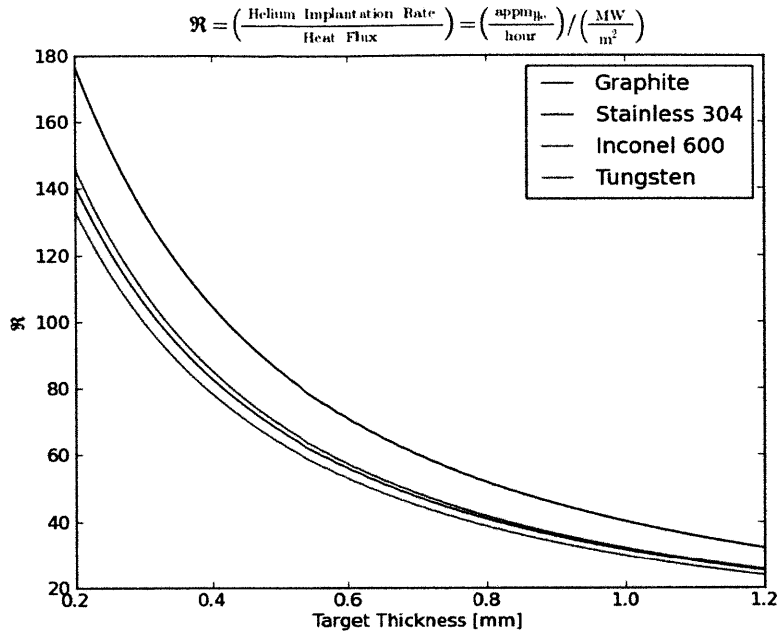


**Figure 2-7: Appm of volumetric helium implantation per hour (y-axis) for Graphite, SS, Inconel 600 and Tungsten with respect to target thickness in mm (x-axis).**

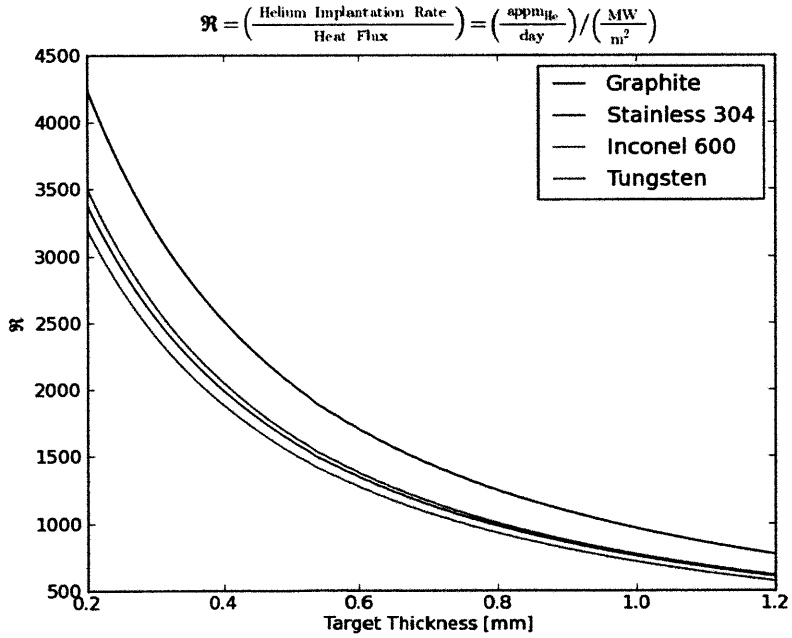


**Figure 2-8: Appm of volumetric helium implantation per day (y-axis) for Graphite, SS, Inconel 600 and Tungsten with respect to target thickness in mm (x-axis).**

## 2.4 Heavy Ions Simulation of Radiation Damage

Heavy ion irradiation was first used in the 1970s to simulate neutron damage effects in breeder reactors.. The choice of heavy ions is limited only by the type of advanced ion source selected and the available charge to mass ratios (Z/A) possible for a particular species [Antaya, 2010]. Many ions, from carbon to uranium, can be accelerated in one machine. The superconducting cyclotrons first introduced in the 1980s were intended for variable ion species and final energy heavy ion acceleration. Versatility, variety, and availability of ion sources create a moderate operational cost for a wide range of studies. Since the 1980s, it has become a well established technique and has been adapted to include a multitude of fission and fusion experiments. In the near future, heavy ion cyclotrons may even include simulation of material effects from heavy ion contamination in plasmas [Antaya, 2010].

Time is important when trying to simulate neutron damage effects in a research setting. Irradiation with heavy ions better simulate neutron damage effects in a material in short time periods because of high dose rates, Figure 2-4. In comparison, light ion beam currents still provide radiation in short periods of time but orders of magnitude less than that of heavy ions [Was G. S., 2007]. Heavy ions have the ability to better match the neutron recoil spectrum. This makes them very efficient at producing dense cascades with large cluster damage, nearly identical to those produced by neutrons [Sickafus, Kotomin, & Uberuaga, 2007]. As seen in Figure 2-9, heavy ions have the densest damage cascade compared to neutrons. Again it is important to note that by supplying higher energy protons, the match to neutron interactions improves. If heavy ions are accelerated to energies below the coulomb barrier, the important nuclear properties can be extracted from the test material. With acceleration to energies above the coulomb barrier, detailed aspects of the nuclear interaction (effects of deformations on scattering and reaction processes and ion-ion potential) can be studied [Grunder & Selph, 1977]. Independent of energy, heavy ion irradiation advances understanding of the reaction mechanism, transfer reactions, compound-nucleus formation, and inelastic processes. All which are fundamental in the study of nuclear materials and radiation effects.

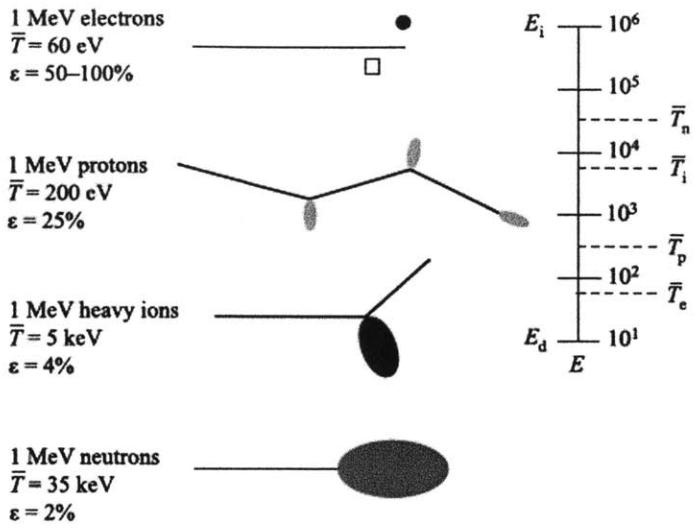


**Figure 2-9: Damage cascade from 1 MeV electrons, 1 MeV protons, 1 MeV heavy ions, and 1 MeV neutrons. Notice that heavy ions better match the damage spectrum created from neutrons. Figure Adapted from [Was G. S., 2007].**

There are a few disadvantages of heavy ion irradiation when simulating neutron damage effects. High dose rates produce large temperature increases due to volumetric heating, resulting in heavy ion irradiation being conducted at higher temperatures in order to simulate neutron irradiation at a lower temperature [Sickafus, Kotomin, & Uberuaga, 2007]. Heavy ions also have small penetration depths and as a consequence damage rates in the bulk material would not be uniform. Figure 2-4 demonstrates the short penetration depths of heavy ion compared to other irradiation ions (heavy ion irradiation is demonstrated by the two curves in the top left of the figure). Figure 2-10 shows the damage profile for nickel from several incident heavy ions. Despite the differences in incident energy, the general shape of the heavy ions damage profile remains the same. It can be seen that the damage profile for the nickel increases continuously and peaks around 2 $\mu m$ below the surface. The non-uniformity and Bragg Peak create inhomogeneous damage profiles when compared to high energy protons, which by proper energy selection, can yield uniform damage profiles over many micrometers. Heavy ions would need to be orders of 100 MeVs per nucleon to achieve sufficient penetration to create uniform damage profile over many grain sizes. This would result in very large cyclotrons, which is outside the foreseen design limits of $M^2TF$. This is not the case for protons which can be accelerated to hundreds of MeV with cyclotrons less than 1 m in diameter.

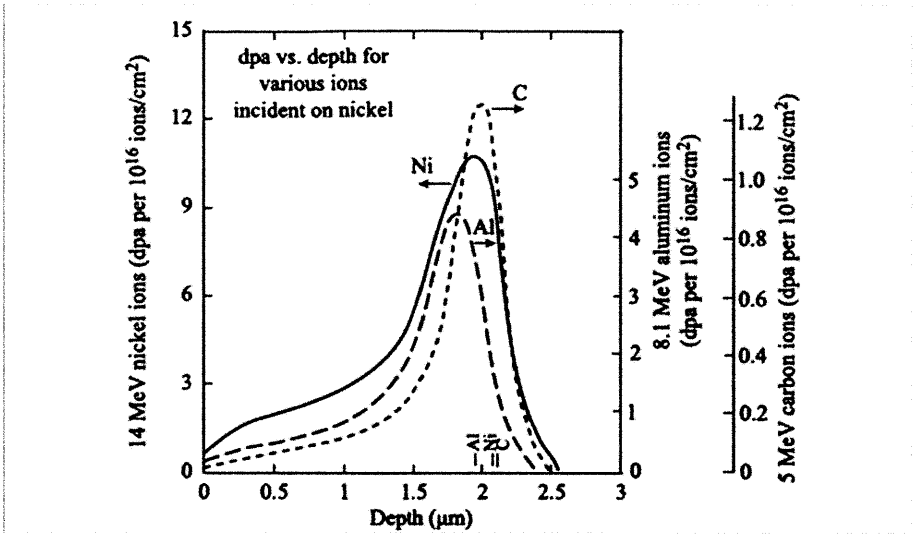


**Figure 2-10: Penetration depth of microns for heavy ions Ni, Al and C. Notice the non-homogenous damage profile over their ~2 micrometer penetration. Figure Adapted from [Sickafus, Kotomin, & Uberuaga, 2007].**

With today's technology, heavy ions lose their advantage over proton acceleration in the simulation of neutron irradiation effects. Current accelerators can achieve high proton currents, lessening the need to employ heavy ions to increase the effective damage rates. Heavy ions were commonly used because they offered high damage rate to heat generation but with the advancement of heat removal systems (such as jet impingement) the damage rate to heat rejection ratio can be increased [San, 1997]. Heavy ion irradiation also causes problems for beam transport. A simple titanium window cannot be used to separate the beam line and target chamber as it could for protons or helium. This is because there would be significant heavy ion range degradation in the window transit [Ziegler & Biersack, 1984]. Therefore, a plasma window must be introduced which adds considerable complexity and cost. Since the advent of light ion radiation, the advantage of uniform deposition and the testing of large samples have experienced more popularity because they offer more macroscopic testing. Due to the advantages of proton irradiation there is no need to employ a heavy ion cyclotron for the M$^2$TF.

# 3 Cyclotrons

A cyclotron is a type of particle accelerator invented by Ernest Lawrence in the 1930s. His idea was to use a magnetic field to accelerate particles in a circle, in order to send them through the same accelerating electrode repeatedly to gradually increase a particle's energy, see Figure 3-1 [Britannica, 2011]. This design greatly reduces the size of the accelerating device compared to that of a LINAC. Lawrence's original design was relatively simple and since then has been modified into complex designs. A cyclotron contains two hollow D-shaped electrodes, called a "dees", separated by a narrow gap to a grounded aperture within a vacuum chamber. The dees are connected to AC current. The chamber, constructed with a non-magnetic material, is placed within the poles of a powerful electromagnet. A source of electrically charged particles is injected at the center of the magnetic field in the center of the chamber. Time varying electric fields applied to the outside of the conductor raise the ion energies as they rotate in the magnetic field and cross the split line gap between the dees [Antaya, 2010]. For a 36 MeV proton, an electric potential difference of 36 MV would be required but since the particle travels through the same electrode repeatedly, the cyclotron can accelerate the proton 10 kV at a time in 1800 steps. As the ions speed up, their radius increases on each successive orbit. At the outer edge of the dees, a deflector plate guides the particles toward the target.

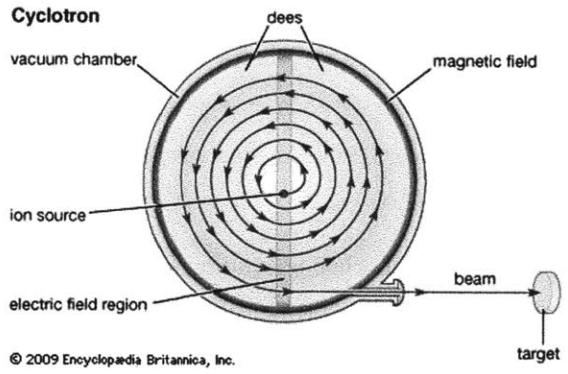


**Figure 3-1: Illustration of a Lawrence Cyclotron components and overall design. Figure adapted from [Britannica, 2011].**

## 3.1 Cyclotron Background

A charge particle will experience a Lorentz force if its motion is perpendicular to a magnetic field. The Lorentz force changes the particles path forcing it to travel centripetally, defining a particular orbit, angular velocity, period, and frequency. The angular velocity ($\omega$) of an ion can be calculated with velocity, v, radius of orbit, r, charge, Q, magnetic field, B, and mass, m.

$$\omega = \frac{v}{r} = \frac{QB}{m} \tag{3.1}$$

Relating angular velocity to angular frequency, f:

$$\omega = 2\pi f \tag{3.2}$$

Angular frequency, f, is:

$$f = \frac{QB}{2\pi m} \tag{3.3}$$

As seen in Equations (3.1) and (3.3), angular velocity and frequency are independent of radius, meaning the ion will cross the split line gap at the same time for every orbit. This consistency allows the application of a time variant electric field used to accelerate the ions across the split line gap. As the ions approach the speed of light their mass increases due to relativistic effects, changing their angular frequency. As the frequency of the ion changes, the ion will no longer cross the split line gap at the same point in the correct voltage cycle for acceleration causing it to decelerate. Modification in the magnetic field with respect to radius or employing a sweeping radial frequency allows particles to be accelerated after significant mass increase. These methods will be further discussed in section 3.2.

The shape of a cyclotron is almost spherical but modeled as a cylinder with cut corners, as seen in Figure 3-2. Its symmetry proves beneficial during calculations allowing it to be modeled in hemispheres (split between the upper and lower coil) and each hemisphere into quarters containing 90° sections, as illustrated in Figure 3-3.

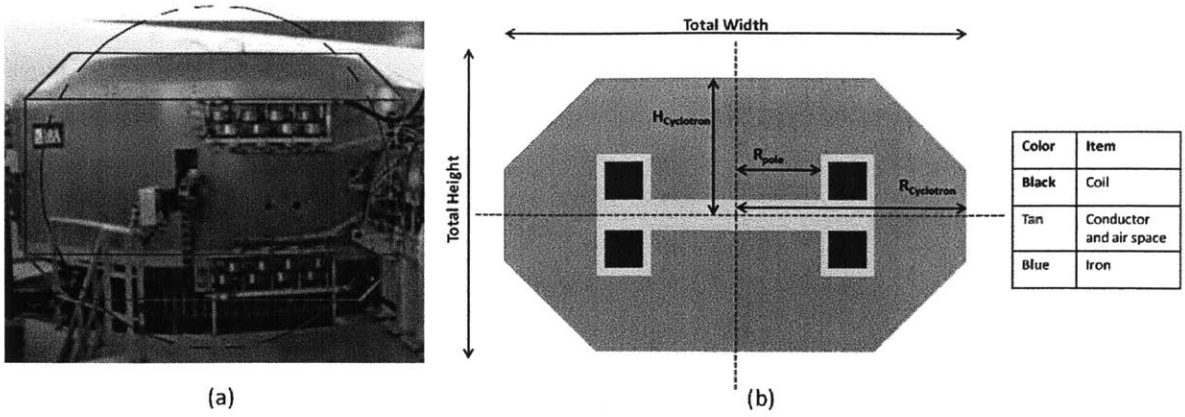


**Figure 3-2: Actual IBA C230 Proton Cyclotron (a) versus model rendition (b). The orientation is as follows: horizontal:radial, vertical:axial, and azimuthal:rotation angle around vertical axis. Figure adapted from [Antaya, 2010].**

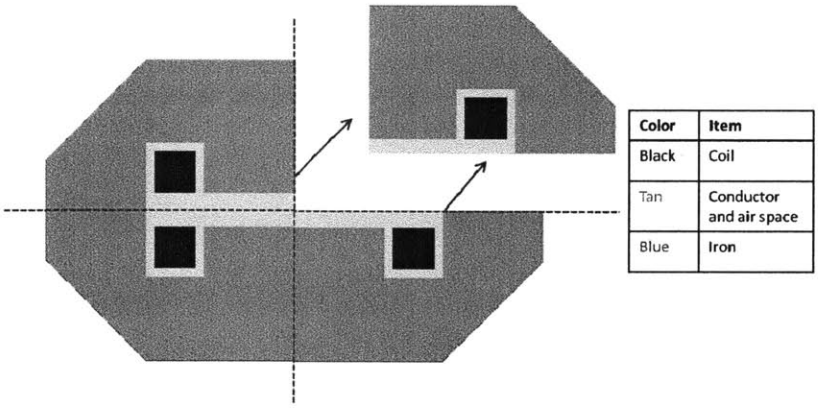


**Figure 3-3: Cut-away view of the cyclotron. This quarter was modeled in Poisson Superfish. The orientation is as follows: horizontal:radial, vertical:axial, and azimuthal:rotation angle around vertical axis.**

Cyclotrons are complex accelerators that consist of hundreds of components, most of which will not be discussed in this thesis. Those important for the following design sections are the: superconducting coil, pole, and yoke. The superconducting coil consists of hundreds of wound Niobium Titanium (NbTi) or Niobium Tin ($Nb_3Sn$) wires. The choice of wire depends on the maximum current density required. The wires are wound in a conductor and placed around the poles of the cyclotron. With a supplied current, these wires generate a magnetic field. There are two total superconducting coils in a cyclotron, one in the top and bottom hemisphere, as seen in Figure 3-2. The poles in a cyclotron are magnetic material (iron or holmium) used to shape the isochronous field. Holmium is used for cyclotrons with central fields above 7T or when orbital stability is low but more commonly iron is used for pole design. The poles are located directly

above the dee conductor and between the superconducting coils, as seen in Figure 3-4. If the cyclotron is isochronous, the poles will no longer be solid cylindrical pieces of iron but broken up to hills and valleys, as see in Figure 3-5. Further explanation for purpose of hills in valleys will be discussed in section 3.2. The yoke of the cyclotron is the remaining iron that surrounds the cyclotron, as seen in Figure 3-4.

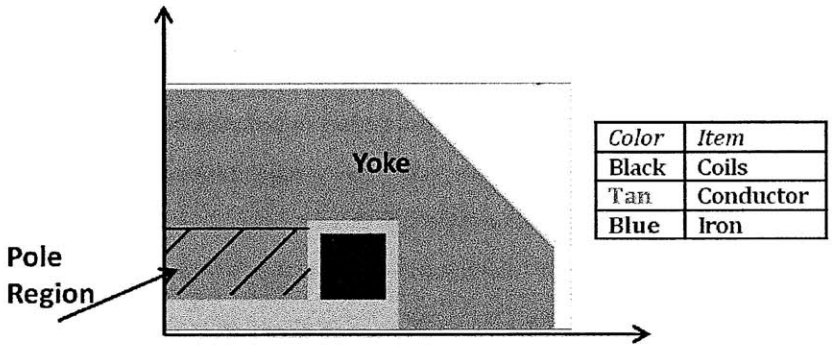


**Figure 3-4: Illustration of the regions of the cyclotron. The orientation is as follows: horizontal:radial, vertical:axial, and azimuthal:rotation angle around vertical axis.**

## 3.2 Cyclotron Selection

There are three different types of cyclotrons: classical, synchrocyclotron, and isochronous. They vary by the mechanisms they use to stabilize and accelerate particles to higher energies. The purpose of the following sections is to explain the selection of the isochronous cyclotron as the baseline $M^2TF$ particle accelerator type.

### 3.2.1 Classical Cyclotron

The classical (Lawrence) cyclotron operates at a fixed frequency and ignores the mass increase that occurs from relativistic effects when ions are accelerated. A classical cyclotron is satisfactory for ions accelerated below 25 MeV because the mass increase is relatively small (< 3%) and the cyclotron frequency increases as 1/M but is insufficient for higher energies [Antaya, 2010]. To demonstrate this limitation, a 36 MeV Proton Lawrence Cyclotron feasibility calculation was conducted.

Equation (3-4) determines the ion rotation difference in radians per turn ($\Delta\varphi$) as mass increases for a Lawrence cyclotron.

$$\Delta\varphi = 2\pi\left[\frac{MB_o}{M_oB} - 1\right] \tag{3.4}$$

$B_o$ and $M_o$ are the field and mass in the center of the cyclotron and B and M occur later after acceleration. Assuming that B is constant for one turn, c is the speed of light in m/s, and v is the velocity of the particle in m/s, for 36 MeV protons the relativistic effect,$\gamma$, is:

$$\gamma = \frac{\mathrm{B}}{\mathrm{B_0}} = \frac{1}{\sqrt{1-\frac{\mathrm{v}^2}{\mathrm{c}^2}}} = 1.0408 \tag{3.5}$$

Substitution of these values in Equation (3.4) results in:

$$\Delta\varphi = 0.232\, rad/turn \sim 13.3^{\circ} \tag{3.6}$$

With $\Delta\varphi$ of 13.3°, it will take 6 turns before the particle would shift to the part of the voltage curve where it would begin to decelerate i.e. a 90° shift; prohibiting its acceleration to 36 MeV. The ion's deceleration is due to the time varying polarity changes of the dees. If the particle is not located in the correct dee at the right time, the dees electric field can decelerate the ion. For a Lawrence cyclotron to accelerate particles to 36 MeV in less than 6 turns it would require 3 MV electric potential difference which is impractical considering the current limit is 10 kV. The Lawrence cyclotron cannot be used for M²TF because it cannot accelerate the particles to the energies required in Table 1-1.

### 3.2.2 Synchrocyclotron

In the synchrocyclotron design, the frequency synchronously matches the increase in mass as the particle accelerates. The synchrocyclotron is very similar to the Lawrence cyclotron but differs because the acceleration at the center is now relativistically corrected, [Antaya, 2010]. If we consider the zero energy ion rotation frequency, $\omega_o$:

$$\omega_o = \frac{qB}{M_o} \tag{3.7}$$

During acceleration, the frequency must decrease proportionally to $\gamma$ to account for the increase in mass according to Equation (3.8):

$$\omega_{rf} = \frac{\omega_o}{\gamma} = \frac{qB}{\gamma M_o} \tag{3.8}$$

Since the frequency is decreasing per turn, it can only accelerate ions a few bunches at a time as the frequency is swept, causing it to have an intrinsically low intensity (particles per second per area) [Antaya, 2010]. To demonstrate this effect, a 4T, 36 MeV Proton Cyclotron frequency calculations will be completed and compared.

For 36 MeV protons the relativistic effect is:

$$\gamma = 1.0408 \tag{3.9}$$

The starting frequency, $f_o$, is:

$$f_o = \frac{\mathrm{eB}}{\mathrm{M}/_{2\pi}} = 60.95\mathrm{Mhz}\ (\mathrm{T} = 16.4\ \mathrm{ns}) \tag{3.10}$$

The final frequency, $f_f$, is:

$$f_f = f_o \frac{1}{\gamma} = 58.6\ MHz\ (\mathrm{T} = 17.1\ \mathrm{ns}) \tag{3.11}$$

The average period for acceleration is around ~16.8 ns. Assuming 10 kV on the dee and 2 gaps per revolution, it will take roughly 1800 orbits to reach full energy. At 16.8 ns average period, one acceleration cycle would take 30 $\mu s$ per bunch, or roughly 33,000 bunches per second. Due to the fact that particles that are being accelerated in bunches per acceleration cycle and not as a continuous wave, the synchrocyclotron is considered low intensity machine. A synchrocyclotron cannot be used for M²TF because of the need of a 'continuous wave' of particles to generate enough intensity to simulate the high flux in a reactor environment, recall Table 1-1.

### 3.2.3 Isochronous Cyclotron

In an isochronous cyclotron, in order to keep the frequency constant, the magnetic field is adjusted to increase with radius to account for the increase in particle mass in accordance with Equation (3.12):

$$B = \gamma B_o \tag{3.12}$$

The energy-mass conservation is used to derive the isochronous field:

$$E^2 = p^2c^2 + E_o^2 \tag{3.13}$$

With substitution of Equation (3.12) into Equation (3.13), the final magnetic field, $B_f$, in terms of rest mass equivalent energy in eV, $E_o$, center magnetic field, $B_o$, and final kinetic energy, $T_f$, is created:

$$B_f = \left(1 + \frac{T_f}{E_o}\right) B_o \tag{3.14}$$

Combing Equation (3.13) and (3.14) results in the isochronous field equation seen in Equation (3.15). For an ion of charge, Z, and atomic mass, A, and extraction radius, r:

$$B = \frac{B_o}{\left[1 - \left(\frac{Z}{A}\right)^2 \left(\frac{r}{\alpha}\right)^2\right]^{1/2}} \tag{3.15}$$

With α:

$$\alpha = \frac{kE_0}{ecB_o} \tag{3.16}$$

A cyclotron must keep ions in orbit through the imposition of radial and axial stability forces. Any loss of particles will generate material activation, degrade the intensity of the beam, and decrease the efficiency of particle extraction. Orbit stability is directly related to magnetic induction, as a function of the radius, classified as the field index [Strijckmans, 2001]. The field index, n, is defined as:

$$n = -\frac{r}{B}\frac{dB}{dr} \tag{3.17}$$

Radial stability ($\nu_x$) is obtained with a field index below unity. Axial stability ($\nu_z$) is achieved with a positive field index. For isochronous machines, the magnetic field increases with radius to compensate for relativistic mass effects, creating a negative field index and thus a lack of axial stability which would result in vertical loss of the particles. To compensate for this, a new axial force must be created to generate a positive axial restoring force. In general the axial or vertical component of the Lorentz force is:

$$F_z = qV_r B_\theta - qV_\theta B_r \tag{3.18}$$

where v is velocity, B is magnetic field, theta is poloidal direction and r is radial direction. Such a force to restore vertical stability can be generated by the shaping of the poles, creating sectors (hill and associated valley) that change the magnetic field in the poloidal direction experienced by the particles as they orbit (see Figure 3-5). Opposed to that of a flat pole having only $B_r$ and $B_z$ components, the magnetic field at the edge of a sector pole is curved allowing the magnetic field to vary with theta ($B_\theta$). With a properly adjusted $B_\theta$ term, the axial restoring force will be positive.

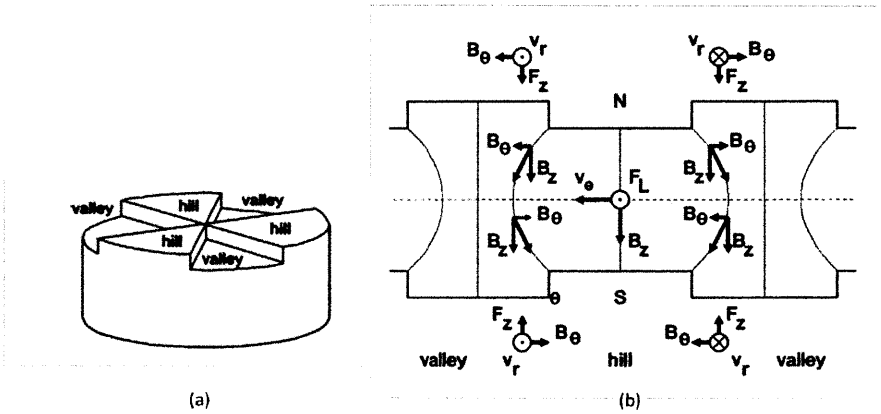


**Figure 3-5: Isochronous design with hills and valleys to create an axial restoring force $F_z$. Representation of polodial variance with hills and valleys, (b). Figure adapted from [Strijckmans, 2001].**

An equilibrium orbit is the orbit of an undisturbed ion that is not accelerated; it is circular with no variations. Equilibrium orbits do not exist in a cyclotron but are only met to define the direction of oscillation of the ion when subjected to an electric and magnetic field. Stable orbits are fully controlled circular-based orbits with small oscillations in the transverse directions (r,z) about equilibrium orbits. These transverse oscillations from the equilibrium orbit are characterized by the vertical ($\nu_z$) and radial ($\nu_r$) frequencies:

$$\nu_z = \frac{\omega_z}{\omega_o} \text{ and } \nu_r = \frac{\omega_r}{\omega_o} \tag{3.19}$$

The motion is characterized by:

$$z = z_o \sin(\upsilon_z \omega_o t) \tag{3.20}$$

$$r = r_o \sin(\upsilon_r \omega_o t) \tag{3.21}$$

For a hypothetical cyclotron to have stable orbits, the vertical frequency, $v_z$, only needs to be positive. For design purposes $v_z > 0.2$ (or $v_z^2 > 0.04$) is chosen allowing for errors in field design. This will insure that the difficulties encountered with magnetic field errors (errors due to improper fabrication or manufacturing of the cyclotrons) will not be encountered in M²TF. Equation (3.22) defines $v_z$ and expresses its relationship with mean squared flutter (F), field index (n), number of sectors (N), and spiral angle ($\xi$).

$$v_z^2 = n + \frac{N^2}{N^2 - 1} F(1 + 2tan\xi) \tag{3.22}$$

Rearranging Equation (3.22) and accounting for $v_z^2 > 0.04$:

$$F\frac{N^2}{N^2 - 1}(1 + 2tan\xi) > n + 0.04 \tag{3.23}$$

Flutter is a mathematical component of magnetic field. Mean squared flutter (F) is calculated from the magnetic field in the z-direction, $B_z$, varying with theta due to the poles:

$$F = \frac{1}{2} f^2 \; where \; f = \frac{B_{peak} - B_{valley}}{\langle B \rangle} \tag{3.24}$$

Increasing spiral angle, the angle between the radius vector and the line tangent to the spiral curve, and decreasing the number of sectors to a minimum of three allows for the stability requirements in Equation (3.23) to be met more easily. The above characteristics will become increasingly important in the cyclotron design section.

Although the isochronous cyclotron is more complex in design, it is a continuous wave (CW) machine with the capability of variable energy by altering the RF frequency and isochronous field. It is also the most commonly built cyclotron in the world today and the choice for the M²TF.

## 3.3 Addressing the Concern of Damage Cascade Timescales

As mentioned earlier, accelerator based radiation damage can be accumulated much faster than real time. Proton irradiation can take about 1/10 the time of neutron irradiation due to high damage rates of the impinging proton beam. This can lead to heat removal issues and damage profiles that are significantly different than real time neutron damage. High damage rates can lead to overlapping and interfering damage cascades that could affect damage physics and contribute to

unrealistic damage effects [Barnard, Ferry, & Payne, 2010]. To determine if this could be an issue for M²TF, the time between displacements must be calculated from the instantaneous current and compared with the timescales of different damage related events.

A 4T, 36 MeV isochronous proton cyclotron has a frequency around 60 MHz. A 60 MHz machine sends a bunch of charged particles $6x10^7$ times/sec (a period of 16 ns). Since the accelerating voltage wave consists of troughs and crests, only part of the wave can be used for acceleration creating a burst of particles. A burst of particles 1.6 ns wide (~10% of the period) generates an instantaneous current that is higher than the average [Antaya, 2010]. To determine the instantaneous rate of current a few calculations must be completed. An average current of 0.1 mA corresponds to $6.24x10^{14}$ protons/sec. A 60 MHz frequency is also the frequency of the instantaneous bursts of particles, $6x10^7$ burst/sec. By dividing the two values, the number of protons per burst can be determined:

$$\frac{6.24x10^{14}\left[\frac{\text{Protons}}{\text{sec}}\right]}{6x10^{7}\left[\frac{\text{Burst}}{\text{sec}}\right]} = 1.04x10^{7}\left[\frac{\text{Protons}}{\text{Burst}}\right] \tag{3.25}$$

The instantaneous current, $I_{instant}$, is the value from Equation (3.25) divided by the width of the burst in seconds, approximately 1.6 ns:

$$I_{instant} = \frac{1.04x10^{7}\left[\frac{\text{Protons}}{\text{Burst}}\right]}{1.6x10^{-9}\left[\frac{\text{sec}}{\text{Burst}}\right]} = 6.5x10^{15}\left[\frac{\text{Protons}}{\text{sec}}\right] \tag{3.26}$$

There are $6.24x10^{18}$ protons/sec in one Amp and 1000 mA in one Amp:

$$I_{instant} = \frac{6.5x10^{15}\left[\frac{\text{Protons}}{\text{sec}}\right]}{6.24x10^{18}\left[\frac{\text{Protons}}{\text{sec}}\right]} = 1.04\text{mA} \tag{3.27}$$

The instantaneous current is one order of magnitude larger than the average current in a 36 MeV Isochronous Proton Cyclotron at 60 MHz operating frequency and 0.1mA/cm² beam intensity.

The timescale for the damage cascade recovery for an instantaneous current density must be calculated to determine whether another cascade is generated in the displaced volume without the former reaching equilibrium. Table 3-1 lists the timescales for different damage related events. In order to have an accurate representation of damage, the cyclotron generated cascade timescale

must be longer than $10^{-8}$ seconds. The time between displacements can be calculated from the volumetric displacement rate and the volume of the displacement cascade. The process is approximated by the range and lateral straggling of the PKAs [Barnard, Ferry, & Payne, 2010]. For more information on the calculation of the mean time between displacements refer to "TSTARC: The Site for Testing of Advanced Reactor materials" [Barnard, Ferry, & Payne, 2010].

The mean time between displacements was calculated for 1 mA/cm$^2$ instantaneous current density and then graphed in Figure 3-6 with the timescales for damage related events superimposed. As seen in Figure 3-6, the time between displacements is 2-3 orders of magnitude longer than $10^{-8}$ seconds; more specifically, on the order of microseconds. This indicates that after the initiation of a damage cascade, all of the damage processes, including the formation of a PKA, its energy dissipation, and finally recombination and thermal migration of defects, will have time to reach equilibrium before the next cascade is initiated within that volume [Barnard, Ferry, & Payne, 2010]. It is thus concluded that time structure, when using an isochronous cyclotron, will create no issues related to damage cascade overlap.

**Table 3-1: Timescale for damage related events. Figure adapted from [Was G. S., 2007].**

| Timescale[s] | Event |
|---|---|
| $10^{-18}$ | Energy transfer from incident particle: formation of primary knock-on (PKA) atom. |
| $10^{-13}$ | Displacement of lattice atoms by PKA: Displacement cascade. |
| $10^{-11}$ | Energy dissipation, recombination and clustering: Formation of stable Frenkel pairs. |
| $> 10^{-8}$ | Thermal migration: Interstitial-vacancy, recombination,clustering, trapping, defect emission. |

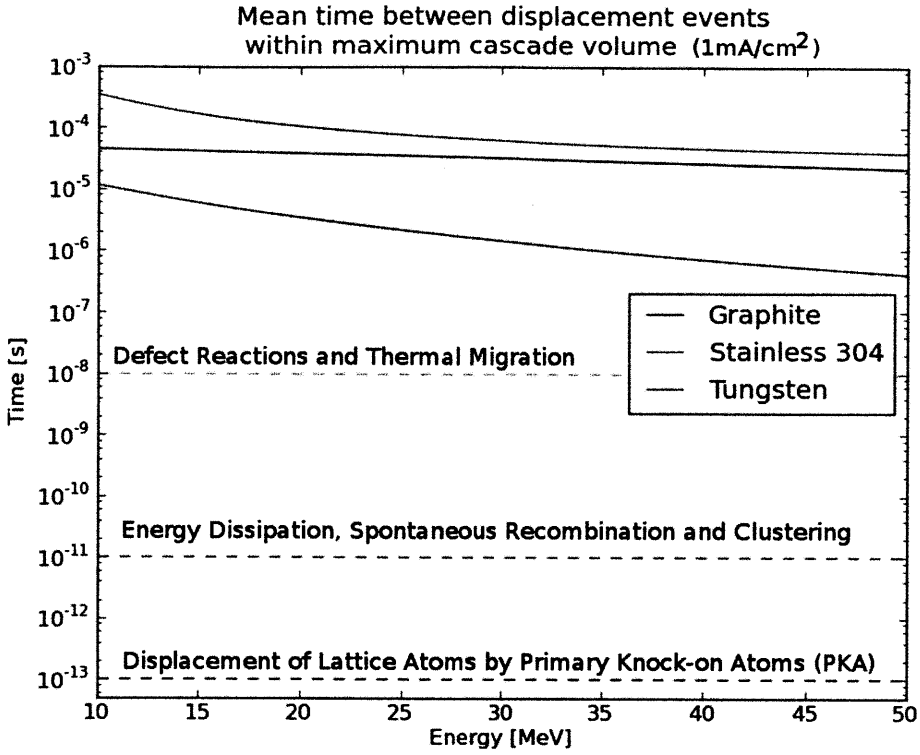


**Figure 3-6: Mean time between Displacements for Graphite, SS and Tungsten with overlay of important timescales of damage related events.**

## 3.4 Cyclotron Design and Analysis

### 3.4.1 Operation Limits and Feasibility Table

The choice of a 3-7T 36MeV Proton and 100 MeV Helium Cyclotron was based on a set of requirements for the overall facility described in section 1.4 and identified in Table 1-1 and Table 1-2. While expanding the envelope in some areas, the overall design needed to be generally consistent with the characteristics of current operating cyclotrons, Table 3-2. By choosing a cyclotron of similar field and energy it was believed that this path reduces the chance of design and operation issues. Table 3-2 shows the characteristics of a cyclotron with high field and energy (Still River PBRT), a high field and a low energy (DTRA Demo), and a low field with high energy (ACCEL-250). The range of current cyclotrons characteristics suggests that an average field (3-6T), low energy (below 100 MeV) cyclotron could be built successfully with minimum design issues.

The strength of the field is inversely proportional to the size of the cyclotron. In general, as the field increases, the size decreases, reducing cost but this generalization is not without limits. These

additional cost issues will be discussed in the section 3.6. The high magnetic field advantages do not come without some collateral issues. Cyclotrons with high fields (above 7T) create a new set of challenges. Since the magnetic saturation limit for iron is around 2T, maintaining and controlling the stability of the particle becomes difficult for compact, high field machines (DTRA Demo and Still River PBRT) [Antaya, 2010]. For the M²TF design, the decision was made to limit the maximum magnetic field to 6-7T to avoid the practical implications on ion stability. A design of maximum field of 7T will still be attempted to analyze the cost and weight savings of a more compact, high field cyclotron.

**Table 3-2: Comparison of current cyclotron magnetic field and energy.**

| Cyclotron | Energy | Magnetic Field | Type | Uses | Unique |
|---|---|---|---|---|---|
| ACCEL-250 | 250 MeV (i) | 2.4T | Isochronous | PT | SC |
| C-230/235 (IBA) | 235 MeV (p) | 1.739-2.165T | Isochronous | PT | Non SC |
| C-400 | 265 MeV (p), 400 MeV (i) | ~3.5T | Isochronous | PT | SC |
| M²TF (Not built) | 36 MeV (p), 100 MeV (He) | 4-7T (p), 4-7T (He) | Isochronous | MTF | SC |
| DTRA Demo | 10 MeV (p), 5 MeV (d) | 7T | Isochronous | DTRA | SC |
| Still River PBRT | 250 MeV (p) | 9T | Synchronous | PT | SC |

PT=Proton Therapy, MTF=Material Test Facility, DTRA=Detection Threat Reduction Agency, SC=Superconducting

## 3.4.2 Basic Scaling with Poisson Superfish

Basic scaling studies of cyclotron fields and sizes were performed with the code Poisson Superfish in order to generate a starting model [LAACG, 1976]. As stated above, one of the design requirements for the system is to be university-size and cost effective. Poisson was able to provide a rough estimate on the size of the cyclotron. With the size, the overall cost could be estimated from the characteristics of the coils, conductor, amount of iron and other components. Such data provides a great foundation before employing more complex codes to refine the cyclotron designs. Due to their complexity, isochronous cyclotrons require 3D magnetic field designs.

### 3.4.2.1 Poisson Program

Poisson Superfish is a collection of programs for calculating static magnetic and electric fields and radio-frequency electromagnetic fields in either 2D Cartesian coordinates or axially symmetric cylindrical coordinates. Poisson Superfish solves the Poisson's equation on a 2D grid generated by

boundaries of the coil, pole, and yoke, as seen in Figure 3-4 [LAACG, 1976]. The program generates a triangular mesh fitted to the boundaries of different materials in the problem geometry, calculates the electrostatic or magnetic potentials on this mesh as desired, and computes derivatives of the potentials to obtain the electric and magnetic fields. It then can output the resulting data in a multitude of different forms including images, contour plots, and generic B vs. R plots. Poisson is a free code that is maintained by the U.S. Department of Energy and supported by the Los Alamos National Laboratory System.

### 3.4.2.2 Boundary Conditions Applied in Poisson

The choice was made to model only a quarter of the cyclotron in cylindrical coordinates taking advantage of the cyclotrons overall cylindrical symmetry. A cut-away image of cyclotron modeled in Poisson is shown in Figure 3-3. Application of symmetry saves time in calculations; however boundary conditions must then be applied. The required boundary conditions must specify whether the magnetic fields are perpendicular (Neumann condition) or parallel to the reference axis (Poisson condition). Figure 3-7 illustrates the proper parallel and perpendicular boundary conditions as applied to the cyclotron modeling problem in Poisson.

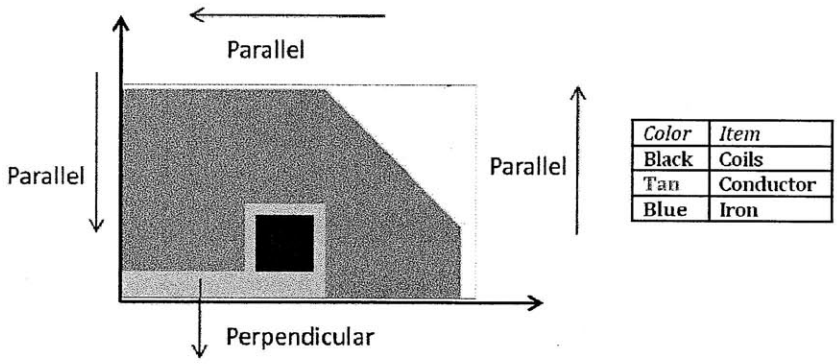


**Figure 3-7: Illustration of the Neumann and Poisson boundary conditions for magnetic fields applied in Poisson Superfish.**

Due to the boundary conditions and symmetry applied to the 2D Poisson model, the 3D nature of the hills and valley of the pole design could not be represented without a stacking factor. A stacking factor is a function used in Poisson to assign material composition in a certain region. For this case it was used to represent the solid hills and empty valleys of the pole design, as seen in Figure 3-5. The assumption was made that there was a 1 to 1 volume ratio of air in valleys to iron poles. In Poisson, this resulted in a stacking factor of 50%. The stacking factor region was located above the conductor and between the coils and is illustrated in Figure 3-8. A schematic of Michigan

State University's K500 superconducting cyclotron poles tips are also shown at the top of Figure 3-8 for illustration purposes [MSU, 2011].

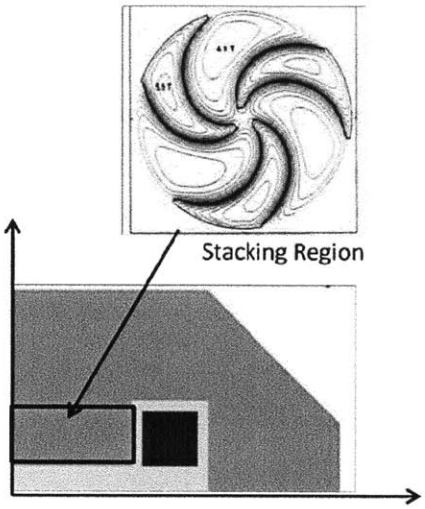


| *Color* | *Item* |
|---|---|
| Black | Coils |
| Tan | Conductor |
| Blue | Iron |

**Figure 3-8: Stacking region (black square region) modeled in Poisson and spiral pole tip design from K500 cyclotron. Above figure adapted from [MSU, 2011].**

### 3.4.2.3 Calculations for Inputs

The minimum orbit radius is the radius necessary for the selected ion to achieve the desired output energy of 36 MeV (protons) or 100 MeV (helium). Each orbit radius is dependent on the strength of the magnetic field. The stronger the magnetic field, the smaller the radius. Calculations for the orbit radius for a given energy begin with the isochronous field equation, Equation (3.15). The term $\left(\frac{Z}{A}\right)$ is set equal to 1 for protons (Z=A=1) and 1/2 for helium ions (Z=2,A=4). Solving for $r_{extraction}$, the final equation is:

$$r_{extraction} = \sqrt{\left(\frac{A}{Z}\right)^2 \alpha^2 \left(1 - \frac{1}{\gamma^2}\right)} \tag{3.28}$$

The maximum current for the coils was determined by the area of the coil and the maximum current density. A maximum current density of 20,000 Amps/cm2 was adopted as a conservative starting density for superconducting coils. This value has been used in most current operating superconducting cyclotrons . Knowing the coil area, an input current could be determined.

Table 3-3 and

Table 3-4 list the initial and final magnetic field and extraction radius for each respective particle as a function of increasing magnetic field; recalling that the definition of alpha from Equation (3.16).

The maximum current for the coils was determined by the area of the coil and the maximum current density. A maximum current density of 20,000 Amps/cm$^2$ was adopted as a conservative starting density for superconducting coils. This value has been used in most current operating superconducting cyclotrons [Antaya, 2010]. Knowing the coil area, an input current could be determined.

**Table 3-3: Proton cyclotron basic sizing calculations.**

| $B_o$ (T) | α (m) | $B_f$ (T) | $R_{extraction}$ (m) |
|---|---|---|---|
| 1 | 3.138 | 1.037 | 0.830 |
| 1.5 | 2.092 | 1.555 | 0.553 |
| 2 | 1.569 | 2.074 | 0.415 |
| 2.5 | 1.255 | 2.592 | 0.332 |
| 3 | 1.046 | 3.111 | 0.277 |
| 3.5 | 0.897 | 3.629 | 0.237 |
| 4 | 0.785 | 4.148 | 0.208 |
| 4.5 | 0.697 | 4.666 | 0.184 |
| 5 | 0.628 | 5.185 | 0.166 |
| 5.5 | 0.571 | 5.703 | 0.151 |
| 6 | 0.523 | 6.222 | 0.138 |
| 6.5 | 0.483 | 6.740 | 0.128 |
| 7 | 0.448 | 7.259 | 0.119 |

**Table 3-4: Helium cyclotron basic sizing calculations.**

| $B_o$ (T) | α (m) | $B_f$ (T) | $R_{extraction}$ (m) |
|---|---|---|---|
| 1 | 3.115 | 1.026 | 1.397 |
| 1.5 | 2.077 | 1.539 | 0.932 |
| 2 | 1.558 | 2.052 | 0.699 |
| 2.5 | 1.246 | 2.565 | 0.559 |
| 3 | 1.038 | 3.078 | 0.466 |
| 3.5 | 0.890 | 3.591 | 0.399 |
| 4 | 0.779 | 4.105 | 0.349 |
| 4.5 | 0.692 | 4.618 | 0.311 |
| 5 | 0.623 | 5.131 | 0.279 |
| 5.5 | 0.566 | 5.644 | 0.254 |
| 6 | 0.519 | 6.157 | 0.233 |

| | | | |
|---|---|---|---|
| 6.5 | 0.479 | 6.670 | 0.215 |
| 7 | 0.445 | 7.183 | 0.200 |

#### 3.4.2.4 Optimization of Poisson Procedure

Unfortunately Poisson does not have an optimization capability built in. Optimization must be done by manual user changes in current, coil area, pole and yoke dimensions. Basic scaling laws for cyclotron design are: the height of the cyclotron should be 60% of its radius and the cyclotron radius should be 65% poles, 15% coil, 20% yoke (please refer to Figure 3-2b) [Antaya, 2011]. These above values are only approximations, but they guide the user through the initial design stages. Figure 3-2 illustrates the parts of the cyclotron and terms referenced and created for this analysis. The associated table gives color codes as to the components of the cyclotron.

The process for modeling the 3, 5, and 7T proton and helium cyclotrons went as follows. First, the radius of extraction was inputted. This value could not be changed because it is the minimum radius needed for acceleration. If it is shortened then the particle will not reach full energy. The coil height and width was inserted. The restriction 20,000 Amps/cm$^2$ current density was applied. Simple arithmetic relates current, coil area and density. The input current, amount of iron, and coil area, were adjusted until the origin of the magnetic field was the desired $B_o$ for a given final orbital radius, the outer boundary of iron was not saturated (<2T), and did not generate a strong fringe field. The fringe field outside the yoke was designed to be less than 100 Gauss. Fringe fields are magnetic fields that extend away from the confines of the magnet. High fringe fields have the ability to interfere with extracted beams trajectories, ruin sensitive equipment, and magnetize ferrous based instruments and tools.

#### 3.4.2.5 2D Poisson Results

The results from modeling the 3, 5, and 7T designs for both proton and helium cyclotrons are presented in their respective sub-sections (3.4.2.5.1- 3.4.2.5.7). A table has been provided for each cyclotron indicating its target field, pole radius, cyclotron radius, cyclotron height, and total size. The red direction arrows in each figure represent the magnetic field direction and strength. The larger the arrow indicates a stronger field. The horizontal line from the y-axis to the top of the coil represents the boundary line of the stacking factor region.

#### 3.4.2.5.1 Proton 3T Cyclotron

| Poisson's Inputs | |
|---|---|
| Target Field | ~3T |
| Pole Radius | 27.5 cm |
| Cyclotron Radius | 41.5 cm |
| Cyclotron Height | 21.5 cm |
| **Poisson's Outputs** | |
| Total Width | 83 cm |
| Total Height | 43 cm |

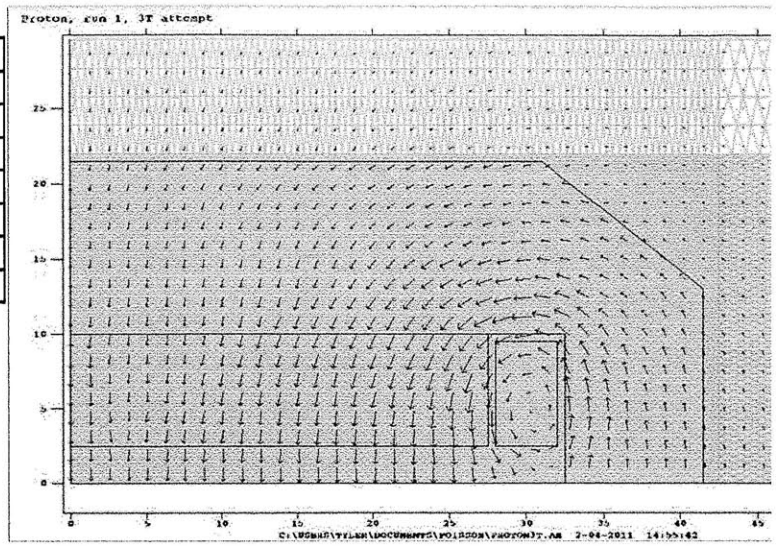


**Figure 3-9: Proton 3T Poisson result. Horizontal axis radius from 0-45 cm, vertical axis height from 0-30 cm. Red arrows length: strength and direction of B field (3T at origin).**

#### 3.4.2.5.2 Proton 5T Cyclotron

| Poisson's Inputs | |
|---|---|
| Target Field | ~5 T |
| Pole Radius | 16.5 cm |
| Cyclotron Radius | 28 cm |
| Cyclotron Height | 19 cm |
| **Poisson's Outputs** | |
| Total Width | 56 cm |
| Total Height | 38 cm |

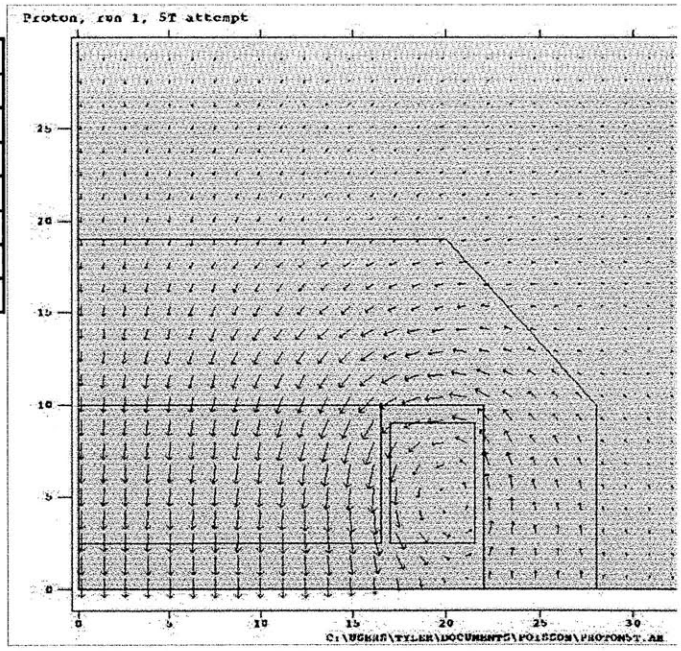


**Figure 3-10: Proton 5T Poisson result. Horizontal axis radius from 0-35 cm, vertical axis height from 0-30 cm. Red arrows length: strength and direction of B field (5T at origin).**

#### 3.4.2.5.3 Proton 7T Cyclotron

| Poisson's Inputs | |
|---|---|
| Target Field | ~7 T |
| Pole Radius | 12 cm |
| Cyclotron Radius | 24 cm |
| Cyclotron Height | 20.5 cm |
| **Poisson's Outputs** | |
| Total Width | 48 cm |
| Total Height | 41 cm |

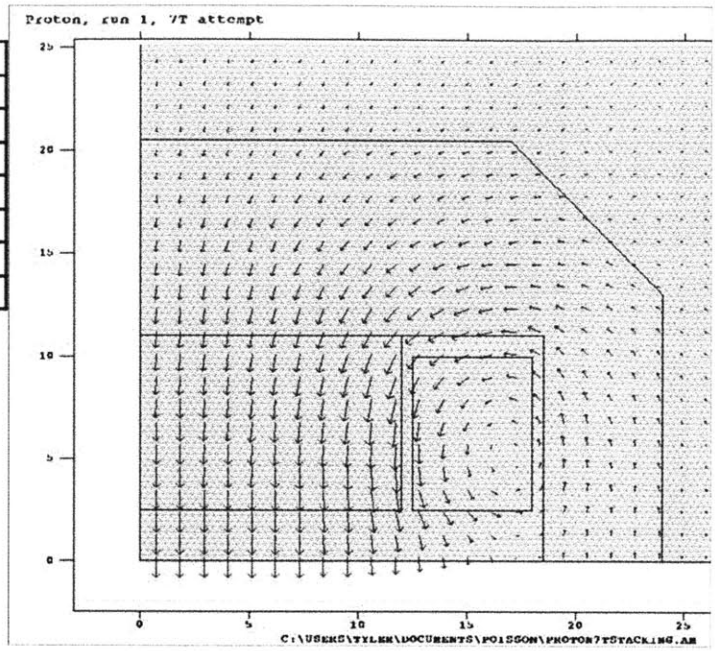


**Figure 3-11: Proton 7T Poisson result. Horizontal axis radius from 0-25 cm, vertical axis height from 0-25 cm. Red arrows length: strength and direction of B field (7T at origin).**

#### 3.4.2.5.4 Helium 3T Cyclotron

| Poisson's Inputs | |
|---|---|
| Target Field | ~3T |
| Pole Radius | 46.5 cm |
| Cyclotron Radius | 74 cm |
| Cyclotron Height | 35 cm |
| **Poisson's Outputs** | |
| Total Width | 148 cm |
| Total Height | 70 cm |

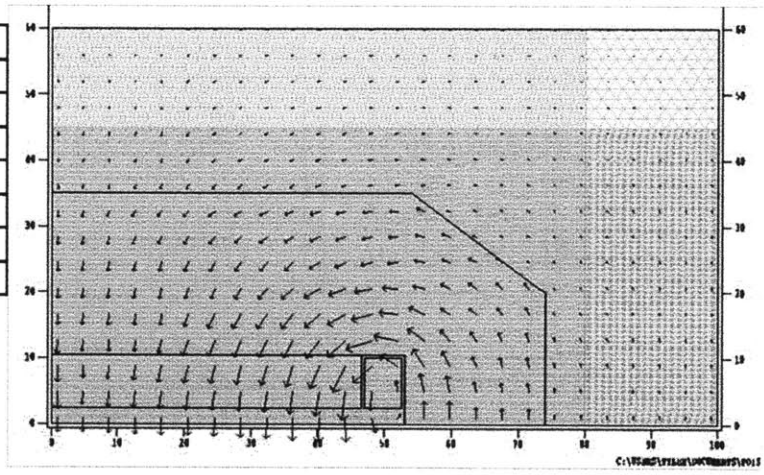

**Figure 3-12: Helium 3T Poisson result. Horizontal axis radius from 0-100 cm, vertical axis height from 0-60 cm. Red arrows length: strength and direction of B field (3T at origin).**

#### 3.4.2.5.5 Helium 5T Cyclotron

| Poisson's Inputs | |
|---|---|
| Target Field | ~5T |
| Pole Radius | 28 cm |
| Cyclotron Radius | 46 cm |
| Cyclotron Height | 27 cm |
| **Poisson's Outputs** | |
| Total Width | 92 cm |
| Total Height | 54 cm |

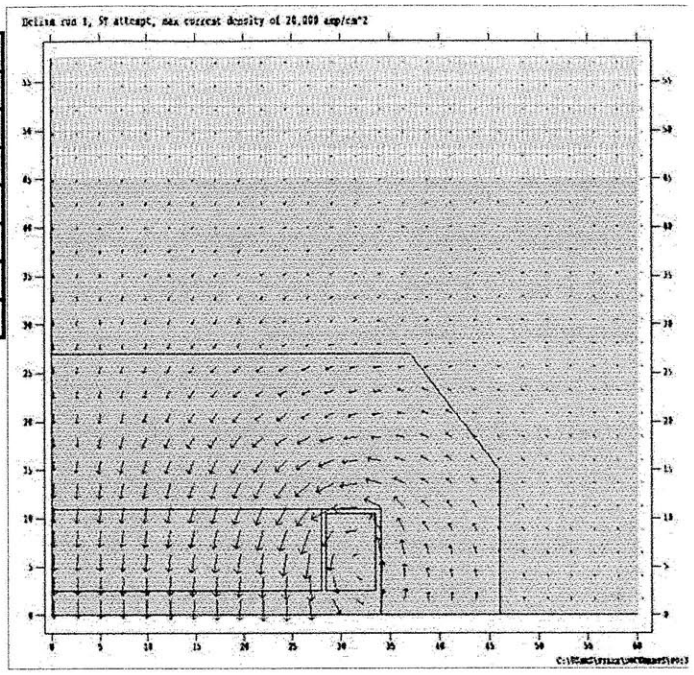

**Figure 3-13: Helium 5T Poisson result. Horizontal axis radius from 0-60 cm, vertical axis height from 0-60 cm. Red arrows length: strength and direction of B field (5T at origin).**

#### 3.4.2.5.6 Helium 7T Cyclotron

| Poisson's Inputs | |
|---|---|
| Target Field | ~7 T |
| Pole Radius | 20 cm |
| Cyclotron Radius | 38 cm |
| Cyclotron Height | 26 cm |
| **Poisson's Outputs** | |
| Total Width | 74cm |
| Total Height | 52 cm |

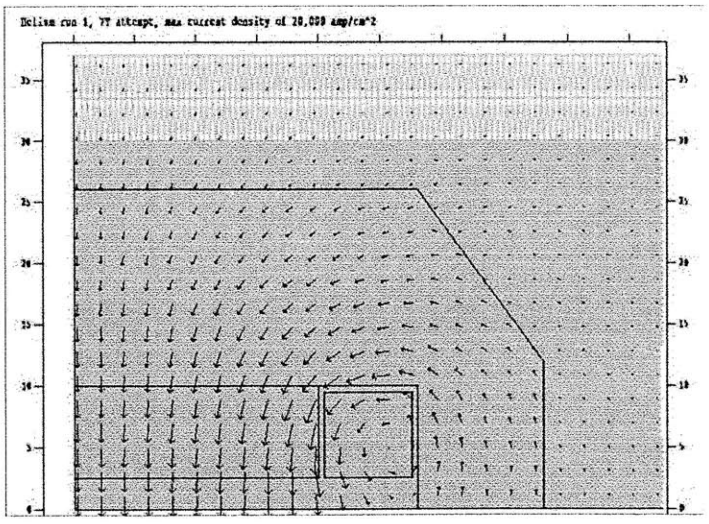

**Figure 3-14: Helium 7T Poisson result. Horizontal axis radius from 0-50 cm, vertical axis height from 0-35 cm. Red arrows length: strength and direction of B field (7T at origin).**

#### 3.4.2.6 Discussion of Results

The results show that as the magnetic field increases, the overall size decreases. Since this is designed to be a university-sized machine, the smaller the cyclotron the better. Smaller size, due to less iron, also relates to a smaller cost (in most cases). Additionally, even higher magnetic field cyclotrons might require the uses of holmium in order to shape the magnetic field when addressing 3D issues. Holmium is unique in that it saturates magnetically at 3.0T, whereas iron saturates around 2.06 T. Holmium also costs almost 60 times as much as iron. From these observations and findings, the decision was made to start designing a 5T machine for both particles and then advance in field to attempt to reduce size and cost.

### 3.4.3 Code Used for Comprehensive Design

The two codes used to further refine the design and optimizations of both cyclotrons were *Acfields* and Opera-3D (Operating Environment for Electromagnetic Research and Analysis).

#### 3.4.3.1 *Acfields*

With the motivation of reducing iteration time in the design of isochronous superconducting cyclotrons, Robert Block for the PSFC Technology and Engineering division created *Acfields*, a Python and Fortran based code [Block, 2011]. Similar to Opera-3D and Poisson, *Acfields* is used to determine approximate size, power, and cost for a cyclotron in 3D. The code also calculates important magnetic properties that are needed to determine the stability of the particle's orbit including the flutter, isochronous field, and $\nu_z$.

*Acfields*, a hybrid field modeling code, works on the assumption that the hills (recall Figure 3-5) of a high field cyclotron have reached their magnetic saturation. This assumption can only be applied for high field cyclotrons since iron saturates at 2T. Magnetic saturation allows for the use of Davies' uniform magnetization approximation when calculating magnetic fields [Lee-Whiting & Davies, 1994]. The approximation allows for a volume integral to be transformed to a surface integral, reducing computation time to only a few minutes, 20-200 times faster than Opera-3D [Block, 2011].

The code organization is very straight forward and simple. The organization below has been taken from the *Acfields* Report [Block, 2011].

1. User specifies several curves that define the cyclotron pole shape and a map of field points for integration.

2. Code integrates fields at all points provided.
3. User generates radial map of coil+yoke fields from another field code. Input as Opera-style .table file of B vs.r.
4. Code generates moments-based approximation for yoke field for fast recovery of field.
5. Yoke, coil, and pole fields are summed together for final processing which includes plotting, cyclotron parameter calculation, etc.

The cyclotron parameter calculations used from the M²TF analysis are the frequencies $v_z$, $v_r$, isochronous field, and the flutter field. Later, the code was slightly modified to plot minimum flutter and $v_z$. The *Acfields* code data for both cyclotrons can be seen in Appendix A.

#### 3.4.3.1.1 Design restrictions and limitations of *Acfields*

*Acfields* underestimates the field contribution of any full ring of magnetic material. The ring, when modeled in Opera-3D, contributes a higher magnetic contribution, raising the overall isochronous field by a few hundred Gauss. *Acfields* also began to break down when complex pole geometries were introduced. Tight spiral angles with many cuts caused errors in the mesh due to the creation of infinitely sharp points. Applying a smaller mesh or slight changes in the spiral angle would sometimes fix this problem. *Acfields* must accept a yoke field in order to begin calculations. The coil and yoke do not change frequently during iterations, so it is not worthwhile to import their calculation to Python or Fortran [Block, 2011]. This acceptance only becomes an issue during the initial stages of design when the size of the yoke and coil are still unknown. Many designs were infeasible from the beginning when a small yoke was chosen that didn't allow proper coil placement or if magnetic yoke field contribution was too strong.

### 3.4.3.2 Opera 3D

Opera-3D is a comprehensive electromagnetic analysis program used widely in the scientific community. It consists of a 2D and 3D modeling program as well as a pre and post processer program to prepare and analyze data [Opera-3d, 2009]. For this project, Opera 3D was first used to for cyclotron design and optimization, but due to the long time between iterations, it was later utilized only to verify results from *Acfields*.

Opera-3D Geometric Modeller and Pre-Processor provide the facilities for the creation of the finite element models, complicated geometry, solenoids, and the definition of materials [Opera-3d, 2009]. The modeller operates much like other CAD programs, such as SolidWorks. One is able to manipulate, rotate, cut, and duplicate objects with relative ease. The Modeller also allows the user

to import certain AutoCAD and SolidWorks files. These files can be imported into the workspace and assigned material properties, skipping the geometric modeling process. Importing is more acceptable when dealing with complex designs or when optimizing an object through iterations. Opera-3D files are very large and its rebuild function tends to frequently malfunction. The Opera-3D Pre-Processor is a program designed to edit 3D finite elements models, assign boundary conditions, apply symmetry, define material characteristics (for non-linear magnetic or dielectric components), select mesh size and define the number of nodes per cell [Opera-3d, 2009]. The Pre-Processor is the most important stage of cyclotron design and optimization.

The Opera-3D Post-Processor displays calculations on results from electromagnetic field analysis programs including CARMEN, DEMAG, ELEKTRA, QUENCH, SCALA, SOPRANO, TEMPO and TOSCA [Opera-3d, 2009]. Table 3-5 provides a short summary of the analysis conducted by each Opera-3D program.

**Table 3-5: Summary of Analysis Conducted by Opera-3D Programs.**

| Program | Analysis Conducted |
|---|---|
| CARMEN | Motion |
| DEMAG | Magnetization of Permanent Magnets |
| ELEKTRA | Time Varying |
| QUENCH | Superconducting Coil |
| SCALA | Space Charge |
| SOPRANO | High Frequency |
| TEMPO | Static and Transient Thermal |
| TOSCA | Static Field |

For cyclotron analysis, TOSCA was applied. TOSCA calculates current flow, magnetostatics fields, and electrostatic fields based on Scalar Potential Formulation derived from the input and specifications of the conductor and conductor current [Opera-3d, 2009]. The Post-Processor is a utility that allows viewing of the finite element data, point data, contour graphs, as well as body forces and trajectory calculations. Data can be extracted by point, line, plane, zone, or polar patch creating a "data.table" file. The file format is Fortran like; therefore hard to manipulate, extract, and use if one is not employing Fortran. Programs like Matlab can read and recognize the file but have trouble organizing it into matrix or vector forms. With some minor manipulation and extraction limits, isochronous fields and flutter calculations can be completed with any data manipulation software of choice.

Please refer to Appendix B and Appendix C for both Opera-3D instructions and the Matlab code for data manipulation.

#### 3.4.3.2.1 Design restrictions and limitations of Opera-3D

Opera-3D is a very powerful program that computes an in-depth accurate analysis of electromagnetic properties. The program is relatively easy to use but requires manipulation in order to minimize computation time. A few methods are described below.

Due to the cyclotron's cylindrical overall shape, almost all aspects are cylindrically symmetric. The cyclotron can be split in half, between the coils. Depending on the number of sectors, the cyclotron can be cut up into that number of sections. For example, a 4 sector pole structure can be broken into four 90 degree sections. Applying these symmetries greatly reduces computation time.

Mesh size directly relates to computation time and accuracy. Opera-3D will recommend certain mesh sizes when applying the surface and volume mesh in the Geometric Modeller and Pre-Processor. These are acceptable meshes for an accurate analysis; however, it will take hours to arrive at the Post-Processor solution. It is recommended to apply a small mesh to the cyclotron iron components and an air gap between while applying a large mesh to the surrounding boundary sphere. No mesh is need for the conductor or solenoid. The mesh selected for both cyclotrons was around 1 to 2 cm. When the mesh becomes too large the gradient between a junction of a small mesh and large mesh is too large and cannot be converged. Small radii, sharp points, and splines cannot mesh accurately because Opera-3D assigns nodes to every corner. If the mesh is too large, it cannot fit between the nodes, resulting in a Pre-Processor error.

Opera-3D has trouble computing spiral poles as opposed to radial sectors. The overall radial isochronous field is the same whether the design is spiral or sector because the area exposed for each radius is the same. The difference arises in flutter and stability calculations. One would assume that a spiral shaped sector would yield the same results in Opera-3D and this assumption is approximately correct if the mesh size is extremely small and if there are no symmetry conditions applied. Due to tight spiral angles, the poles are relatively close together, therefore requiring a smaller mesh. A 3 pole cyclotron would be divided into 120 degree sections regardless of a spiral orientation or not. When applied to a spiral based cyclotron, the resulting isochronous field is incorrect in magnitude. Possible causes could be due to Opera-3D's inability to distinguish hill from valley when spiral angles were very tight. This also stems from Opera-3D computation method. Opera-3D selects a certain point in a mesh, completes an analysis, and then chooses a point nearest

to its first point's location [Opera-3d, 2009]. It keeps selecting points and modeling them as small cubes until there is a convergence on similar value. Once converged, Opera will then continue to another section of geometry. Figure 3-15 describes an exaggerated effect of what is described above and is only meant to clarify an extremely complicated process. If points 1 through 4 are selected and converge, then the importance of the geometry surrounding point 5 will be ignored.

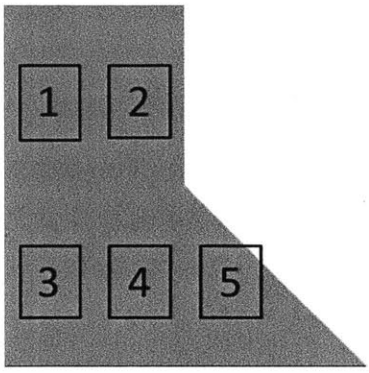


**Figure 3-15: Possible example of Opera-3D grouping error. Zones 1-4 will converge correctly and satisfy Opera-3D iteration program causing it to continue to another sector of geometry, diminishing zone 5's geometric importance.**

## 3.4.4 Proton Cyclotron

### 3.4.4.1 Design Issues

Table 3-6 provides selected extraction radii and final magnetic fields for a 5, 6, and 7T proton cyclotrons with a final energy of 36 MeV. This table will be referenced repeatedly in the following sections in order to express in more detail some encountered design issues.

**Table 3-6: Selected values of interest for radius of extraction for an Isochronous 36 MeV Proton Cyclotron.**

| $B_o$ (T) | $\alpha$ (m) | $B_{final}$ (T) | $R_{extraction}$ (m) |
|---|---|---|---|
| 5 | 0.628 | 5.185 | 0.166 |
| 5.5 | 0.571 | 5.703 | 0.151 |
| 6 | 0.523 | 6.222 | 0.138 |
| 6.5 | 0.483 | 6.740 | 0.128 |
| 7 | 0.448 | 7.259 | 0.119 |

#### 3.4.4.1.1 Proton 5T Cyclotron

The 5T proton cyclotron was first modeled for M²TF. The 5T Poisson design, Figure 3-10, was translated into *Acfields* and a yoke-coil model was created using Opera-3D. For a 5T central field cyclotron, the magnetic field at the point of extraction needs to be 5.18T, a total gain of 0.18T or

1800 Gauss over 17 cm due to the proton mass increase. The assumed model, without accounting for any contribution of the poles, had a 0.6T or 6000 Gauss increase in the magnetic field over 17 cm, Figure 3-16. It was obvious that the yoke's contribution to the magnetic field was too strong.

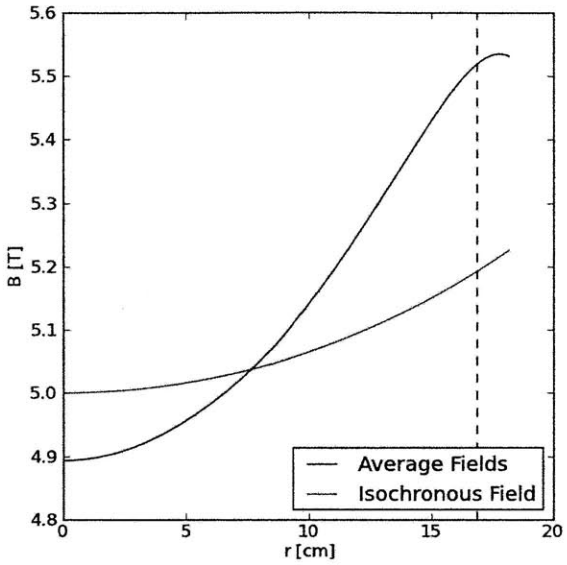


**Figure 3-16: Illustration showing the strong yoke field contribution (blue line) compared to the isochronous field (black line). The horizontal axis is radius in cm and the vertical axis is magnetic field in Tesla.**

To attempt to fix the problem of an overpowering yoke field:

1. A superconducting inner coil was added to increase the magnetic field in the first 5cm
    a. Applied to all revisions
2. The coil was moved further away from the center in the radial direction to reduce its contribution and hopefully lower the magnetic field at larger r
    a. Applied to rev29
3. The current supplied to the coils was reduced
    a. Applied to rev30

The result of these changes can be seen in Figure 3-17. The dark black line is the isochronous field attempting to be matched. 'Rev31' is a mix of changes 1 through 3.

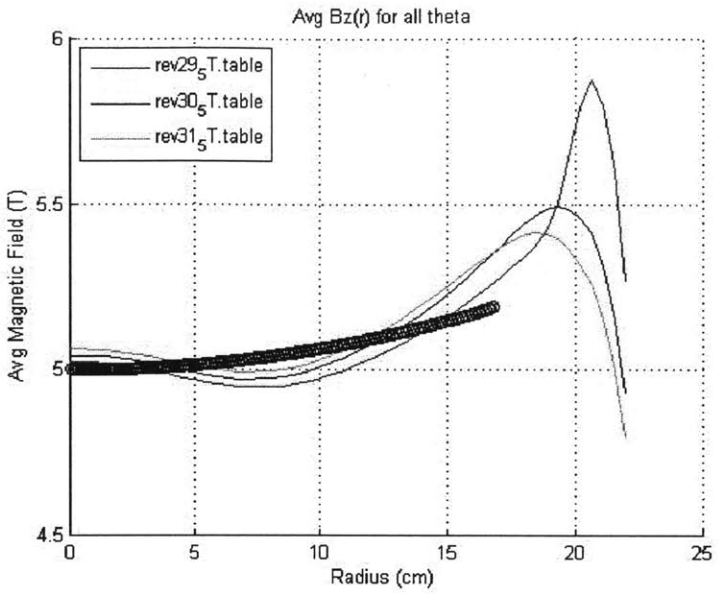


**Figure 3-17: Result the addition of steps 1-3. Each color represents the changes conducted to match the isochronous field (black line). Red: Coil movement, Blue: Current reduction, Green: Coil movement and current reduction. The horizontal axis is radius in cm and the vertical axis is magnetic field in Tesla.**

The changes proved that there is not a simple way to match the magnetic field with the isochronous field because the yoke's contribution is too large. Before the design was abandoned, analytical modeling was done to see if the design would still be possible despite the miss-matching of the isochronous field. Both sector and spiral designs were attempted Figure 3-18a and Figure 3-19a, recall a spiral design will generate better results for $v_z$ (Equation 3.23). Both designs still were not able to generate enough flutter (Figure 3-18b and Figure 3-19b) to keep $v_z$ positive, as seen in Figure 3-18c and Figure 3-19c as the green line. Since $v_z$ was not positive, the proposed design was abandoned.

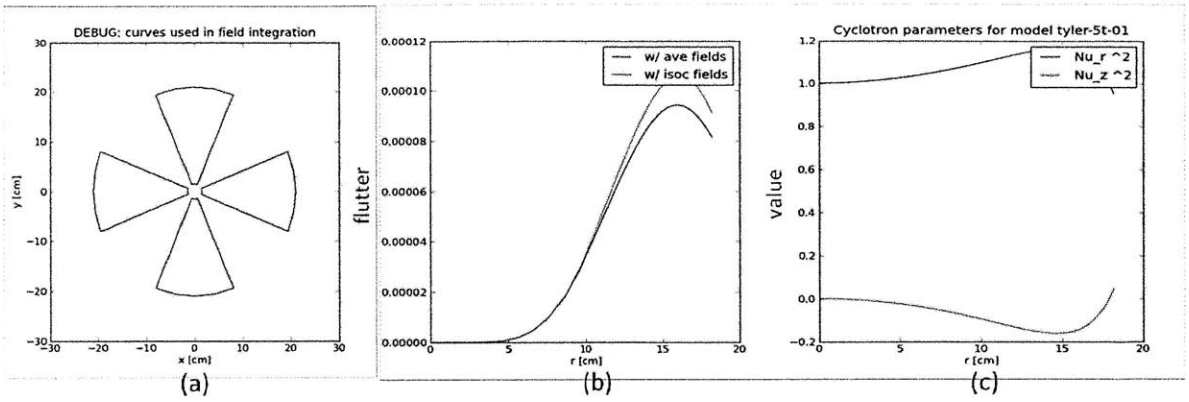


**Figure 3-18: Sector design (a), flutter (b), and representation of $\nu_z$ and $\nu_r$ (c) for the 5T Proton Cyclotron. Figure generated with *Acfields*.**

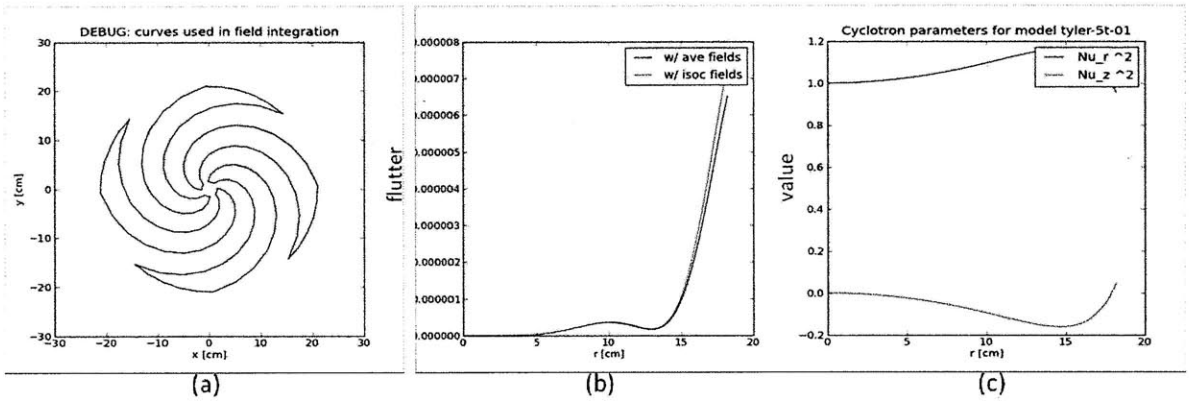


**Figure 3-19: Spiral design (a), flutter (b), and representation of $\nu_z$ and $\nu_r$ (c) for the 5T Proton Cyclotron. Figure generated with *Acfields*.**

#### 3.4.4.1.2 Proton 7T and 6T Cyclotron

The 5T design showed that the yoke's contribution must be less than the isochronous field gain until the radius of extraction. A 7T design was chosen for M²TF because it has a 0.25T increase in magnetic field at extraction (recall Table 3-6). The 7T design also has a steeper B vs. R slope because of its smaller extraction radius. Figure 3-20 illustrates both ideas for switching to the 7T design: higher B gradient resulting in a steeper slope.

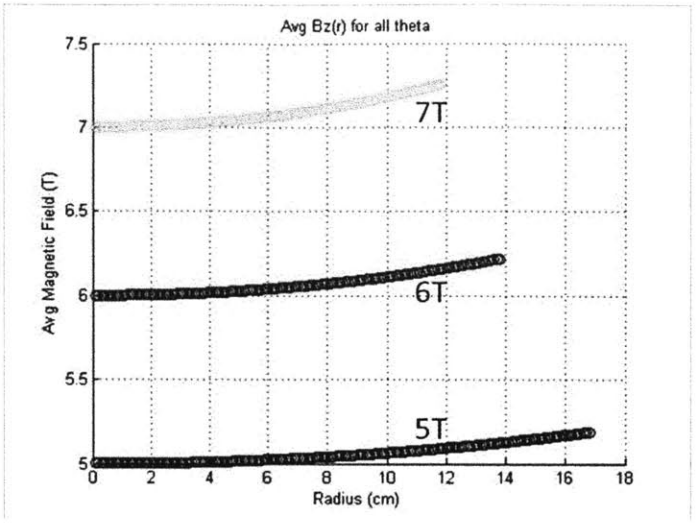


**Figure 3-20: Illustration of Delta B with respect to radius "r". B gradient increases with magnetic field. The horizontal axis is radius in cm and the vertical axis is magnetic field in Tesla.**

A zero sector model, or a yoke's contribution, was created in Opera-3D to see if the 7T design was possible. Figure 3-21 illustrates the yoke field (plotted in a red dashed line). Unlike the yoke field in the 5T design, the yoke field for the 7T machine is not as dominating and a good match of the isochronous field out to the ~11 cm extraction radius.

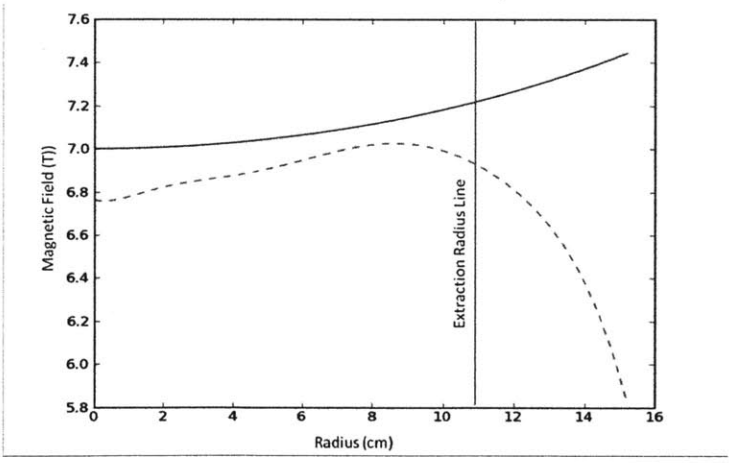


**Figure 3-21: Illustration of yoke field contribution for 7T Proton Cyclotron. The horizontal axis is radius in cm and the vertical axis is magnetic field in Tesla. Figure generated with *Acfields*.**

The 7T design was thought feasible based on the yoke's contribution. After repeated attempts to shape the sectors to match the isochronous field, the design was halted until the feasibility of other cyclotron properties were tested first. The current design was modeled with three holmium sectors, with a tight spiral, and a maximized pole and valley height difference. This situation

demonstrated the best condition for flutter and orbital stability, Figure 3-22. As seen in Figure 3-22, the design was not feasible due to insufficient values of $v_z$ resulting in loss of vertical stability during acceleration.

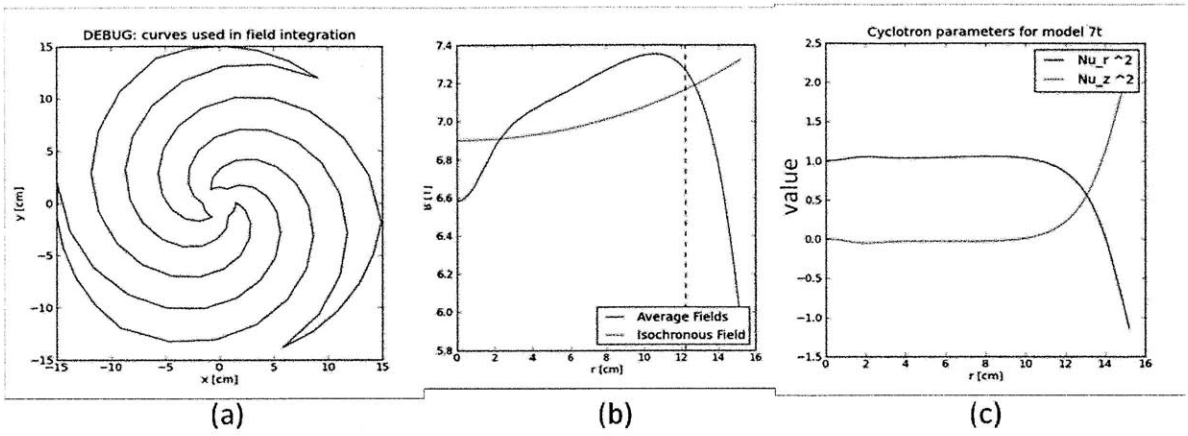


**Figure 3-22: Spiral design attempt (a), isochronous field (b) and value of $v_z$ and $v_r$ (c) for the 7T Proton Cyclotron. Figure generated with *Acfields*.**

With the 5T design having too high of a yoke's contribution, and the 7T design having to low of flutter, a 6T design was considered as a compromise. Much like the 7T design, the extreme conditions were modeled first to see if minimal flutter and orbital stability could be achieved, Figure 3-23. In the 6T design, both the yoke field contribution was too high and $v_z$ below zero. This result proved that something in the cyclotron design must be changed in order to make it feasible; this change would be found in the coil spacing and coil shape.

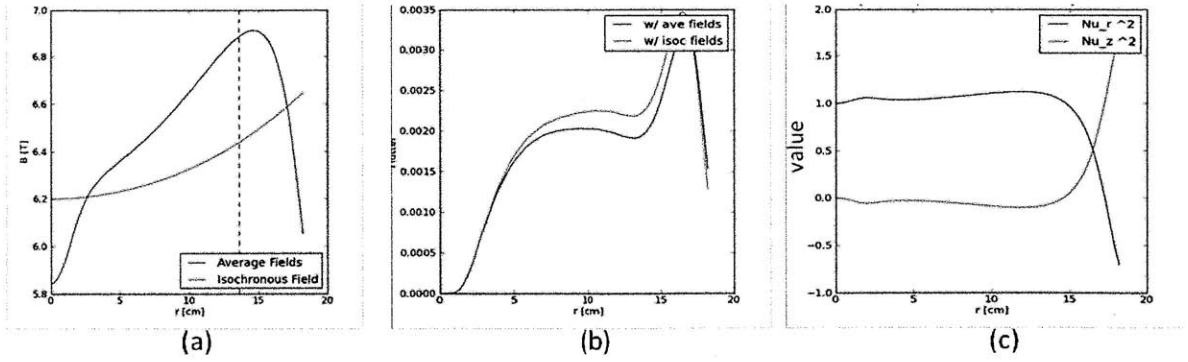


**Figure 3-23: Spiral design attempt (not shown) with isochronous field (a), flutter (b), and value of $v_z$ and $v_r$ (c) for the 6T Proton Cyclotron. Figure generated with *Acfields*.**

### 3.4.4.2 Coil Design

The idea of shaping and changing the spacing of the coil came from analyzing the Nanotron Cyclotron now under design at MIT [Antaya, 2010]. The Nanotron Cyclotron had a flat yoke field that was later shaped with iron/holmium poles. In order to generate a flat yoke field, the solenoids need to be far apart vertically and rectangular as opposed to square. An illustration of the coil spacing and shaping can be seen in Figure 3-24.

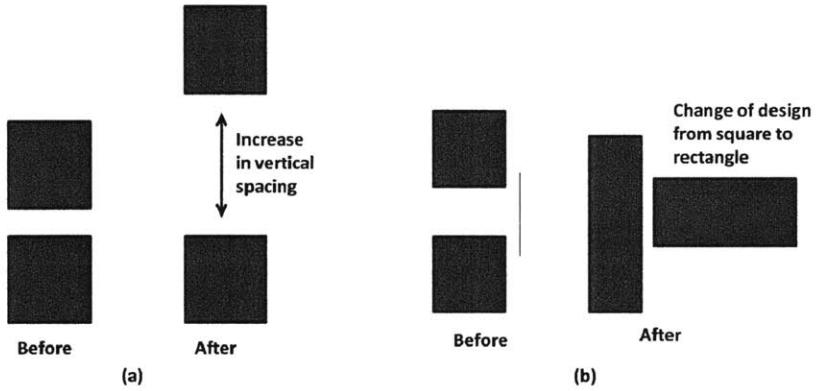


**Figure 3-24: Changes made to coil vertical spacing with respect to height (a) and coil shape (b) with respect to height and radius (width).**

A few examples are given below of the consequences of changing the size and configuration of the solenoid. An original yoke magnetic field contribution can be seen in Figure 3-25a. By increasing the coil vertical spacing by 2X, $\Delta B$ from the yoke field magnetic contribution would decrease as shown in Figure 3-25b.

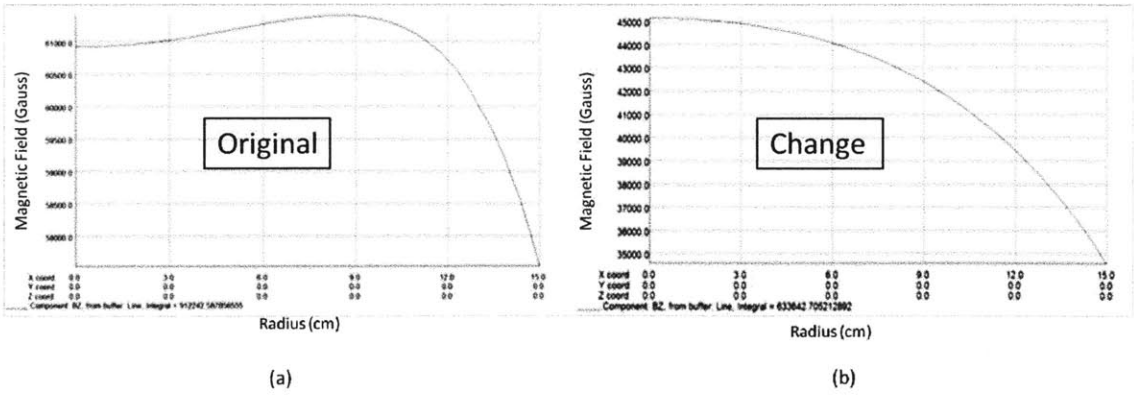


**Figure 3-25: An original isochronous field (a) changed due to increased coil spacing by a factor of 2 (b). The magnetic field decreases with respect to radius for increasing spacing. The horizontal axis is radius in cm and the vertical axis is magnetic field in Gauss (10,000G=1T).**

By design, the peak field should be at the extraction radius. This location helps guide particles to extraction because shortly after the particle loses stability when it encounters a decreasing B vs. R. An original yoke magnetic field contribution can be seen in Figure 3-26a. By changing the coil shape from square to rectangle, the peak of the yoke field can be moved depending on the location of the center of mass of the coil. However, increasing the location with radius of the peak magnetic field also increases $\Delta B$, Figure 3-26b. Changing the current density from 20,000 to 30,000 A/cm$^2$ creates a smaller coil for a given $B_0$ and further magnifies the effects of the peak's location and $\Delta B$.

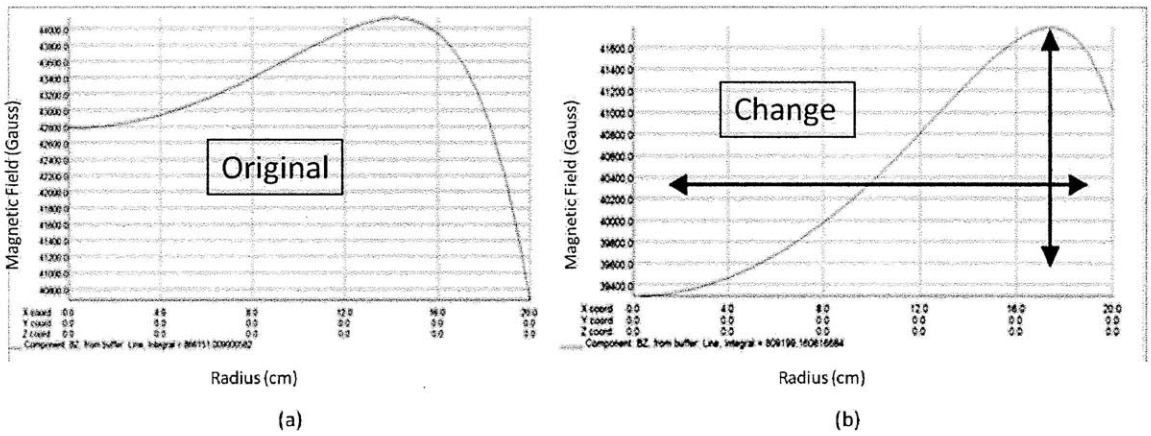


**Figure 3-26: An original isochronous field (a) changed due coil shaping of a rectangle of twice height and one width (b). Result is that both $\Delta B$ and radius have increased by 1500 G and 4 cm respectively. The horizontal axis is radius in cm and the vertical axis is magnetic field in Gauss (10,000G=1T).**

The different coil designs were taken into account to create a relatively flat yoke field with an extraction radius around 17-20 cm (5T to 4T). An optimized design consists of a cyclotron reaching full energy at more than 90% of the pole radius (radial efficiency). Radial efficiency is the ratio of the pole radius by the inner coil radius. High radial extraction efficiency is needed in order to utilize the given space of the cyclotron. Anything less than 90% would mean that most of the cyclotron is wasted space. After 30-40 revisions, an optimal design was created which is shown in Figure 3-27. Figure 3-27a shows the cyclotrons spiral design. Figure 3-27b illustrates that with pole shaping the isochronous field (green line) can be matched. Since the yoke field was generally flat, a majority of the field shaping was due to the poles. The more material in the poles allowed for high flutter and orbital stability (Figure 3-27c and Figure 3-27d).

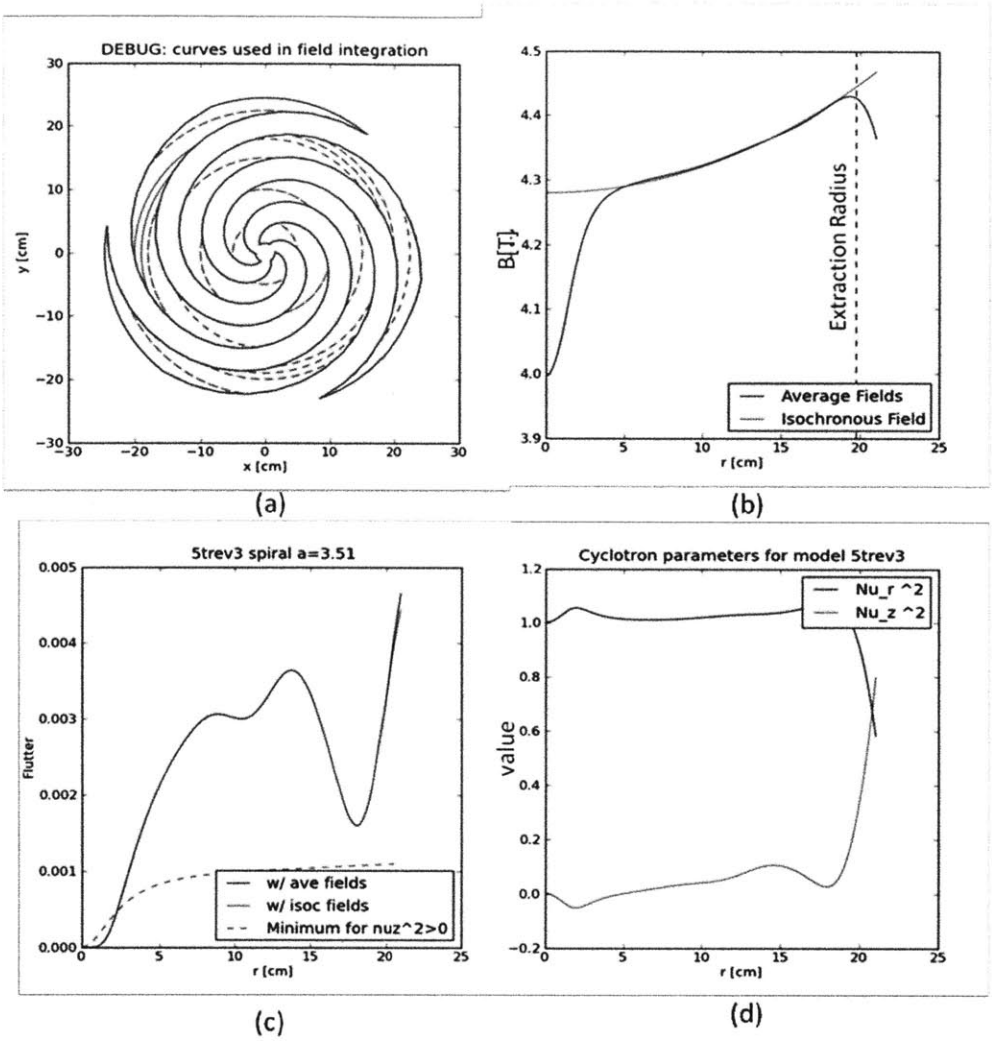


**Figure 3-27: Spiral pole Design (a), isochronous field (b), flutter calculations (c) and value of $v_z$ and $v_r$ (d) for the Proton 4.3T Cyclotron. The dotted red lines plotted in (a) signify the cuts on the poles. Figure generated with *Acfields*.**

*Acfields* was able to quickly generate an isochronous field with spiral pole shaping. The next step is to design the poles and yoke in SolidWorks and run the model in Opera 3D. Two models were created in SolidWorks, a radial pole sector and spiral pole (Figure 3-28a and Figure 3-28b respectively). Spiral models in Opera-3D take hours to compute compared to a sector model. Since the isochronous field remains the same no matter the design, a sector design was modeled. In this case, the Opera-3D results were similar to that of the *Acfields*. The isochronous field was relatively the same; the only difference was the magnitude of the magnetic field. Opera-3D computed the cyclotron $B_0$ as a 4.325T machine, whereas *Acfields* resulted in 4.28T, a 500 Gauss difference. A difference in magnetic field at extraction (500 gauss) is not unreasonable given the simplicity of

*Acfields*, but the final cyclotrons will have to use Opera 3D. This difference is of little concern and can be corrected with minor shimming [Antaya, 2010]. For clarity, this cyclotron will be referred to as the 4.3T Proton Cyclotron despite the correct central magnetic field value computed with Opera-3D.

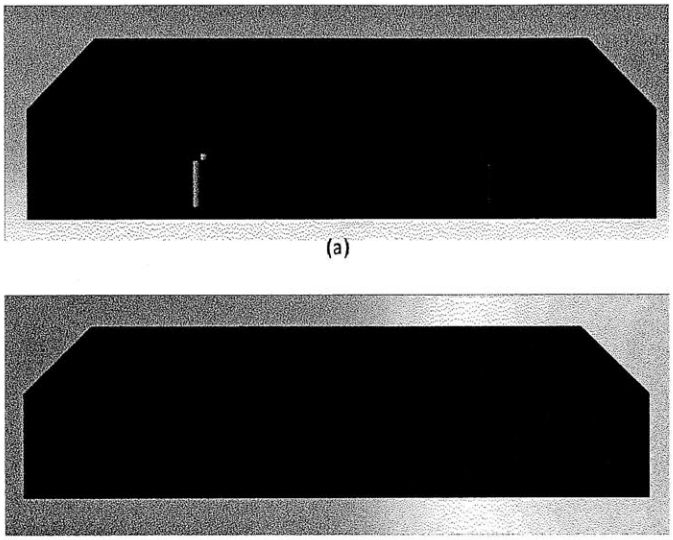

(a)

(b)

**Figure 3-28: SolidWorks design for the Proton 4.3T Cyclotron sector model (a) and spiral model (b).**

### 3.4.4.3 Design Limitations

#### 3.4.4.3.1 Proton 5.5T Cyclotron

To see if a more compact design could be created, a higher field model was attempted. Aiming for a 6T machine, a 5.5T machine was created. Although the design was smaller in size, minimum flutter and $\nu_z$ could only be achieved by using holmium. Figure 3-29a-d illustrates the design, isochronous field, flutter and $\nu_z$. Figure 3-29e is a zoom-in version of Figure 3-29d that shows the dip in $\nu_z$ in the center which will require later correction. Price and stability issues prevented this design. Two of the main goals in cyclotron selection were low cost and avoiding design limits, constraints, or issues. Holmium is a lanthanide series metal that costs 1500 $/kg or 681 $/lb, roughly 60 times more than the price of iron [Antaya, 2011]. This results in a machine that is almost three times more expensive than the 4.3T iron based design. This cyclotron design also has issues with negative $\nu_z$ values. Figure 3-29e illustrates that $\nu_z$ was not greater than 0.04 until a radius of 13 cm. The first 6-8 cm can be corrected by an inner coil, but accounting for the next 5 cm is very difficult and sometimes cannot be done due to restrictions in cyclotron space. This design, although

plausible, has zero practical gain over the 4.3T design- the smaller size is far outweighed by the fundamental difficulties.

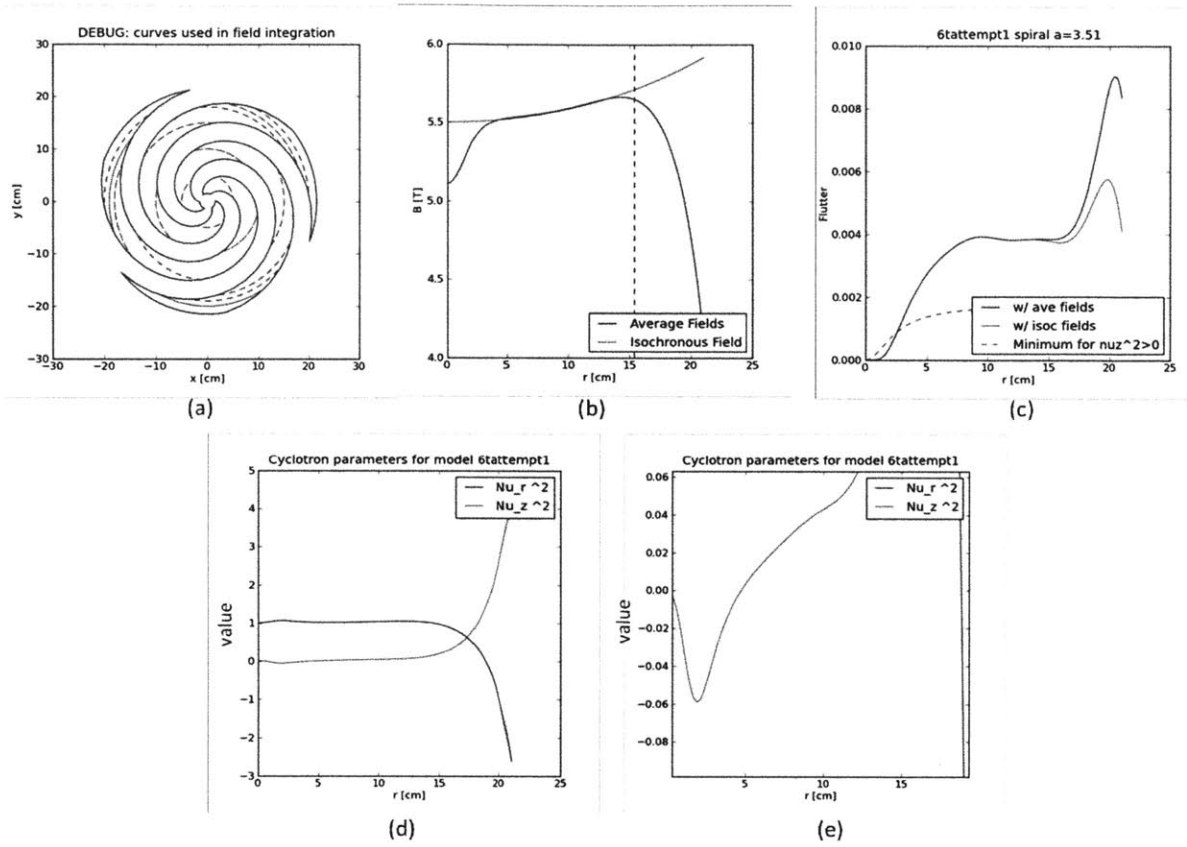


**Figure 3-29: Spiral pole design (a), isochronous field (b), flutter calculation (c), value of $v_z$ and $v_r$ (d) and zoom of value of $v_z$ (e) for the Proton 5.5T Cyclotron. The dotted red lines plotted in (a) signify the cuts on the poles. Figure generated with *Acfields*.**

A 6T design was also tested; its results were similar to that of the 5.5T design. Although the machine could generate enough flutter, $v_z$ never became positive indicating this machine was not feasible. Both attempts to increase the magnetic field from the 4.3T design have shown that there is a limit in cyclotron design between 4.3T and 5.5T. It has become apparent that there is no advantage of adapting a 5.5 or 6T machine due to size, price, and orbital stability.

#### 3.4.4.4 Inner Coil Design

One may notice that the isochronous field seen in Figure 3-27 is not matched in the first few centimeters. With a 1.5 cm hole in the center of the cyclotron for future ion source placement, the magnetic field is depressed in this region. The depression is corrected by adding either a central iron ring or a coil to boost the magnetic field at the center. This field 'bump' will raise the magnetic

field above the isochronous and will be necessary for radial stability when the particle is first introduced to the magnetic field [Antaya, 2010].

The iron ring's feasibility for creating such iron bump fields was tested first. A small iron ring, with dimensions listed in Table 3-7, was added to the center of the cyclotron. The result of adding a central ring can be seen in Figure 3-30. The red line represents the modified field and the blue line represents the existing field. The desired isochronous field was plotted in black as a reference in the figure. As seen in Figure 3-30, the magnetic field shifted and no longer matches the isochronous field, creating a tail from the iron contribution from radius 4 to 8 cm. Any addition of iron to the cyclotron will raise the magnetic field locally and disturb the magnetic flux in the overall region. It was concluded that an iron ring cannot be used to raise the central field.

**Table 3-7: Iron ring dimension for 4.3T Proton Cyclotron.**

| Inner Radius | Outer Radius | Height 1 | Height 2 |
|---|---|---|---|
| 0.5 cm | 1.5 cm | 1.5 cm | 8 cm |

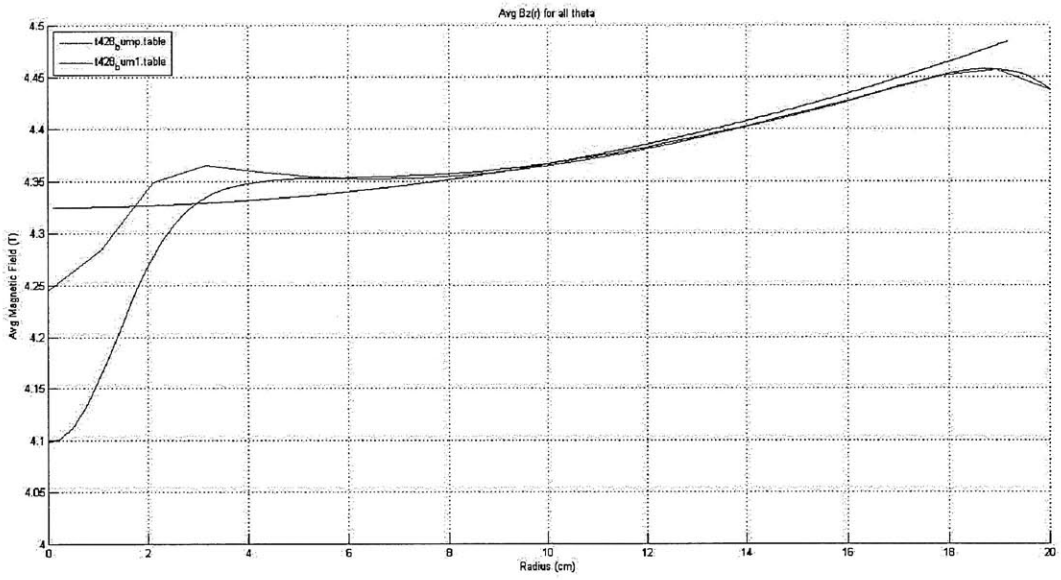


**Figure 3-30: Magnetic field coil bump contribution from a central iron ring with dimensions listed in Table 3-6.**

There are two routes to raise the central field without disturbing the flux in other locations: using a non-superconducting or superconducting coil. Non-superconducting coils have a maximum current density of 1000 A/cm$^2$ [Supercon Inc, 2011]. Since the strands that build a conductor are cylindrical and the coil is rectangular, there is a packing factor around 70% therefore reducing the maximum current density to 700 A/cm$^2$. To test if a non-superconducting coil would suffice in

providing a central field bump, one was inserted from inner radius 0.5 cm to 1.5 cm. This would allow the coil to fit inside the 1.5 cm radius hole with the ion source. The magnetic field contribution was computed with Poisson and can be seen in Figure 3-31. The y-axis is in units of Gauss, 10,000 G is 1 Tesla. A non-superconducting coil with the given dimensions can only provide 145 Gauss. The central field bump needed for the 4.3T machine is 2600 Gauss. It is apparent that a non-superconducting coil cannot be used for this purpose of providing a field 'bump.'

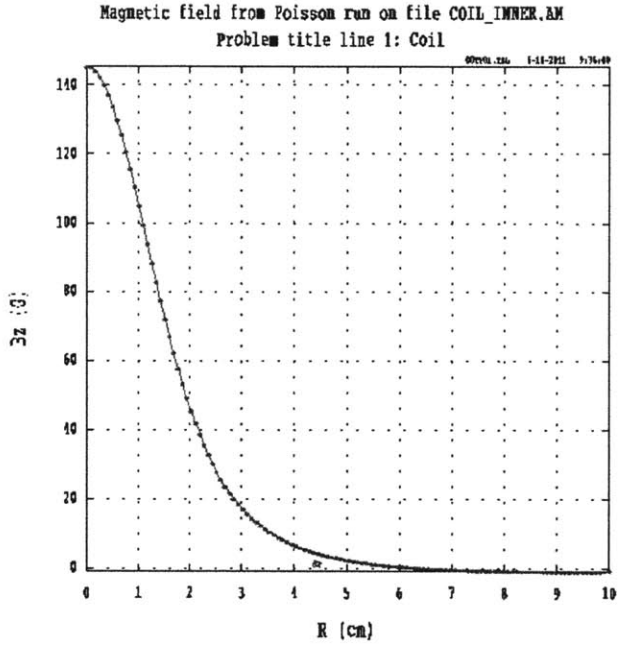


**Figure 3-31: Non-superconducting inner coil contribution reaching 145 Gauss for the Proton 4.3T Cyclotron. Figure generated with Poisson.**

The next step was to model a superconducting coil in Poisson to determine the number of amp-turns for cost and applicability. Complexity will increase due to the cooling of a superconducting wire, but there is no other option. The current density of 20,000 A/cm$^2$ was chosen. The inner coil radius was fixed at 0.5 cm. The outer radius and height 1 and height 2 were varied until the proper bump magnetic field contribution was achieved. Table 3-8 lists the final bump coil's dimensions. The result of the super-conducting coil can be seen in Figure 3-32. The coil was then super-imposed on the original 4.3T isochronous field, as shown in Figure 3-33.

**Table 3-8: Dimension of Superconducting inner coil.**

| Inner Radius | Outer Radius | Height 1 | Height 2 |
|---|---|---|---|
| 0.5 cm | 2.8 cm | 1.5 cm | 3.5 cm |

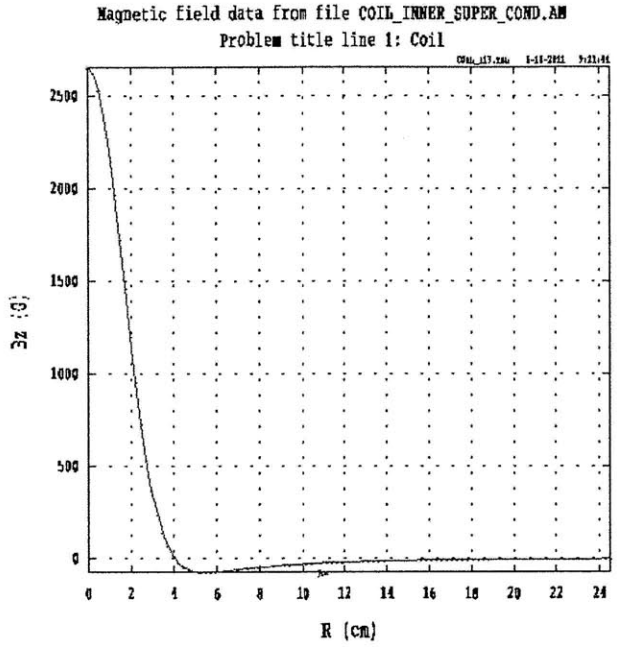


**Figure 3-32: Superconducting inner coil result reaching 2600 Gauss for the Proton 4.3T Cyclotron. Figure generated with Poisson.**

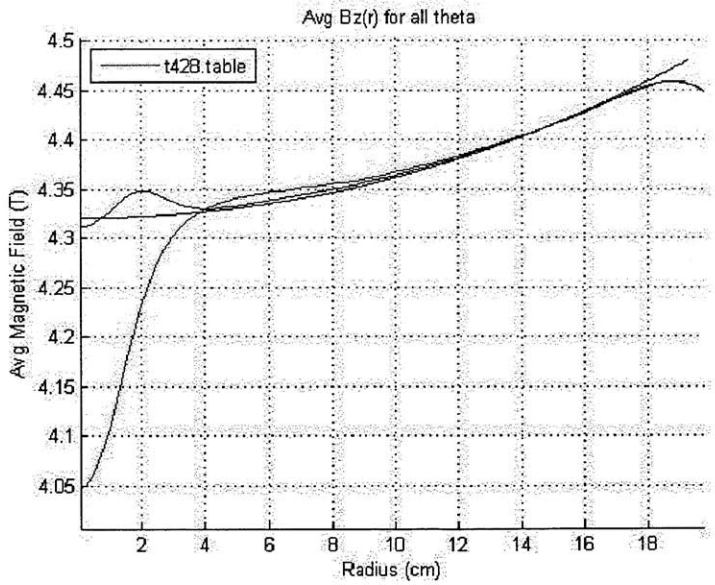


**Figure 3-33: Superconducting inner coil result (blue line) superimposed onto the Proton 4.3T cyclotron isochronous field (red line) with the isochronous field equation (black line).**

This bump coil cannot fit without interference with the poles. This exercise was only meant to determine the number of amp-turns needed for the coil and establish feasibility. In reality, the inner

pole radius will be adjusted to fit in the bump coil and then adjusted to correct what changes may have occurred to the isochronous field. Table 3-9 lists the geometric and electric properties of the superconducting coil for the 4.3T proton cyclotron. A 0.85 mm diameter wire can withstand 790A at 5T [Supercon Inc, 2011]. The maximum current per wire for the proposed inner coil is 35 A and will not exceed coil design or operation limits.

**Table 3-9: Number of Amp-turns for the inner coil of proton cyclotron.**

| Strand Diameter | Area of Strand | Area of Coil | Number of Wire Turns | Amps per Wire(Current of 20,000 A) |
|---|---|---|---|---|
| 0.85 mm | 0.005672 $cm^2$ | 4.6 $cm^2$ | ~ 567 | 35 A |

## 3.4.5 Helium Cyclotron

### 3.4.5.1 Design Progression

With the knowledge gained from the proton design pitfalls and successes, the helium cyclotron design was relatively simple. However, with the size increase of the helium cyclotron, cost became a key design constraint. The idea with the helium cyclotron was to start with low field, knowing that stability would not be a limiting factor, and then increase the magnetic field until either cost began to increase or stability became inefficient. Cost would decrease as magnetic field increased until holmium had to be introduced in place of iron poles to maintain flutter.

### 3.4.5.2 Design and Design Limitations

Table 3-10 provides selected extraction radius and final magnetic fields for a 3, 4, and 5T Helium Cyclotrons with a final energy of 100 MeV. This table will be referenced repeatedly in the following sections.

**Table 3-10: Selected tabulated values for Helium Cyclotron isochronous field.**

| $B_o$ (T) | $\alpha$ (m) | $B_{final}$ (T) | $R_{extraction}$ (m) |
|---|---|---|---|
| 3 | 1.038 | 3.078 | 0.466 |
| 3.5 | 0.890 | 3.591 | 0.399 |
| 4 | 0.779 | 4.105 | 0.349 |
| 4.5 | 0.692 | 4.618 | 0.311 |
| 5 | 0.623 | 5.131 | 0.279 |
| 5.5 | 0.566 | 5.644 | 0.254 |
| 6 | 0.519 | 6.157 | 0.233 |

The first design created was a ~3T Helium design (actual 3.2T). As seen in Table 3-10, it has a large extraction radius, twice that for a 6T machine. Coils where shaped and spaced to create a flat magnetic field yoke contribution. Since the machine is much larger than the proton, fewer issues of stability were encountered. Figure 3-34(a-e) show good orbital characteristics, with high flutter and positive $\nu_z$. Its only negative characteristic is its enormous size. In order to move the peak magnetic field toward the extraction radius the pole radius was increased to 75 cm. With the addition of the yoke thickness, the cyclotron was 2.4 m in diameter and weighed closed to 15 tons. With the amount of iron and the increase in conductor length, the estimated cost of the 3.2T Helium Cyclotron would be over 7 million dollars.

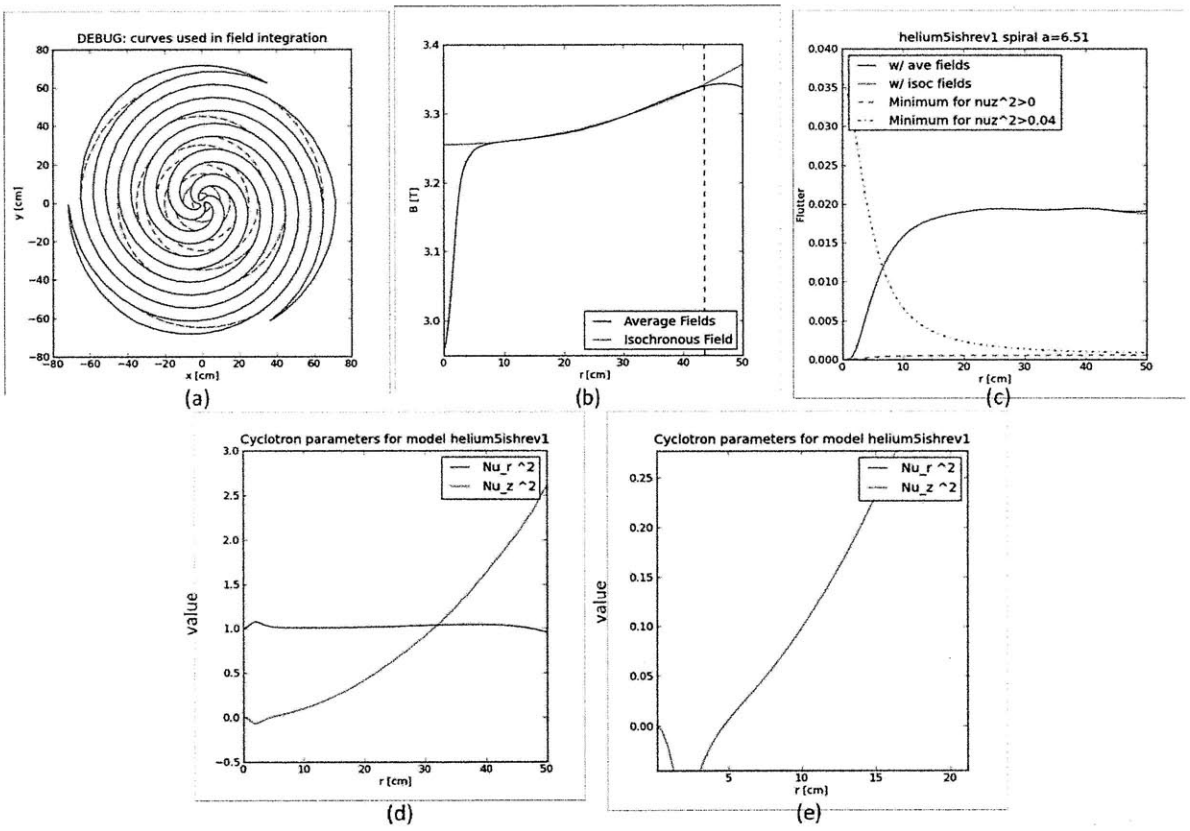


**Figure 3-34: Spiral pole design (a), isochronous field (b), flutter calculation (c), value of $\nu_z$ and $\nu_r$ (d) and zoom of value of $\nu_z$ (e) for the Helium 3.2T Cyclotron. The dotted red lines plotted in (a) signify the cuts on the poles. Figure generated with *Acfields*.**

The next design was one modeled toward a higher magnetic field to focus on reducing the cost of the machine. A 6T machine was originally chosen, but due to trouble in creating a flat magnetic field contribution from the yoke, a 5.4T design was settled on. Similar to the high field proton designs, the 5.4T Helium design could not generate enough flutter, see Figure 3-35. The increase in

flutter over the first 12 cm can be accomplished by using valley coils to boost flutter or by tightening the spiral. Although achievable, this machine would be difficult to build and it would be better to actually lower the field to boost flutter. The price, however, was six times less than the 3.2T design at approximately 2.5 million dollars.

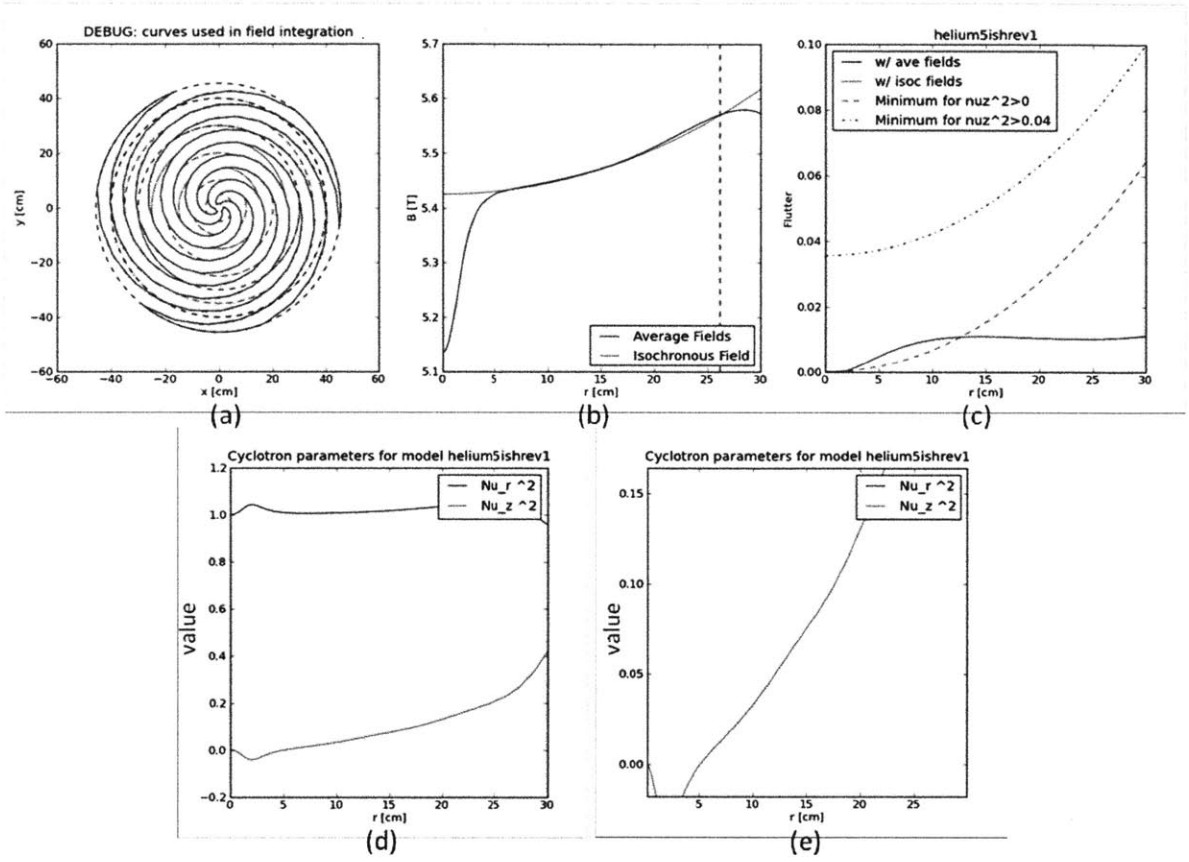


**Figure 3-35: Spiral pole design (a), isochronous field (b), flutter calculation (c), value of $\nu_z$ and $\nu_r$ (d) and zoom of value of $\nu_z$ (e) for the Helium 5.4T Cyclotron. The design does not meet minimum flutter requirements. The dotted red lines plotted in (a) signify the cuts on the poles. Figure generated with *Acfields*.**

The next design was aimed toward a 4T machine. A 4T machine should have enough flutter and stability and also be low in cost. The results of a 3.9T machine can be seen in Figure 3-36. Not only did the 3.9T machine contain good properties, it was also the same price as the 5.4T design. With proper coil spacing and shaping, the 3.9T design proved very efficient. A cross section of the pole design for both sector and spiral models can be seen in Figure 3-37a and Figure 3-37b respectively. *Acfields* was again benchmarked with Opera-3d and predicted a near exact isochronous field, a difference of only 200 Gauss.

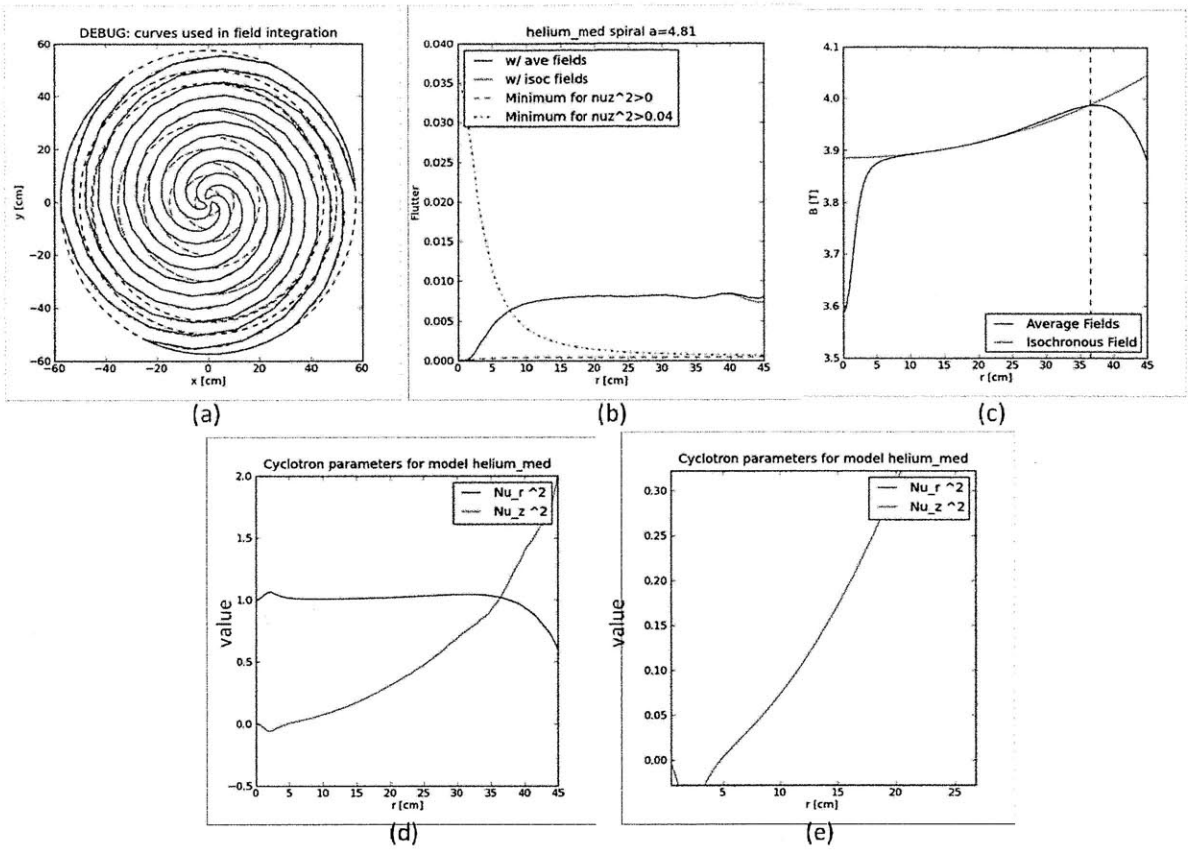


**Figure 3-36: Spiral pole design (a), isochronous field (b), flutter calculation (c), value of $\nu_z$ and $\nu_r$ (d) and zoom of value of $\nu_z$ (e) for the Helium 3.9T Cyclotron. The dotted red lines plotted in (a) signify the cuts on the poles. Figure generated with *Acfields*.**

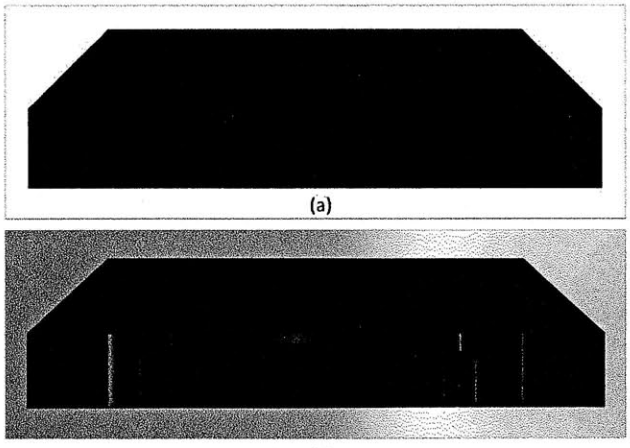


**Figure 3-37: Helium 3.9T Cyclotron cross-section view of SolidWorks design. Sector design (a) and spiral design (b).**

### 3.4.5.3 Inner Coil Design

Based on the results of the proton inner coil section, a superconducting coil must be used in order to achieve more than 145 Gauss in the 3.9T Helium cyclotron. Within a few attempts a superconducting coil was created with properties given in Table 3-11 and the resulting magnetic field contribution is shown in Figure 3-38.

**Table 3-11: Dimension of 3.9T Helium Cyclotron superconducting inner coil.**

| Inner Radius | Outer Radius | Height 1 | Height 2 |
|---|---|---|---|
| 0.5 cm | 3.5 cm | 1.5 cm | 5.5 cm |

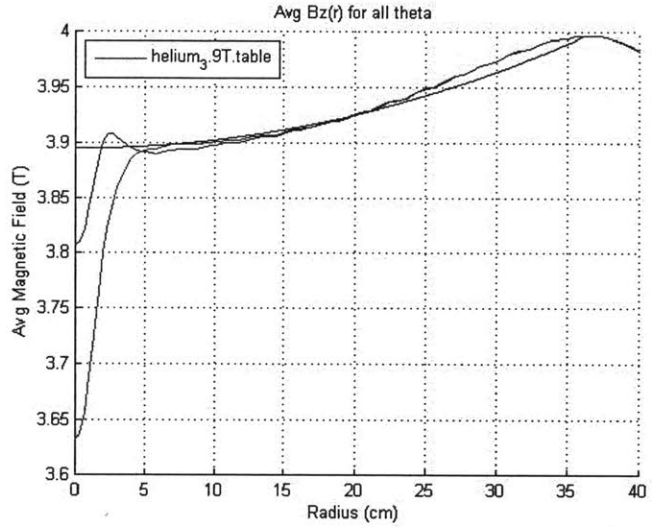


**Figure 3-38: Superconducting inner coil result (blue line) superimposed onto the Helium 3.9T Cyclotron isochronous field (red line) with the isochronous field equation (black line).**

Again this bump coil cannot fit without interference from the poles of the 3.9T Helium Cyclotron. Table 3-12 lists the geometric and electric properties of the superconducting bump coil. The maximum current per wire for the proposed inner coil is 11 A and will not exceed design or operation limits.

**Table 3-12: Number of Amp-turns for inner coil of Helium Cyclotron.**

| Strand Diameter | Area Of Strand | Area of Coil | Number of Wire Turns | Amps per Wire (Current of 15,000 A) |
|---|---|---|---|---|
| 0.85 mm | 0.005672 $cm^2$ | 12 $cm^2$ | ~ 1480 | 11 A |

## 3.5 Final Proposed Design

The final design for both cyclotrons was developed in the proceeding sections. Figure 3-39 and Figure 3-41 illustrate a 3D view of the overall proton and helium cyclotron design respectively. Figure 3-40 and Figure 3-42 show the sector pole design (a), spiral pole design (b) and coil (c). The purpose of the sector pole design is to better illustrate the pole shaping completed to match the isochronous field. A summary of their height, width and weight can be seen in Table 3-13.

**Table 3-13: Summary of Cyclotron Design.**

| Cyclotron | Height (cm) | Width (cm) | Rough Weight (lbs) |
|---|---|---|---|
| Proton | 46 | 84 | 3024 |
| Helium | 100 | 180 | 28,260 |

### 3.5.1 Proton Cyclotron

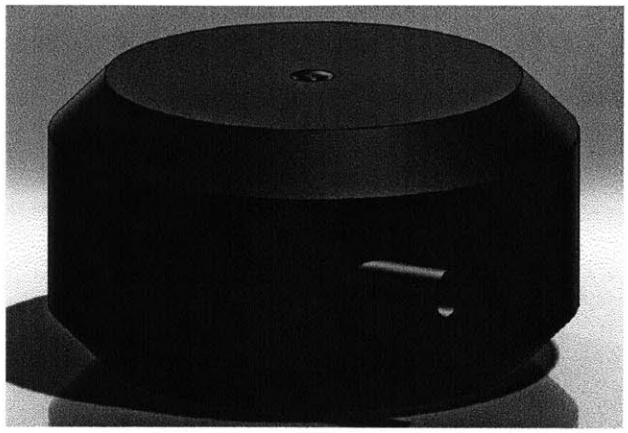

**Figure 3-39: Final Design of Proton 4.3T Cyclotron. The dimensions are diameter of 84 cm and total height of 46 cm.**

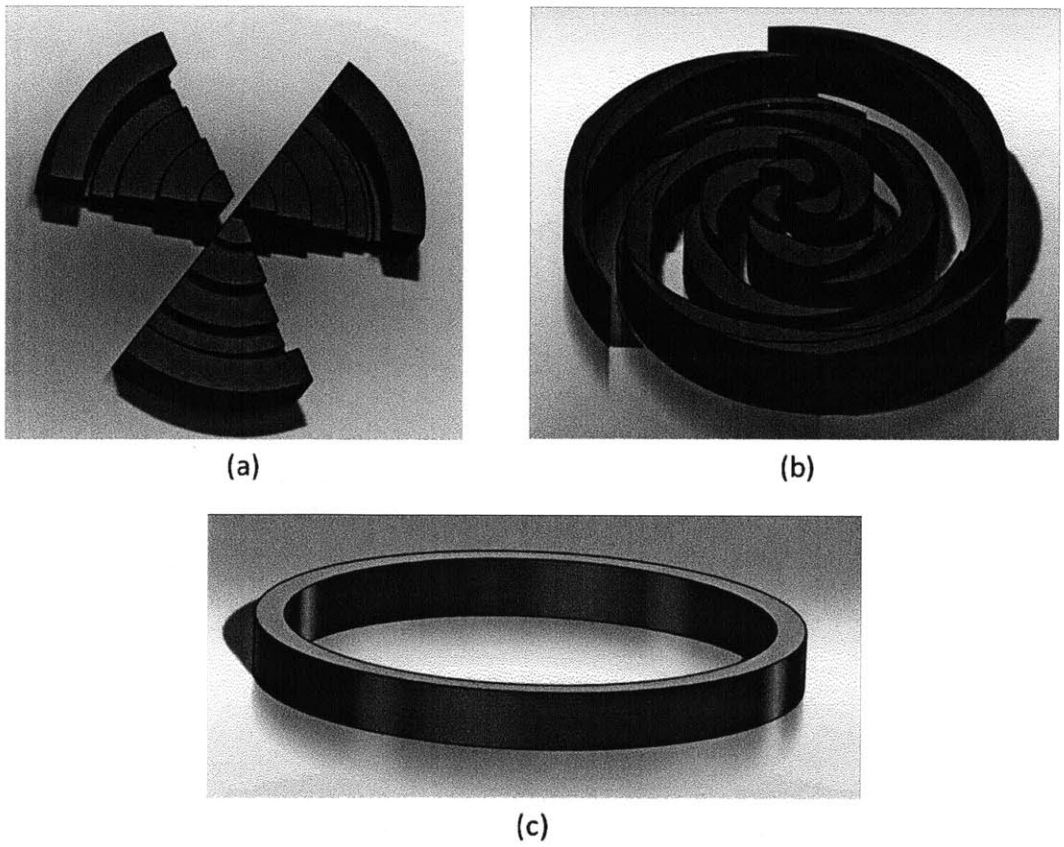

(a) (b)

(c)

**Figure 3-40: Final sector pole design (a), spiral pole design (b) and coil (c) of Proton 4.3T Cyclotron.**

Layout drawings of the overall design, coil, and pole sector/spirals can be seen in Appendix D.

### 3.5.2 Helium Cyclotron

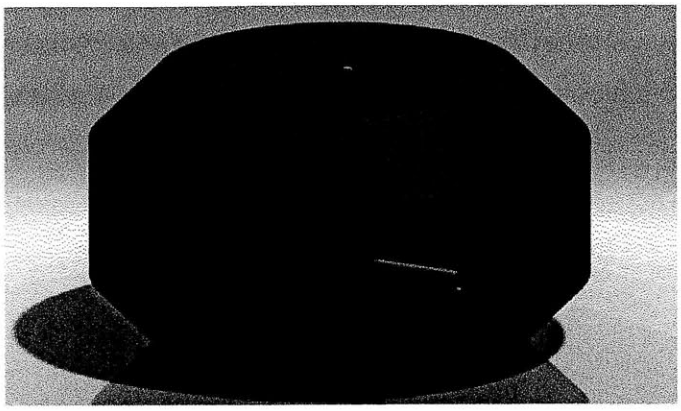

**Figure 3-41: Final Design of 3.9T Helium Cyclotron. The dimensions are diameter of 180 cm and total height of 100 cm.**

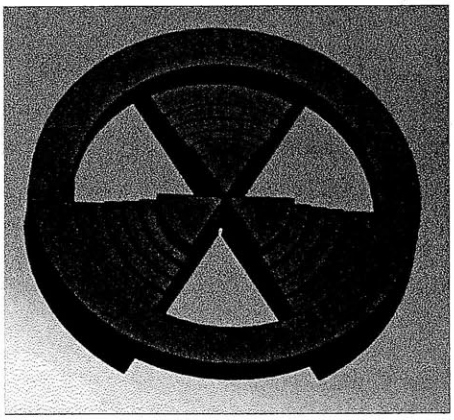

(a)

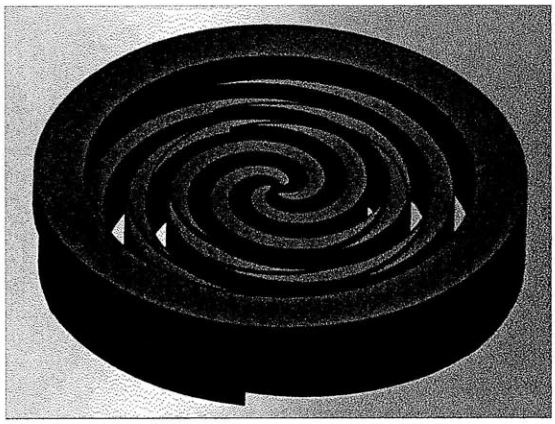

(b)

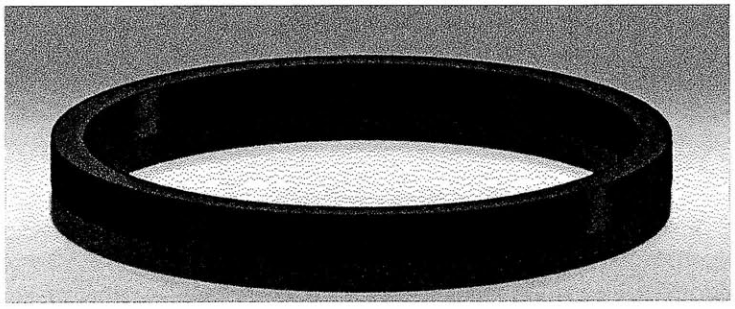

(c)

**Figure 3-42: Final sector pole design (a), spiral pole design (b) and coil (c) of Helium 3.9T Cyclotron.**

Layout drawings of the overall design, coil, and pole sector/spirals can be seen in Appendix D.

## 3.6 Cost Analysis

The detailed cost analysis for a cyclotron is very complex. In this section, a rough order of magnitude (ROM) cost is presented. Using experience, the ROM cost has been simplified to be driven by 4 main elements: the cost of iron, the cost of the coil, the cost of the cryostat and the cost of the magnet. These elements are the key cost drivers, which when combined allow for the cost approximation for the cyclotron.

### 3.6.1 Cost of Iron

The historical cost of 10$/lb for machined magnet iron will be assumed [Antaya, 2011]. To determine an accurate mass, a simple 2D magnetic model, using symmetry and geometry, can be easily transferred from Poisson to a 3D CAD program, in this case SolidWorks. Material properties were assigned to the model and the mass of iron was determined. Most CAD programs offer thousands of compositions of iron alloys; depending on the selection, the mass will vary slightly. Regardless, the differences should have little effect when determining a rough estimate of the price of iron. The cost of iron in both cyclotrons can be seen in Table 3-14.

**Table 3-14: Cost of manufactured iron.**

| Cyclotron | Mass of Iron (lbs) | *Cost |
|---|---|---|
| P4.30T | 3024 | $30240 |
| H3.9T | 28,260 | $282,600 |

*Machined Iron Price ~ 10$/lb

### 3.6.2 Conductor/Coil Cost

Since the peak fields in the conductors are less than 9T, Niobium Titanium (NbTi) superconducting wire is chosen to generate the magnetic field [Antaya, 2011]. NbTi can achieve current densities up to 3,000 A/mm$^2$ without significant challenge; exceeding that of copper by two orders of magnitude [Bruker, 2011]. If the peak field was greater than 9T, Niobium Tin ($Nb_3Sn$) would have been used. $Nb_3Sn$ wires are known for their higher performance under high magnetic fields, especially those seen in fusion environments. NbTi wires used for conductors have the following approximated properties:

- Price ~300 dollars/kg

- Packing fraction of 70% inside rectangular coils
- Diameter of 1 mm
- $\rho \approx \rho_{Cu} = 8.92 \frac{g}{cm^3}$

The above properties were used to determine the cost of the conductor. The coil consists of hundreds of wound strands of NbTi laid on top of each other. The area of each strand, $A_{Strand}$, is:

$$A_{Strand} = \frac{\pi}{4} D^2 \tag{3.29}$$

Since the coil area is rectangular and the strands are cylindrical, there will be packing efficiency ($P_f$) we take conservatively as 70%. Applying the packing efficiency creates an effective area of the coil, $A_{coil}$:

$$A_{coil}=A_{Conductor}*Pf \tag{3.30}$$

To find the total number of circular loops, N, the $A_{coil}$ is divided by the $A_{Strand}$:

$$N = \frac{A_{coil}}{A_{Strand}} \tag{3.31}$$

The average radius, $R_{avg}$, was taken at the center of the coil and determined the average circumference, $C_{avg}$:

$$C_{avg} = 2\pi r_{avg} \tag{3.32}$$

Multiplying the circumference by the total number of loops determined the total length, $L_{tot}$, of NbTi needed to produce the coil:

$$L_{tot} = N * C_{avg} \tag{3.33}$$

A more exact solution of the total length can be completed with by accounting for turn separation and climbs. This analysis, however, is only an approximation. Using the area of a strand of NbTi and its density, $\rho$, the mass can be determined. With a mass of NbTi in kilograms the cost is calculated:

$$V_{coil} = A_{Strand} * L_{tot} \tag{3.34}$$

$$Mass = \rho * V_{coil} \tag{3.35}$$

$$Cost = 300\frac{\$}{kg} * Mass_{(kg)} \tag{3.36}$$

A table of the approximate values is listed in Table 3-15 for both cyclotrons.

**Table 3-15: Conductor cost.**

| Machine | $*A_{Strand}$ ($cm^2$) | $A_{Conductor}$ ($cm^2$) | $A_{coil}$ ($cm^2$) | N | $r_{avg}$ (cm) | $C_{avg}$ (cm) | $L_{total}$ (cm) | $V_{coil}$ ($cm^3$) | Mass (Kg) | Cost ($) per shell |
|---|---|---|---|---|---|---|---|---|---|---|
| P4.30T | 0.00785 | 18 | 12.61 | 1606 | 26.5 | 166.42 | 267,120 | 2096.89 | 18.70 | 5611.28 |
| H3.9T | 0.00785 | 33.75 | 23.64 | 3010 | 61.4 | 385.43 | 1,159,988 | 9105.90 | 81.22 | 24,367.39 |

*1 mm Diameter Wire Used

* Prices were computed for half the cyclotron

## 3.6.3 Overall Engineering Cost

The price of the iron and conductor were carried over to Table 3-16. Each coil price was doubled to account for the use of two coils in each cyclotron. Based on recent cyclotron cost analyses, the price of the superconducting magnet cryostat is roughly ten times the price of the conductor, and the cost of the magnet is roughly the cost of the cryostat and iron together [Antaya, Cost Estimate of Cyclotron, 2011]. The total cost of the cyclotron includes that price of iron, magnet, and the coils. This accounts for the one-third the cost of the whole cyclotron. The two-thirds not included is the one-third labor cost and one-third cyclotron components cost (ion sources, RF amplifier, vacuum, cooling, etc). A rough estimate of total cyclotron price would then be three times (3X) the price of the cyclotron raw materials [Antaya, 2011]. An estimated total cost for each cyclotron can be seen in Table 3-16.

**Table 3-16: Overall engineering cost for each cyclotron.**

| | Iron Cost | Conductor Cost | SC cryostat Cost | Magnet Cost | Estimated Cyclotron Cost (3X) |
|---|---|---|---|---|---|
| P4.30T | $30,240 | $11,222 | $112,220 | $142,460 | $427,380 |
| H3.9T | $282,600 | $48,734 | $487,340 | $769,940 | $2,309,820 |

*All prices rounded to the nearest dollar

# 4 Facility Design

The purpose of a shielding calculation is to identify the radiation hazards associated with the operation of each cyclotron and the target chamber, in order to develop a facility that will succeed in all safety standards and codes for total effective dose rate.

## 4.1 Shielding Concern

Accelerated charged particles, except synchrotron radiation effects, do not produce radiation unless they interact with matter. Radiation caused from bremsstrahlung and synchrotron radiations are negligible at energies below the GeV range and are insignificant to the radiation created from the interaction with matter [Cossairt, 2007]. For M²TF, these sources of radiation will be ignored. Most of the radiation caused from cyclotrons is due to beam extraction losses and particles losses in orbit. Even with extraction efficiencies of 99%, a significant amount of particles can escape to the surrounding areas and contribute to significant biological dose rates. Since there will always be inefficiencies in the acceleration of particles, significant shielding must be provided for safety.

Shielding low energy beams (less than 10 MeV) is especially complex because it is the region of significant nuclear effects. The Radiation Physics for Personnel and Environmental Protection Fermilab Report TM-1834 states "there are many resonances associated with the compound nucleus that can be excited and there are also many nuclear reaction channels leading to a large number of nuclear excited states up to 20 MeV in excitation energy" [Cossairt, 2007]. Energies below 200 MeV have a significant effect on human tissue. Below 200 MeV the proton range in tissue is less than the typical thickness of the human body [Cossairt, 2007]. Protons, while inside the body, can make thousands of collisions with neighboring cells before losing their energy [Lamarsh, 2001]. Secondary and tertiary reactions created from the material in the cyclotron create new particles well outside the defined cyclotron source. Although particles such as deuterium and alphas have little penetration power, they increase the production of photons and neutrons. Photons produced from (n,γ) and similar reactions can penetrate through meters of concrete, contributing to the total dose rate. The described situations above are only a few of many health concerns with radiation.

For the M²TF (energies of 36 to 100 MeV) it is important that a shield be sufficiently thick to distribute the energy of the particles and contain a sufficient amount of hydrogen to scatter all particles that reach the surface [Cossairt, 2007]. The most utilized material for shielding is high density concrete because it is a hydrogenous mixture of materials. The addition of lead and steel can be used for the reduction of the photon's contribution to the total effective dose rate. Since the M²TF is a new design, concrete thicknesses of 1 m were chosen to match with other shielding calculations from the Texas A&M K500 Cyclotron [Youngblood & Bronson, 1994] and Milan Cyclotron [Ferrari, Fasso, & Birattari, 1988].

## 4.2 Proposed Location and Layout

The corner rooms in NW21 are being used as the reference location for design purposes, see Figure 4-1. The rooms consist of two floors separated by steel grating with the upper floor having a ceiling height over 12 m. The room's surrounding walls and entry ways are already properly shielded with 1 m thick concrete doors (with labyrinth entry design) and exterior walls. The proposed M²TF shielding layout to fit in any corner room can be seen in Figure 4-2. The 12x12 m design was chosen for its symmetry. Each cyclotron space is modeled as a 4.5 m cube, with 1 m thick surrounding walls. Symmetry allows shielding results to be universal to all sides of the chamber. The target chamber is a 4.5x9 m rectangle with 1 m thick surrounding wall. The steel grating separating the two floors will be removed and replaced with a concrete, detachable roof. With the use of accepted construction dimensions and symmetry, calculation time, overall construction cost, and facility engineering will be reduced.

The proposed design is unique in that it is separated into chambers. Separate chambers allow for maintenance on one of the cyclotrons while the other is in operation. Ongoing maintenance without stopping an experiment will increase the reliability of the facility. Due to the size of each room, the proton chamber will have roughly 1.75 m of open space surrounding the cyclotron and the helium chamber will have around 1 m. The target chamber will be the most spacious. The extra space can be used for hot cell storage or other miscellaneous testing equipment and instruments. If space is a concern the target chamber can be reduced in size.

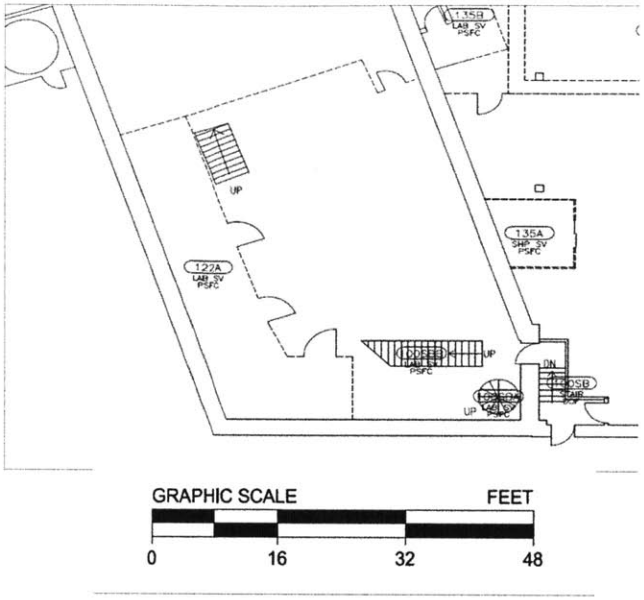


**Figure 4-1: Corner room in MIT building NW21 with scale in feet. The second floor is not shown in figure above. Figure adapted from MIT floor plans [MIT].**

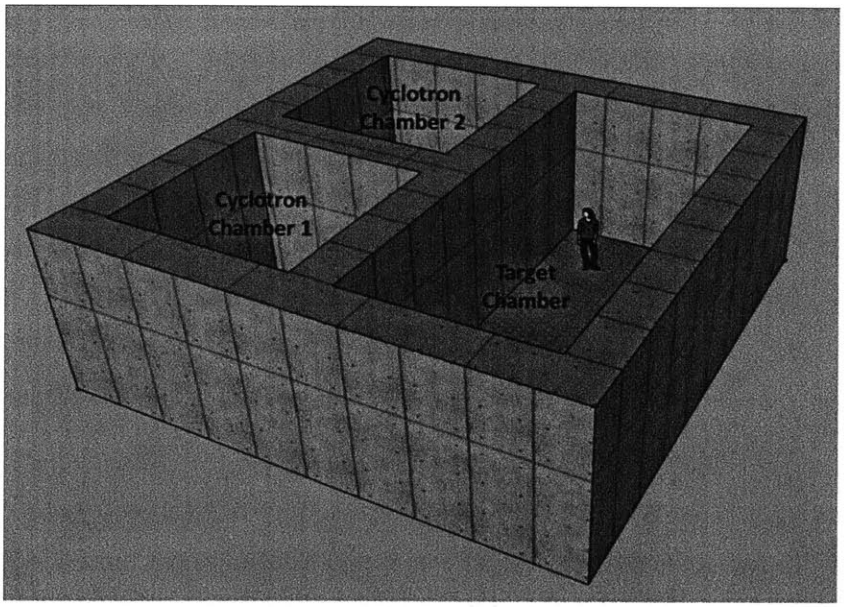


**Figure 4-2: MCNPX facility layout consisting of three chambers (two cyclotrons and target chamber) and concrete shielding walls. Roof not shown for visual purposes.**

## 4.3 The MCNPX Program

Monte Carlo N-Particle (MCNP) is a general purpose code used for neutron, photon, and electron transport and interaction with matter. MCNPX is an extension from MCNP that includes the ability to track all charged particles. MCNPX's applications include the design of accelerator spallation targets, investigations for accelerator isotope production, design of shielding in accelerator facilities, and activation of accelerator components [MCNPX, 2008].The units for MCNPX are length in cm, energy in MeV, density in $g/cm^3$, cross sections in barns, temperature in MeV (kt), and time in shakes ($10^{-8}$s). Since both cyclotrons are charged particle accelerators, MCNPX was used for $M^2TF$ shielding analysis. More information on MCNPX inputs, codes, functions, and assumptions can be seen in Appendix D.

### 4.3.1 Design Modeling and Representation

Figure 4-3 illustrates the cyclotron modeled in MCNPX. The table attached to Figure 4-3 provides a key to the meaning of the components. Overall size dimensions of the cyclotron were conserved with the original CAD model (refer to section 3.4.1 and 3.4.2). Only minor changes were made to the coils and the surrounding air gaps. From the original CAD model, the coils were instead expanded another 0.25 cm until they were flush with the pole sectors and yoke (the surrounding air gap was eliminated). The lines between the labeled parts of the cyclotron are drawn by VisEd to distinguish different cells. The cyclotron consists of many cells since it couldn't have been modeled in one piece with MCNP. The separation of these cells has zero effect on the result as long as the density and material specification cards are uniform. Before running the code, MCNPX merged surfaces and lines that are shared, releasing a warning identifying which surfaces where deleted.

To better represent the situation that is being modeled for each cyclotron in MCNPX, VisEd's particle simulation was used. Within VisEd, a disc source of isotropic 100 MeV helium particles was introduced at the center of the cyclotron, space 5 in Figure 4-3. Only a few thousand particles were tracked due to computational restrictions of the program. Every particle's (helium, protons, neutrons, photons, deuterons, and tritium) collision location and energy at the time of collision were plotted as a point in Figure 4-4. The simulation also included all (#,#) reactions, where new particles were introduced in the model that did not originated from the disc source or originating particles in MCNPX. The points plotted in Figure 4-4 have no distinction among the particles. The color of each point signifies their energy where red is high energy and blue low energy.

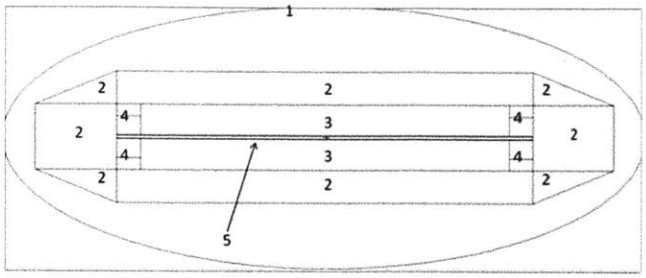


| Number | Meaning |
|---|---|
| 1 | Surrounding Tally Sphere |
| 2 | Iron Yoke |
| 3 | Iron Pole |
| 4 | Super-Conducting Coil, Air Gap, and Al Defector Plate |
| 5 | Beam Space with Copper Conductor Lining |

**Figure 4-3: MCNPX cyclotron model. Figure generated in MCNPX VisEd.**

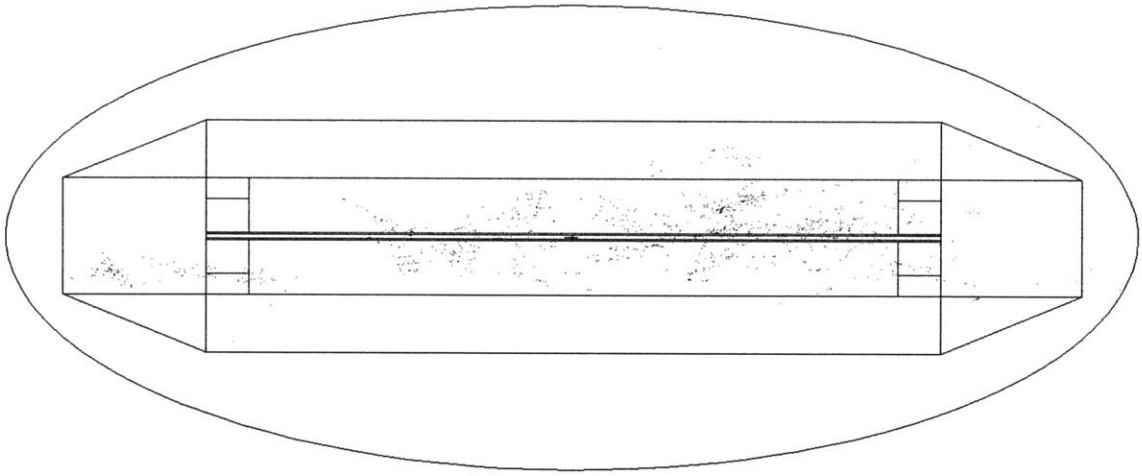

**Figure 4-4: Particle simulation of isotropic 100 MeV Helium disc beam source. Each dot represents the location of a collision, the color represents it energy at the time of collision.**

Each cyclotron was then inserted into their respective chambers with 1 m thick surrounding concrete walls. Figure 4-5 illustrates the idea. As seen in the figure, the cyclotron is placed inside its concrete chamber. What is not shown in the figure is the ion source, the surrounding tally sphere and surface flux tally.

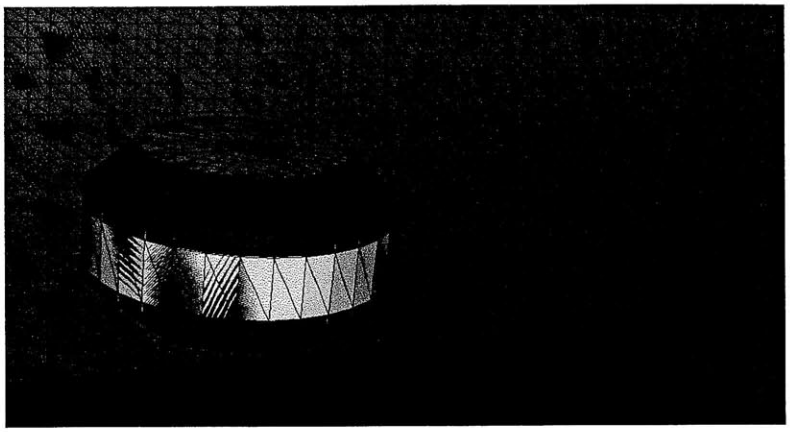

**Figure 4-5: MCNP 3D model of a cyclotron in its chamber. Figure generated with MCNPX VisEd.**

The target chamber modeled in MCNPX was a simple design consisting of a 2.75 inch thick stainless steel shell, roughly 1.5x1.5x3 ft comprising the pressure vessel. The 1.5x1.5 ft edge was fitted with a titanium window of thickness 100 $\mu m$ that allows the beams to pass to the target. The inside of the target chamber was pressurized with 10 MPa of helium. The target sample chosen for this analysis was a 1 mm thick slab of pure iron. Different materials could have been selected for the analysis; iron was chosen for this analysis because of the abundance of relevant cross section data. The target chamber modeled in MCNPX can be seen in Figure 4-6a. The model is extremely simplified compared to the proposed design, Figure 4-6b. It does not include the helium jet impingement cooling nozzles and equipment for the in-situ testing. There are a few reasons for such differences in design. The first is that the proposed target chamber (Figure 4-6b) is only a scaled design, with no real dimensions. The proposed design is also very design intensive, consisting of cones, jets, and other shapes that are difficult to model in MCNPX. The approach instead was to take a generic model of the target chamber and conserve the amount and type of material used in both. Although an approximation, the change in design should accurately represent results within a small factor since many components can be neglected as being too small or too thin to affect the results. This idea was adapted from Milan's cyclotron shielding calculations; it simplified many of the components of the cryostat in the cyclotron [Ferrari, Fasso, & Birattari, 1988].

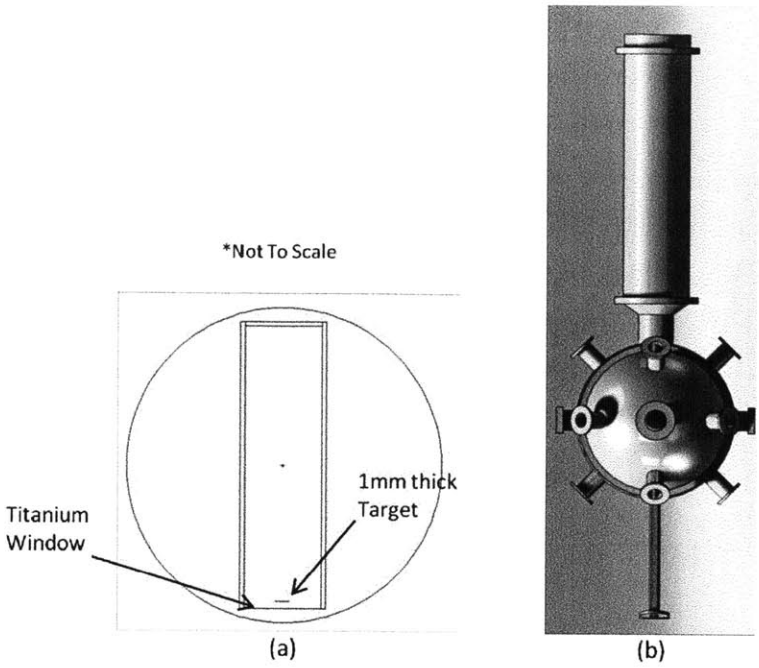


**Figure 4-6: Target chamber MCNPX model (a) and proposed design (b).**

### 4.3.2 Design Process

The first MCNPX non-programming issue arose when trying to model the whole facility. One cyclotron was chosen to operate while the other was stagnant. A point detector tally was placed in the stagnant chamber and programmed to calculate dose rate in rem/hr from both neutrons and photons. This comprehensive method failed because of large amounts of variance in the point detector tally. The large variance was due to the low number of particles reaching the point detector tally in the stagnant chamber. The first response was to increase the number of particles; however, this increased computation time to well over one week per run. This situation forced the shielding calculations to be broken up into sections and further modified to include variance reduction techniques.

In the next design, the point tally was replaced with a surface tally on the inner wall of the cyclotron. A surface tally would tally more particles than a point detector because of its size difference (4.5x4.5 m surface), increasing the number of particles hitting the wall. The spectrum captured by the surface tally would then be used to generate a new source at that location. This new source would be used in a separate model of just the source, concrete, and point detector. The issue when using surface tallies is the energy bin structure. When a particle travels through the surface

tally, its energy is recorded into bins; more particles per bin decrease the variance. As seen in Table 4-1, 1 MeV bin sizes were too large for low energy protons (number in bin was large) but too small for higher energies (number in bin was low). In order to reduce the variance, bin sizes were expanded for higher energy. This solved the variance issue, but created another problem. The particles most important to shielding are those with high energy; however, they were binned all together. With this bin structure, it is unknown whether the 25-36 MeV bin consists of a majority of 25 MeV particles or 36 MeV particles. Another method rather than expanding bin sizes is to increase the number of particles. Increasing the number of particles increased computation time to days.

**Table 4-1: Bin size example table with percent error. The percent error increases with larger bin size.**

| Energy (MeV) | # in Bin Normalized to number of particle histories | % Error |
|---|---|---|
| 1 | 1.04E-02 | 0.15% |
| 2 | 1.37E-04 | 0.90% |
| 3 | 2.65E-05 | 1.98% |
| 4 | 9.26E-06 | 3.25% |
| 5 | 5.17E-06 | 4.34% |
| 6 | 3.17E-06 | 5.44% |
| 7 | 1.89E-06 | 6.86% |
| 8 | 1.45E-06 | 7.80% |
| 9 | 1.19E-06 | 8.55% |
| 10 | 9.04E-07 | 9.85% |
| 11 | 9.04E-07 | 9.84% |
| 12 | 6.71E-07 | 11.09% |
| 13 | 6.50E-07 | 11.55% |
| 14 | 4.08E-07 | 14.58% |
| 15 | 2.71E-07 | 17.79% |
| 16 | 4.16E-07 | 14.66% |
| 17 | 3.46E-07 | 16.28% |
| 18 | 2.94E-07 | 17.71% |
| 19 | 3.99E-07 | 15.29% |
| 20 | 2.56E-07 | 19.29% |
| 21 | 2.10E-07 | 21.82% |
| 22 | 1.90E-07 | 22.94% |
| 23 | 1.10E-07 | 30.15% |
| 24 | 1.39E-07 | 26.73% |
| 25 | 1.00E-07 | 31.62% |
| 36 | 1.90E-07 | 22.94% |

The final design method was slightly different than the previous. It involved using a surface flux tally (F2) on each side of the concrete shielding walls. With a flux-to-dose conversion program, the dose rate in rem/hr was calculated. In order to reduce calculation time, the design included variance reduction techniques of geometry splitting, energy cutoffs, and Russian roulette. To

improve tally counting, it was assumed that 100% of the beam was lost to materials in the cyclotron. This was corrected after the fact by assuming a more realistic 95% extraction efficiency and scaling the results by a simple scalar. This method, along with variance reduction techniques, achieved reliable results with less than 10-20% error.

## 4.4 MCNPX Shielding Results

A spectrum for each chamber alone was first generated to indentify the number of particles and range of energy from secondary reactions occurring in each chamber. Along with the spectrum calculation the equivalent dose rate was calculated to illustrate the importance of shielding. The shielding results were determined from the proton chamber, helium chamber, and target chamber (both separately and in combination with each other). A source strength of 6.25E14 n/s (100% inefficient 0.1mA beam) was used for the target chamber. The source strength was reduced to 3.125E13 n/s to account for the 95% extraction efficiency of the cyclotrons.

### 4.4.1 Neutron and Photon Spectrum

The first calculation completed with MCNPX was to understand the spectrum of photons and neutrons from each cyclotron. A display of the energy range, for both neutrons and photons, was needed to make a better estimate on proper shielding techniques. The spectrum was captured by using a surface tally. The tally only recorded photons and neutrons. Other secondary particles that were present such as alpha, protons, deuterium, and tritium were insignificant compared to the magnitude of photon and neutron particles. Recording these miscellaneous particles could have easily been done. However, significantly more computation time would have been required. Note that while these particles were not recorded, they still were tracked in the MCNPX program (refer to section 4.3.1). Figure 4-7, Figure 4-8, Figure 4-9, Figure 4-10, and Figure 4-11 illustrate the spectrum of both neutrons and photons from the proton and helium cyclotron and target chamber which consist of three graphs, one for each circumstance. For each figure, the y-axis signifies the number of particles normalized to the starting number of histories and the x-axis signifies the energy bin size (between each major tick is the specified energy bin). A bar of zero height indicates that zero particles were found in this energy bin.

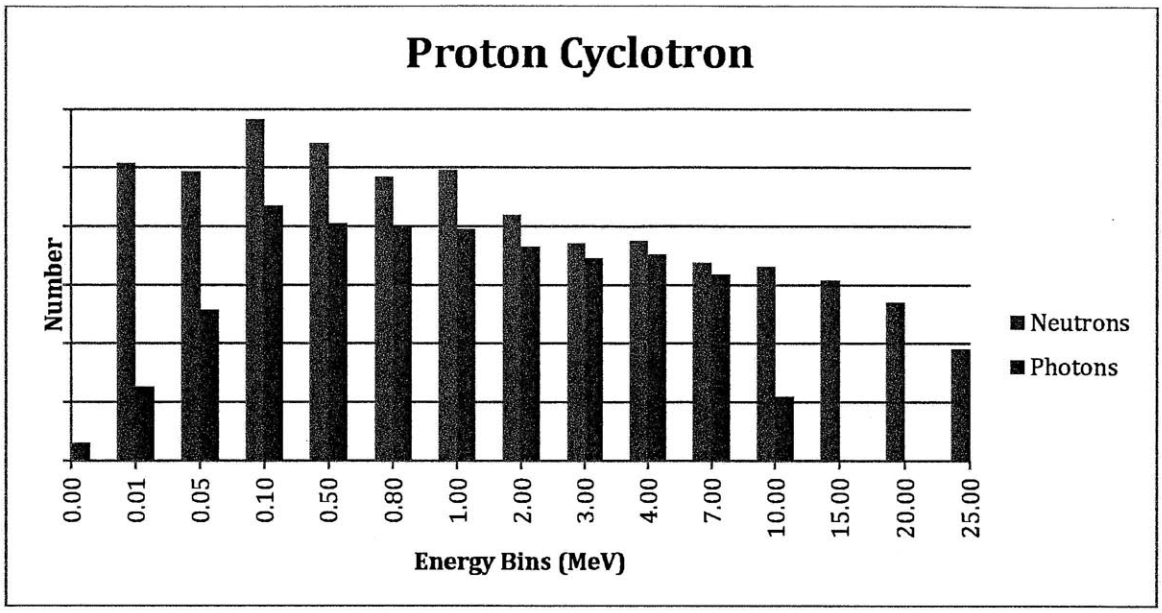


**Figure 4-7: Proton cyclotron spectrum.**

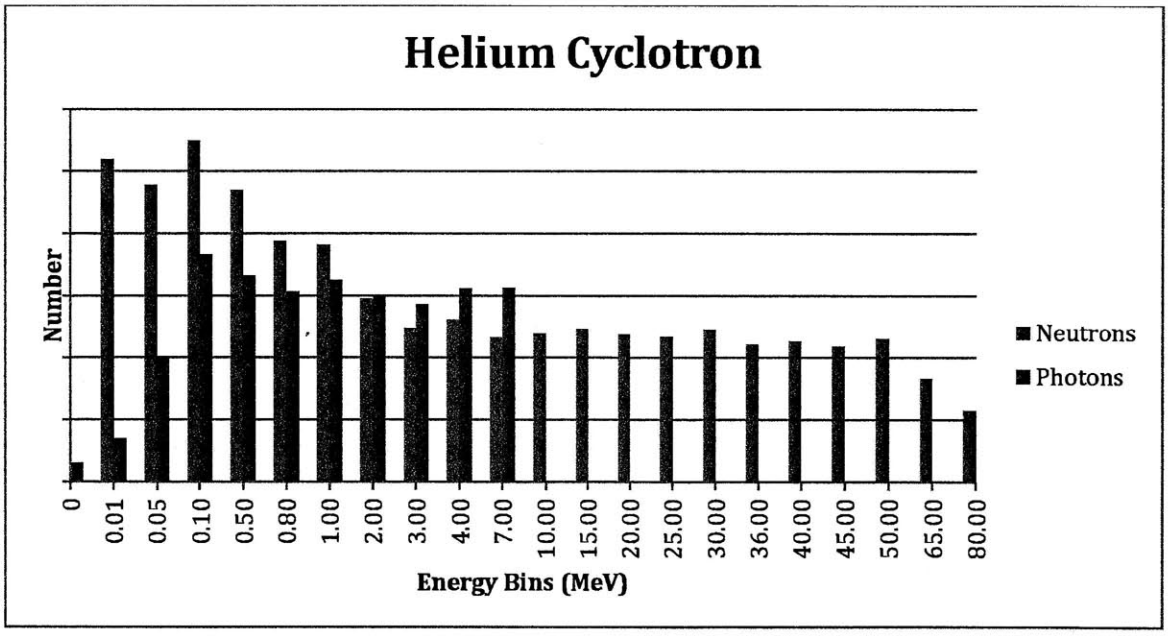


**Figure 4-8: Helium cyclotron spectrum.**

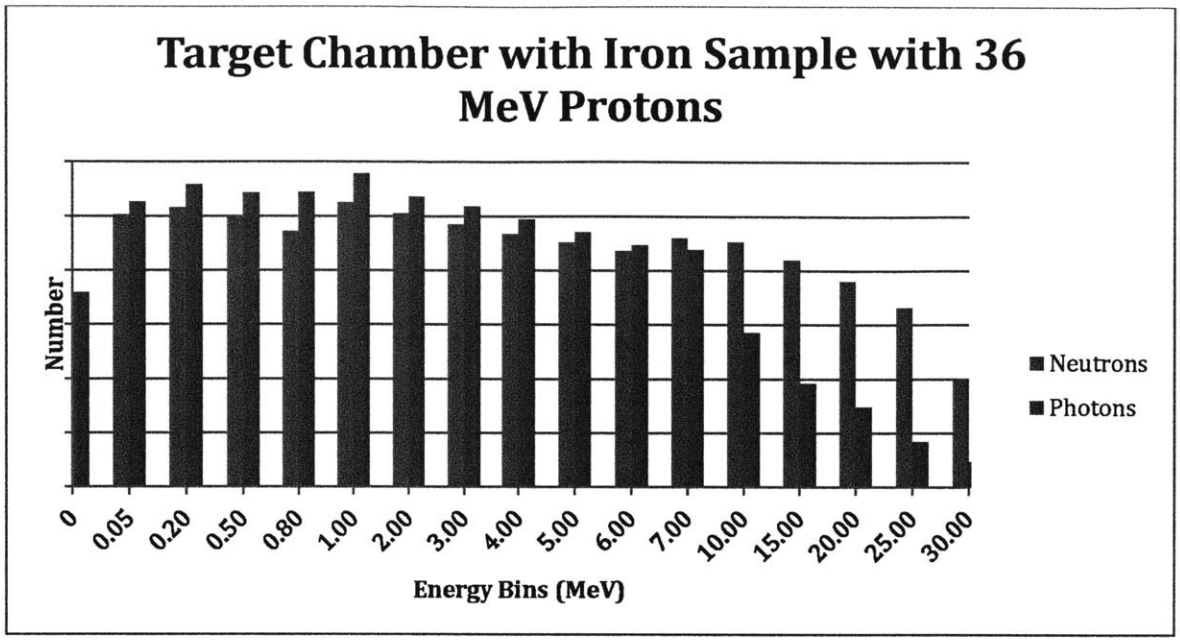


**Figure 4-9: Target chamber spectrum with 36 MeV protons on an iron sample.**

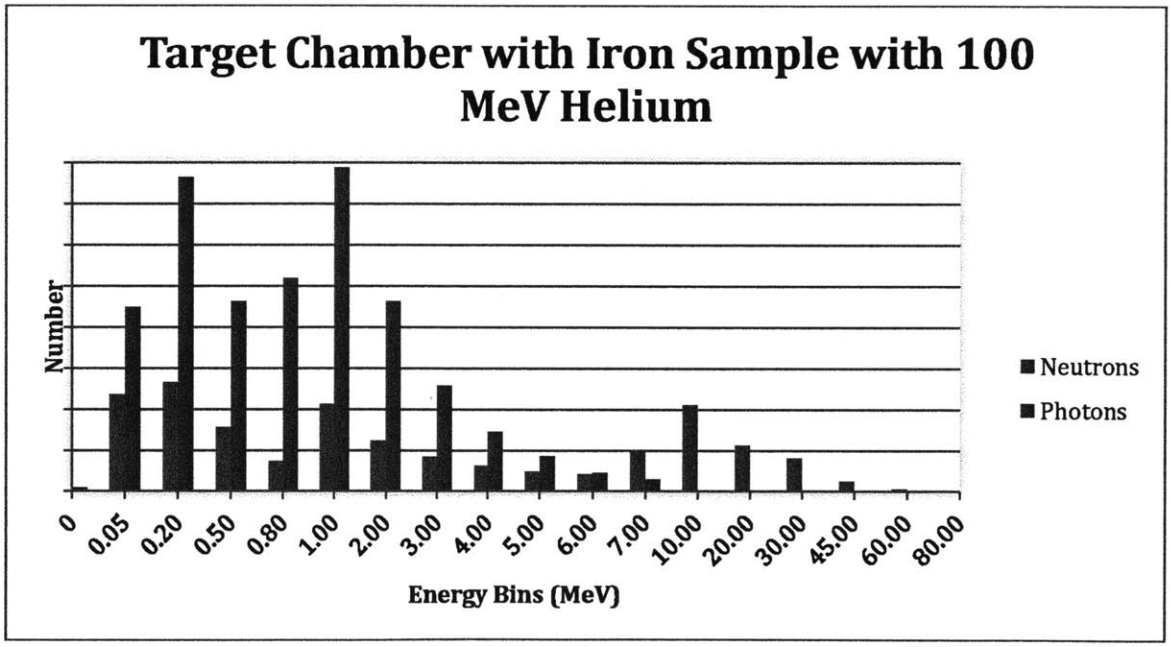


**Figure 4-10: Target chamber spectrum with 100 MeV helium on an iron sample.**

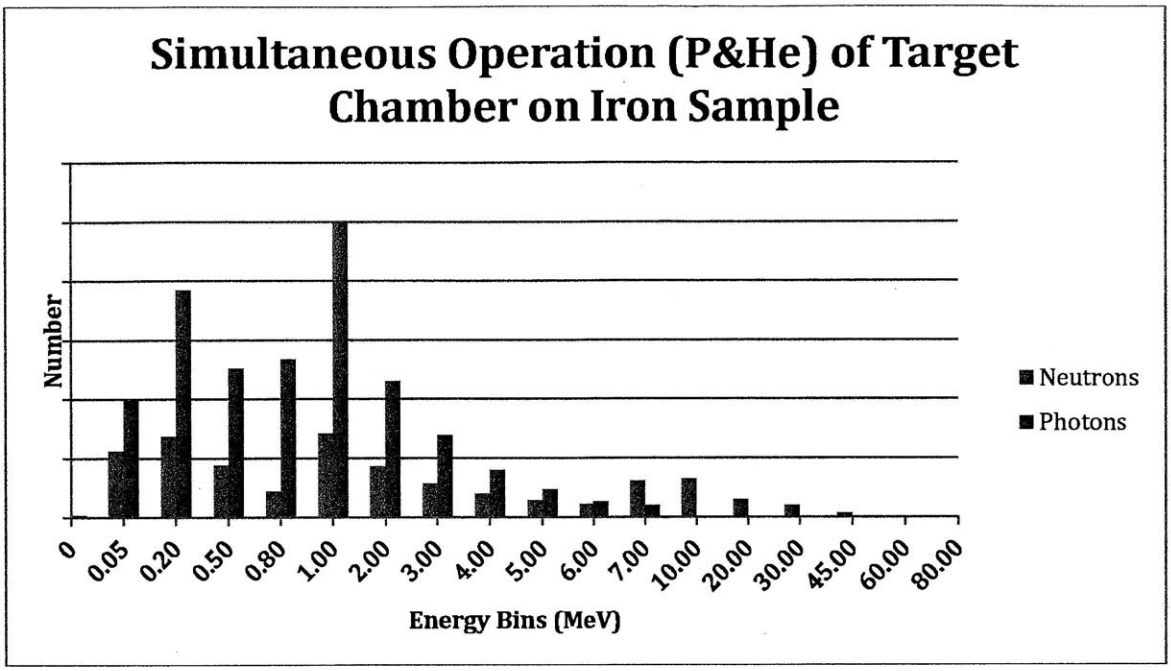


**Figure 4-11: Target chamber spectrum during simultaneous operation of both beams on an iron sample.**

### 4.4.2 Dose Rate Inside the Chamber

While in operation, the dose rate inside each chamber was calculated assuming the entire beam was lost for the target chamber and a 95% extraction efficiency to the cyclotron chambers. The results illustrate the importance of shielding the intense dose rate. Table 4-2 and Table 4-3 show the calculated dose rate inside a respective chamber. The table does not include any contributions of the other chambers. For example, the dose rate for the proton chamber while the helium and target chamber are in operation cannot be calculated from this table. Each table is broken down into each particle source contribution. The dose rate was computed with a flux-to-dose surface flux tally.

**Table 4-2: Dose rate inside cyclotron chambers with 95% extraction efficiency.**

| Cyclotron | Neutron Contribution (rem/hr) | Photon Contribution (rem/hr) | Total Contribution (rem/hr) |
|---|---|---|---|
| Proton | 35.02 ± 0.14 | 1.47 ± 0.01 | 36.49 ± 0.14 |
| Helium | 10.79 ± 0.07 | 0.70 ± 0.01 | 11.49 ± 0.07 |

Table 4-3: Dose rate inside target chamber with full beam stop.

| Beam | Neutron Contribution (rem/hr) | Photon Contribution (rem/hr) | Total Contribution (rem/hr) |
|---|---|---|---|
| Proton | 317.18 ± 0.95 | 14.44 ± 0.0549 | 331.62 ± 0.95 |
| Helium | 383.25 ± 3.83 | 16.10 ± 0.16 | 399.35 ± 3.84 |

### 4.4.3 Dose Rate Outside the Chamber

The dose rates outside of the shielding wall were then calculated for both respective cyclotron chambers with a 95% extraction efficiency and target chamber with full beam stopping. The results are shown in Table 4-4and Table 4-5. The tables only list data from its respective chamber in operation, not any combination. For example, the dose rate from the proton cyclotron is interpreted as if one was in the helium chamber, on the roof, outside, or in the target chamber while the proton cyclotron was in operation. Since the dose rate was calculated for 1 m thick walls for a cube for the cyclotrons, the dose rate will be roughly equivalent in all directions for the cyclotron chambers.

Table 4-4: Dose rate shielded from cyclotron chambers with 95% extraction efficiency.

| Cyclotron | Neutron Contribution (rem/hr) | Photon Contribution (rem/hr) | Total Contribution (rem/hr) |
|---|---|---|---|
| Proton | *4.90E-4 ± 5.40E-5 | 4.90E-4 ± 5.40E-5 | 9.80E-4 ± 5.40E-5 |
| Helium | 1.42E-4 ± 7.11E-5 | 1.86E-4 ± 3.53E-5 | 3.28E-4 ± 7.94E-5 |

*The neutron contribution could not be obtained with low tally error due to the low energy spectrum of the neutrons. Even after 200 million simulations, tally error was still high due to low count rate. Linear attenuation for 1 m thick of concrete and comparison with the 100 MeV Helium Cyclotron predict a small dose rate on the order of 1-2E-4 rem/hr. For a conservative measure, the gamma dose rate contribution was adapted.

An initial MCNPX calculation of the target chamber shielding resulted in a dose rate contribution above 5 rem/yr for the 100 MeV helium beam. In order to lower the dose rate, an addition of 50 cm of concrete was added to the inside of the target chamber resulting in 150 cm thick concrete shielding walls. The results from the 150 cm shielding walls can be seen in Table 4-5, below. With the additional 50 cm of wall thickness, the dose rates listed in Table 4-4 would remain the same for locations above and in the adjacent cyclotron chamber but would be lower (~25%) if located in the target chamber.

Table 4-5: Dose Rate shielded for Target Chamber with full beam stop.

| Beam | Neutron Contribution (rem/hr) | Photon Contribution (rem/hr) | Total Contribution (rem/hr) |
|---|---|---|---|
| Proton | 7.79E-5 ± 3.12E-5 | 1.52E-4 ± 1.67E-5 | 2.3E-4 ± 3.53E-5 |
| Helium | 8.4E-3 ± 2.5E-3 | 1.2E-3 ± 2E-4 | 9.6E-3 ± 2.5E-3 |

Table 4-6 lists the Total Effective Dose Rate Limits (TEDE) in rem/yr and mmrem/year for workers. The hazard classification for Table 4-7 was determined from Table 4-6, per 105 CMR 120.211 with applied occupancy factors of 1/4[Mass.gov, 1998].

Table 4-6: Regulatory standards and guidance [Mass.gov, 1998].

| | Total Effective Dose Rate (TEDE) limits (per 105 CMR 120.211) |
|---|---|
| Occupational | 5 rem/yr |
| Public | *100 mrem/yr |
| | *2 mrem/hr |

*Whichever limit is reached first

Since the helium cyclotron will only be in operation a few days at a time and operating at an average current of 0.05 mA (half the original beam current for proper helium implantation), the helium cyclotron and respective target chamber dose contribution was not included in the Table 4-7. Table 4-7 includes the proton cyclotron and respective target chamber dose contribution at full operation for one year. To determine the total contribution during simultaneous operation, the helium cyclotron and target chamber, with applied occupancy factors and reduction in average beam current, the values listed in Table 4-4 and Table 4-5 can be added to the tabulated value in Table 4-7.

Table 4-7: Total contribution in mrem/yr for each chamber.

| Chamber Source | Maximum Total Contribution (rem/yr) | Occupancy Factor (Time in Location) | Modified Total Contribution (rem/yr) | Hazard Classification |
|---|---|---|---|---|
| Proton | 8.58 ± 0.47 | ¼ | 2.14 ± 0.12 | Occupational |
| Target with Protons | 0.68 ± 0.3 | ¼ | 0.17 ± 0.07 | Occupational |

### 4.4.4 Conclusion

As stated above, the final design was different than the proposed design described in section 4.2. The target chamber required 1.5 m thick concrete shielding walls as opposed to the proposed 1 m thick walls for adequate shielding. Thicker shielding walls were required to thermalize the high energy neutrons and photons, as seen in Figure 4-10. Both cyclotron chambers, however, still maintained a surround wall thickness of 1 m. For the reference cell and final design, the dose levels calculated, for a fully operation proton cyclotron, should be adequate even under the conservative assumptions made about the source strength. A fully operation helium cyclotron will create a TEDE above 5rem/yr, however this is not the case in reality. The helium cyclotron will only operate for days at a time, reducing is TEDE. As a result from the design of the chambers and use of symmetry, scaling can be applied to the final dose rate calculation listed in Table 4-7 for the use of different concrete, type and amount of beam intensity, or the addition of metal shielding plates. Linear scaling is a well known practice outlined in many shielding documents and books. The radiation Physics for Personnel and Environmental Protection Fermilab Report TM-1834 outlines such tenth value layer (TVL) calculations [Cossairt, 2007].

## 4.5 Suggested Design Improvements

Extra steps should be taken to reduce the TEDE for the target chamber. Possible changes could be the use a borated concrete and high density concrete or provide another localized shielding box around the target chamber. An addition of a steel or lead plate on the outside of the target chamber will also reduce the number of photons due to the material's high photon cross section.

# 5 Beam Transport

The purpose of this chapter is to explain the design process and selection of the beam transport system for both cyclotrons. The beam transport system facilitates the transport of charged particles, protons and helium, from the cyclotrons to the target chamber.

## 5.1 Arranging the Cyclotron with the Beam Transport System

The beam transport system for M²TF must be as efficient as possible entailing straight beam sections, short traveling distances to minimize beam divergence, and minimal steering components. When working with two separate beams, the beam with the lower magnetic rigidity will be chosen to merge with the other. Magnetic rigidity is the measure of how well the field can hold ions in orbit. It is expressed in terms of the magnetic field normal to which the particles are travelling [Antaya, 2010]. It can be derived from the momentum equation and rearranged to express magnetic rigidity (R):

$$\frac{p}{q} = Br = \mathrm{R} \tag{5.1}$$

The left side of Equation (5.1) is known as the ion's stiffness which opposes orbital motion in a magnetic field. The right side of Equation (5.1) is known as the magnetic rigidity (R) [Antaya, 2010]. The helium beam has a higher magnetic rigidity because of a higher combination of its radius and magnetic field. With its higher rigidity, it is advantageous to make the helium beam path as straight as possible and steer the proton beam instead.

The shielding calculations computed for the facility design had both cyclotrons placed at the center of each respective chamber. The location of each cyclotron is not permanent and can be changed with minor effects on shielding calculations because particles traveling through air have insignificant collisions and interactions with matter. The proposed beam transport system is illustrated in Figure 5-1, starting with each cyclotron at the center of their chambers. The starting beam path dimensions are summarized in Table 5-1. The restricted distance in the Table 5-1 refers to the distance the beam pipe travels through the concrete shielding walls. No quadrupole or steering element can be placed in this distance for obvious reasons.

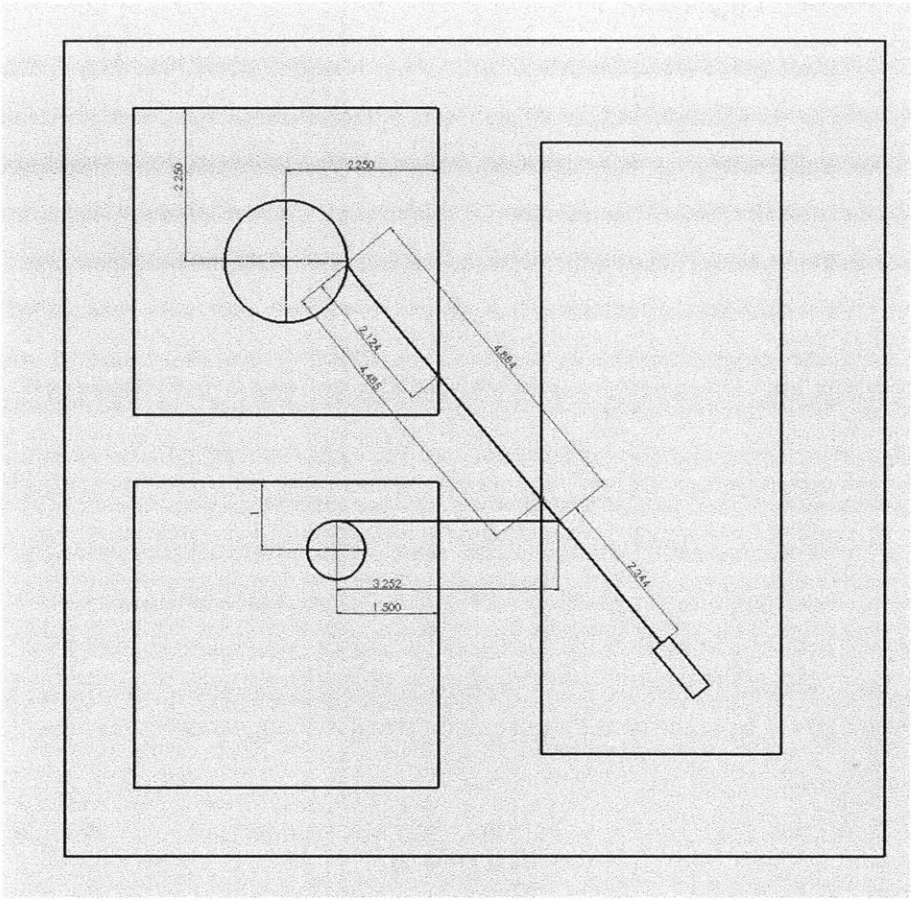


**Figure 5-1: Schematic of the starting beam transport system. The helium cyclotron is located in the top left quadrant whereas the proton cyclotron is located in the bottom left. The target chamber is located in the right quadrant. The dipole location is the intersection of the two beams.**

**Table 5-1: Starting beam path dimensions summarized from Figure 5-1.**

| Beam | Length Before Dipole (m) | Restricted Distance (m) | Sector Angle | Sector Length (m) | Length After Sector (m) |
|---|---|---|---|---|---|
| Proton | 3.252 | 1.5-3.0 | N.A. | N.A. | 2.344 |
| Helium | 4.884 | 2.124-4.485 | 50.5° | 0.5 | |

## 5.2 Initial Beam Properties

A beam pipe diameter of 7.62 cm (3 inch) was chosen for the transport system. The selected diameter is commonly used for low energy beams and is prevalent in similar beam transport

systems [Antaya, 2010]. The selected operating space for the beam was chosen to be half that diameter (38.1 mm). With this set of conditions the beam should be fully controlled minimizing any losses. Figure 5-2 illustrates the beam pipe and operating space chosen for the M²TF.

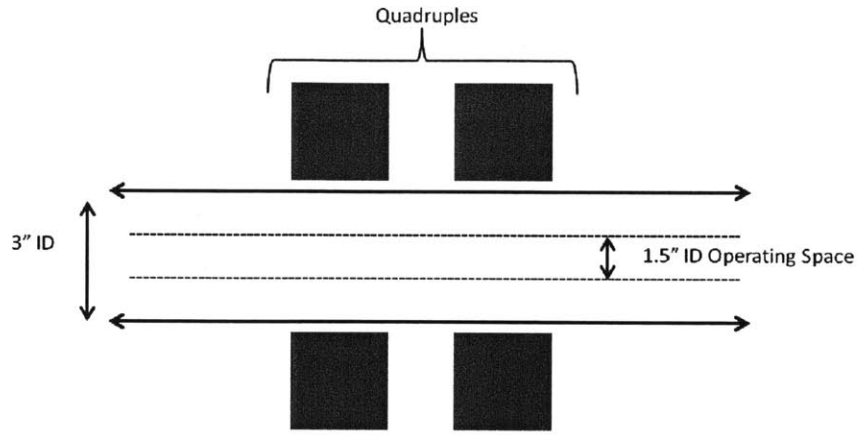


**Figure 5-2: Beam pipe specifications and selected operating space.**

**Table 5-2: Beam phase space specifications after cyclotron extraction.**

| Beam | Δx | Δx' | Δy | Δy' |
|---|---|---|---|---|
| Proton | 2 mm | 5 mrad | 2 mm | 5 mrad |
| Helium | 2 mm | 5 mrad | 2 mm | 5 mrad |

Table 5-2 lists the starting beam properties for both cyclotrons. They are similar to the exiting beam properties of other current isochronous cyclotrons [Antaya, 2010]. These values, along with energy and mass of the particle, will serve as inputs for TRANSPORT, a beam transport code. Δx and Δy are the beam's initial transverse dimensions while it travels in the z-direction. Δx' and Δy' are the beam's initial transverse divergence measure with respect to the main direction of propagation (z). Emittance is the product of the particle's beam size and divergence in units of mrad [Nolen, 2003].

As a charged particle beam travels through "drift space," the beam will diverge due to non-zero Δx' and Δy' and a space-charge-repulsion [Nolen, 2003]. Drift space is empty vacuum space not controlled by a magnetic or electric field. This effect occurs from the radial electric fields generated from the propagation of charged particle bunches. A simple calculation, ignoring space-charge-repulsion, can be completed to determine the associated drift length, based on a particular emittance, when the beam reaches the operation limit of the pipe (Figure 5-3). With the beam

specifications listed in Table 5-2, an initial drift space greater than 3 m will cause the beam to extend outside the operation space for either ion species. Referring to Table 5-1, it can be seen that both beam paths are longer than 3 m in length. Therefore, focusing and steering elements must be added to properly transport the beam to the target chamber.

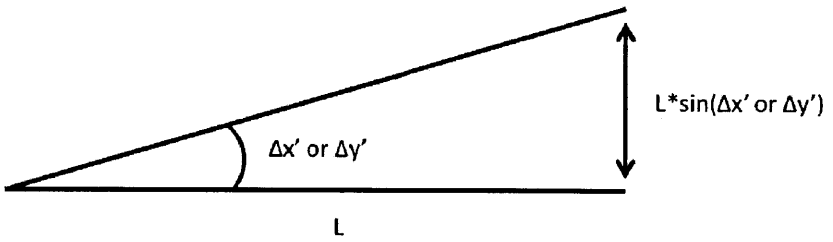


**Figure 5-3: Illustration of maximum drift space calculation with length L and divergence Δx' or Δy'.**

## 5.3 Beam Focusing and Steering Components

The focusing and steering of particles is accomplished by the use of magnetic and electric fields imposed on the charged particle. These fields create a Lorentz force that changes the particles momentum, Equation (5.2), allowing the charged particles to be deflected and therefore focused and steered inside the beam pipes.

$$F = q(\bar{v}\, x\, \bar{B} + \bar{E}) = \frac{d\bar{p}}{dt} \tag{5.2}$$

M²TF will not use electric fields for the beam transport system. Electric fields are not as strong as magnetic fields in imposing changes on the particles path [Nolen, 2003]. Instead, deflection and focusing will occur with the use of magnetic fields; in particular, dipole magnets and quadrupoles (Figure 5-4). Dipole magnets bend and focus the beam radially whereas quadrupoles just focus. The focusing of charged particles is analogous to the use of concave and convex optical lenses to focus light. However, since beam transport is controlled by phase space (6D space, 3 position and 3 orthogonal divergence components), and each direction of motion is acted on 2-3 components of the field, it is much more complex. Beam optimization becomes difficult because the number of particles in the phase space volume must be conserved [Antaya, 2010]. Therefore, much iteration is needed for an efficient design that exceeds the desired specifications.

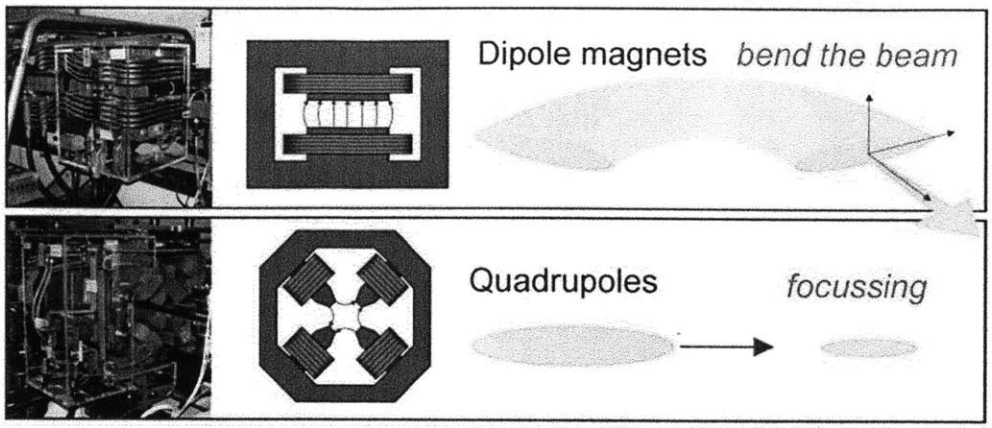


**Figure 5-4: Beam Dynamics of dipole and quadrupole with a realistic picture to the left, model in the center, and purpose on the right. Figure adapted from [Streun, 2007].**

### 5.3.1 Dipole Magnet

Dipole magnets are used to steer, deflect or merge two beams in a multitude of directions. The schematic of a dipole can be seen in Figure 5-5. $\beta_1$ and $\beta_2$ are edges angles one and two, $\rho$ is the radius of the dipole, and $R_1$ and $R_2$ are convex curvatures one and two. Pure dipole magnetic fields with normal entrance and exit angles ($\beta_1$ and $\beta_2$ edge angles $=0^o$ normal to particle motion) focus radially and bend the particles in a particular plane [Nolen, 2003]. Geometrically, dipoles focus the beam because the outer rays of the dipole have more path length exposed to the magnetic field and hence bend more; whereas the inner rays bend less [Nolen, 2003]. Edge angles placed on the ends of the dipole magnets are great tools to increase or decrease the path length of the rays in the magnet in a particular transverse direction.

### 5.3.2 Quadrupole

Quadrupoles are commonly used to focus charge particle beams. They are created by using 4 magnets of alternating north (N) and south (s) fields about the beam, with magnetic field lines, that are predominately perpendicular to the beam path (Figure 5-6) [Nolen, 2003]. The amount of deflection depends on the quadrupoles magnetic field strength (B), the radius of aperture (a), and effective length (l). Single quadrupoles can only focus one direction while defocusing the other. This may be applicable for a flat, wide beam; but for most applications, two quadrupoles are placed one after another creating a doublet. Courant and Snyder mastered this doublet formation. The details of optimizing the converging and diverging lenses will not be discussed but were implemented in

the beam design process. More information on this process can be found in Nolen's Charged-Particle Optics, [Nolen, 2003].

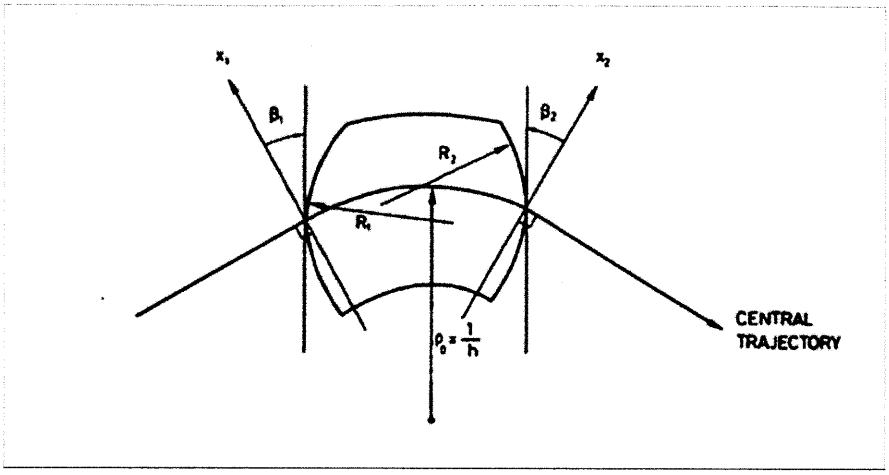


**Figure 5-5: Illustration of dipole magnet where β is the edge angle, $R_1$ and $R_2$ are convex curvatures, and ρ the radius. Figure adapted from [Nolen, 2003].**

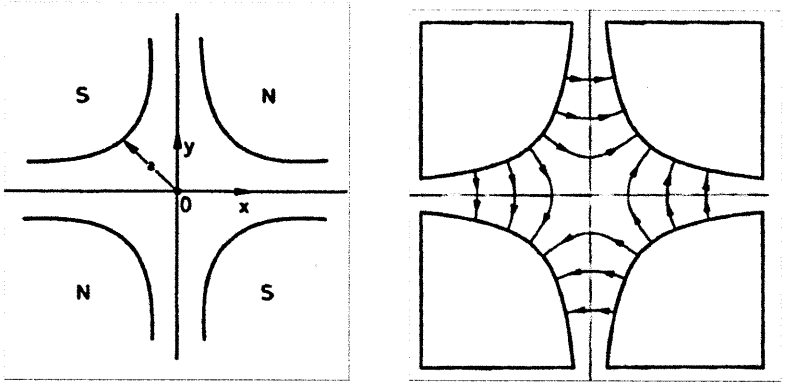


**Figure 5-6: Quadrupole magnets with aperture radius 'a' (a), origin "o," and magnetic field representation (b). Figure adapted from [TRANSPORT, 1972].**

## 5.4 Beam Transport Design

### 5.4.1 TRANSPORT

Beam transport modeling and design was done using TRANSPORT. TRANSPORT is a code that utilizes first and second order matrix multiplication for the intention of designing a static-magnetic

beam transport system [TRANSPORT, 1972]. A beam path in TRANSPORT is described by a sequence of elements. These elements include magnets, electric fields, drifts space, as well as the input parameters for each. TRANSPORT has the ability to optimize a beam based on certain parameters. This is accomplished by utilizing code 10 elements (10.xxx). Code 10 elements allow the user to select certain variables of element properties (radius, length, field, etc) that can be varied by TRANSPORT. System length constraints can also be applied with code 10 elements to ensure that a quadrupole or bending magnetic would not be placed in a restricted length zone, authorizing only drift space there. Other code numbers, the order of operation, and variable inputs will not be discussed thoroughly here. Detailed code information of each input parameter can be found in Appendix F and the TRANSPORT manual.

There are many assumptions that TRANSPORT adopts to simplify iterations and beam matrices, all of which are listed in the manual. Most assumptions were accepted for the modeling of the beam transport system. TRANSPORT's bending magnet assumption was changed to create a more realistic representation of magnets. Bending magnets in TRANSPORT are modeled with uniform fields that start and end abruptly [TRANSPORT, 1972]. Fringing field elements, code 13, allow for a more gradual variation of field when entering and exiting the element, and were applied to the TRANSPORT code.

### 5.4.2 Design Process

TRANSPORT does not allow the user to model two beams at the same time and therefore cannot be used to model the entire M²TF system at once. Instead the beam transport system must be broken up into two sections: proton beam path and helium beam path, with an overlapping shared section after the merging dipole. The proton beam consists of its focusing elements preceding the dipole bending magnet and then the focusing elements after the dipole to construct the beam envelop before entering the target chamber, recall Figure 5-1. The helium beam consists of variable elements preceding the dipole and then the same focusing elements found after the dipole in the proton beam. These focusing elements in the shared path, created in the proton beam model, must also be sufficient in focusing the helium beam. If they were not further analysis was required.

TRANSPORT was used to create a final beam envelope of 5 mm in the horizontal direction and 2 mm in the vertical direction. This beam size was needed to ensure the beam did not collide with the jet impingements or the in-situ tensile testing apparatuses. With many model restrictions, it

became quite difficult to produce feasible designs using TRANSPORT. Results were limited because TRANSPORT offers solutions that are mathematically feasible, but cannot be designed, due to unrealistic distances and lengths of optimized elements. These unrealistic results were discarded as possible beam transport solutions and the design process was repeated until a feasible result was achieved.

## 5.5 Beam Transport Final Design

Sections 5.5.1 and 5.5.2 list the final beam design for the proton and helium beam. Figure 5-7 and Figure 5-8 horizontal axes are total path length (z-axis, shown here as the x-axis) and beam envelope width (y-axis). The y-axis boundary is fixed to the operating radial limit of 19 mm. The continuous solid line in each figure signifies the beam envelope. The vertical blue lines denote the start and finish coordinates of the drift spaces. Each figure is divided into two regions; the top region illustrates the vertical component of the beam, whereas the bottom illustrates the horizontal component. Each figure also illustrates the placement of each element. Drifts, quadrupoles and dipoles are signified by the letter "D", "Q", and "B" with its consecutive number. Elements increase in number as they approach the target chamber. Tables 5-3, 5-4, 5-5, 5-6, and 5-7 summarizes each element's position, length, field, and radius (if applicable). As seen in both figures, the beam envelope is fully controlled in x and y to the position of the target chamber and never passes outside of the defined 19 mm operating space.

### 5.5.1 Proton Beam

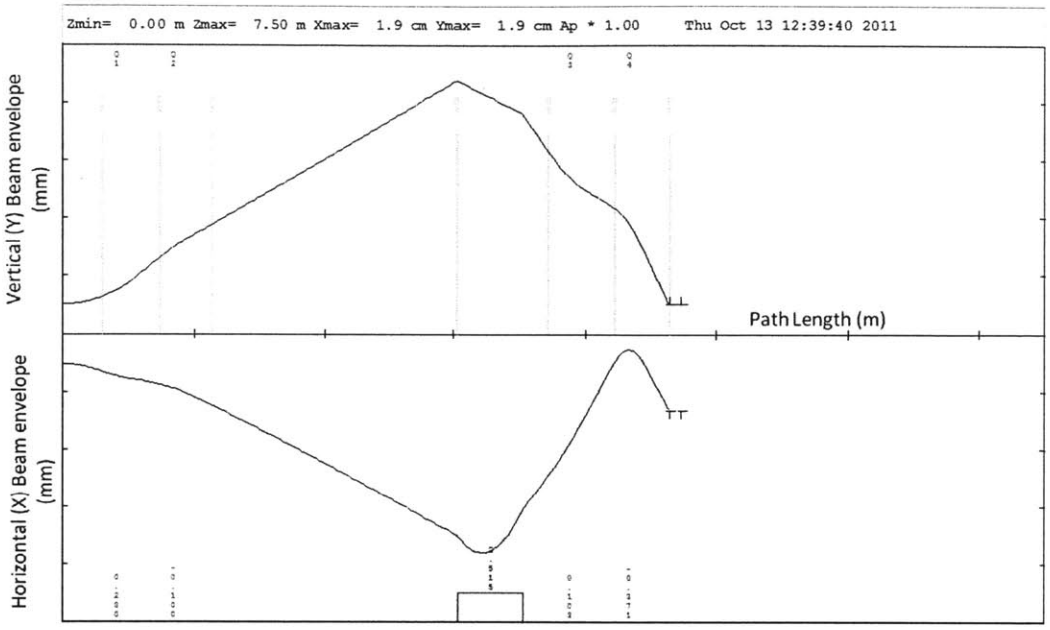


**Figure 5-7: 36 MeV Proton beam transport result. Beam envelope range of 2-19 mm. Total length of 4.8 m. The top region illustrates the vertical component of the beam, whereas the bottom illustrates the horizontal component. Each figure also illustrates the placement of each element. Drifts, quadrupoles and dipoles are signified by the letter "D", "Q", and "B" with its consecutive number. Figure generated from TRANSPORT.**

**Table 5-3: Proton beam quadrupole dimensions.**

| Quad | Z (m) | Length (m) | Field (kG) | Aperture Radius (cm) |
|---|---|---|---|---|
| Q1 | 0.530 | 0.230 | 0.20 | 3.81 |
| Q2 | 0.930 | 0.20 | -0.10 | 3.81 |
| Q3 | 4.03 | 0.30 | 0.103 | 3.81 |
| Q4 | 4.444 | 0.2239 | -0.3708 | 3.81 |

**Table 5-4: Proton beam drift dimensions.**

| Drift | Z (m) | Length (m) |
|---|---|---|
| D1 | 0.30 | 0.30 |
| D2 | 0.730 | 0.20 |
| D3 | 1.13 | 0.20 |
| D4 | 3.03 | 1.90 |
| D5 | 3.73 | 0.20 |
| D6 | 4.2204 | 0.19 |
| D7 | 4.6443 | 0.2 |

Table 5-5: Proton beam dipole magnet dimensions.

| Bending | Z (m) | Length (m) | n | Field (kG) |
|---|---|---|---|---|
| B1 | 3.53 | 0.5 | 0 | 2.515 |

## 5.5.2 Helium Beam

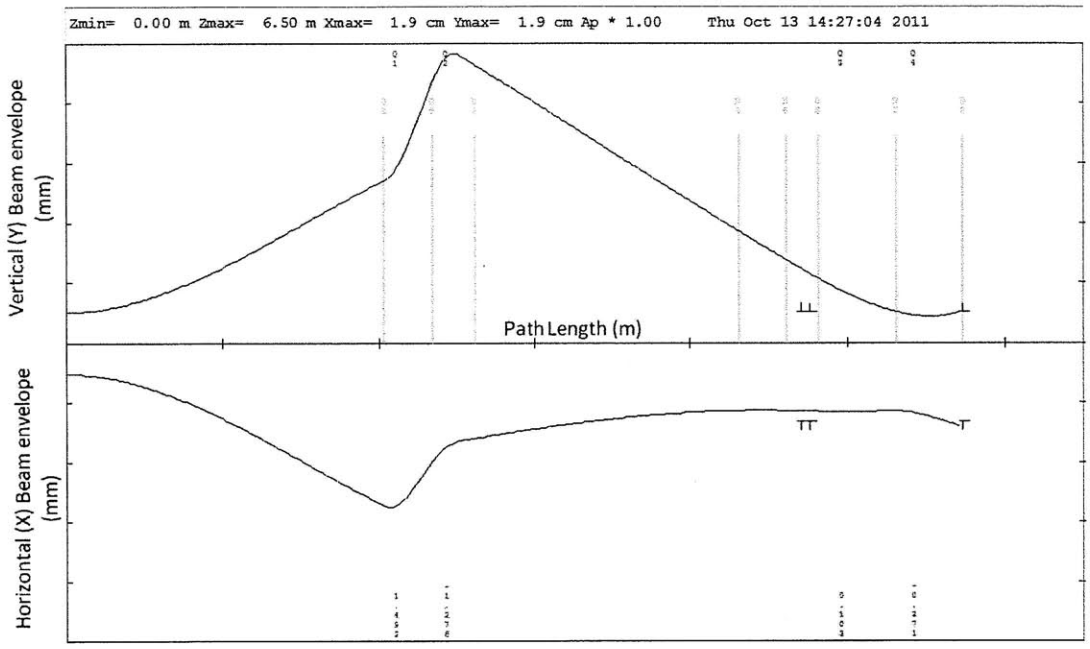


**Figure 5-8: 100 MeV Helium beam transport result. Beam envelope range of 2-19 mm. Total length of 5.8 m. The top region illustrates the vertical component of the beam, whereas the bottom illustrates the horizontal component. Each figure also illustrates the placement of each element. Drifts, quadrupoles and dipoles are signified by the letter "D", "Q", and "B" with its consecutive number. Figure generated from TRANSPORT.**

Table 5-6: Helium beam quadrupole dimensions.

| Quad | Z (m) | Length (m) | Field (kG) | Aperture Radius (cm) |
|---|---|---|---|---|
| Q1 | 2.1852 | 0.1529 | 1.492 | 3.81 |
| Q2 | 2.5191 | 0.1740 | -1.276 | 3.81 |
| Q3 | 5.1191 | 0.30 | 0.103 | 3.81 |
| Q4 | 5.5334 | 0.2239 | -0.3708 | 3.81 |

Table 5-7: Helium beam drift dimensions.

| Drift | Z (m) | Length (m) |
|---|---|---|
| D1 | 2.0322 | 2.0322 |
| D2 | 0.160 | 2.3452 |
| D3 | 2.6191 | 0.10 |
| D4 | 4.3191 | 1.70 |
| D5 | 4.6191 | 0.30 |
| D6 | 4.8191 | 0.20 |
| D7 | 5.3095 | 0.19 |
| D8 | 5.7334 | 0.2 |

## 5.6 Final Design Layout

A few issues contributed to the final design (Figure 5-9) differing from the proposed design (Figure 5-1). The design was changed to become more efficient, reducing drift lengths and number of doublet quadrupoles. The main differences between the two models were the dipole bending angle being increased slightly to minimize unnecessary drift space and the movement of the cyclotrons to create a smaller restricted length for the helium beam. Without these changes, the helium beam required two doublets before the dipole as opposed to one. Figure 5-9 provides a top down view of the final beam transport system. The figure includes shielding walls, which have been cut away for visual purposes, and illustrate the cyclotrons inside each respective chamber.

## 5.7 Feasibility of Beam Components

The next step in the design process was to model the strongest quadrupole and bending magnet to see if the elements would be engineering feasible. This was quadrupole "Q1" in the helium beam path and the only bending magnet "B1". Each element was modeled in Poisson to estimate the size of the coil and number of amp-turns. The hollow copper conductor most commonly used in this operation is a copper ¼ inch by ¼ inch wire with a hollow center [Antaya, 2010]. For such a non-superconducting coil, each individual wire is limited conservatively to carrying 200 Amps but sufficient cooling achieves 300-400 Amps.

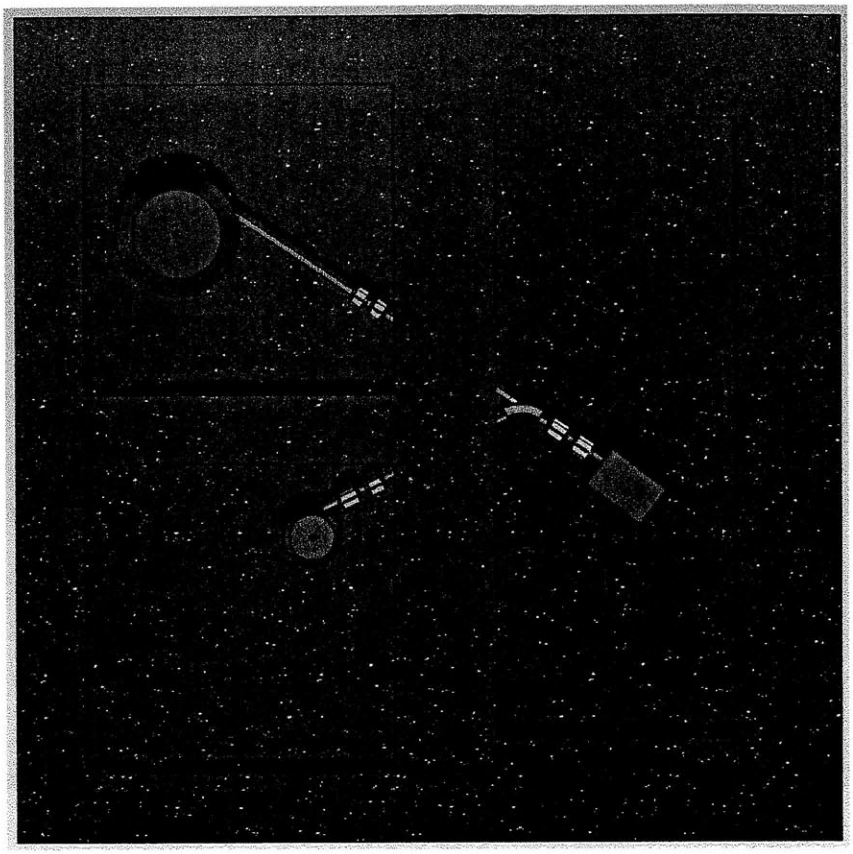

**Figure 5-9: Final beam transport layout with integrated cyclotrons (helium in upper left quadrant and proton in lower left quadrant). Dimensions are 12 m by 12 m with 1 m thick concrete shielding.**

### 5.7.1 Dipole Bending Magnet (B1)

Although the dipole is arced and 0.5 meters in length, only the middle section was modeled in 2D in Poisson. The middle section will have a constant magnetic field unaffected by fringe effects. According to TRANSPORT's output, the field at the center of the beam pipe must be 2.515 kG for this dipole to work. The strength and size of the coils were modified in Poisson until a final magnetic field was achieved. Figure 5-10a shows results for the top section of the dipole modeled in Poisson. Figure 5-10b illustrates the magnetic field reaching 2515 Gauss at the center of the beam pipe (48 cm). Table 5-8 summarizes the properties of the dipole and validates its feasibility with amp-turns of 175.

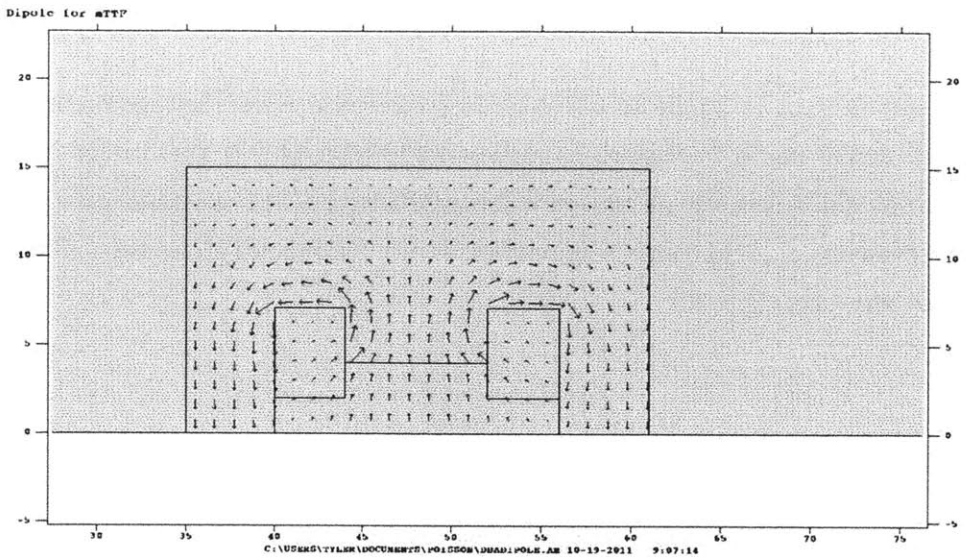


(a)

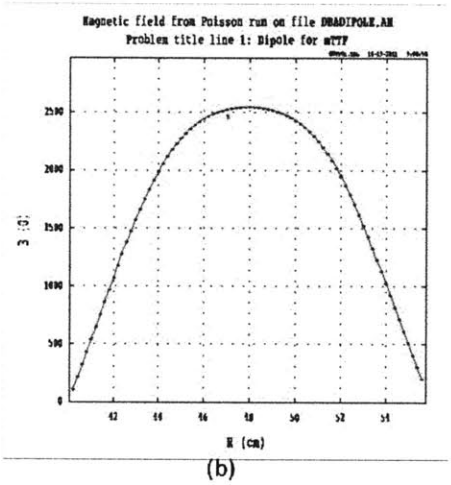


(b)

**Figure 5-10: Dipole bending magnetic "B1" feasibility calculation with Poisson. Figure (a) is the dimensions of the dipole bending magnet with vertical and horizontal axis in cm. The length of the red arrows denotes its strength and direction. Figure (b) is a magnetic field with respect to radius curve peaking at 2515 G at the center of the dipole, radius of 48 cm.**

**Table 5-8: Summary of dipole properties.**

| Height | Width | Current | Current density | # of ¼" Copper conductors | Amp-turns |
|---|---|---|---|---|---|
| 5.08 cm | 4 cm | 8400 A | 413 A/cm$^2$ | 48 | 175 |

## 5.7.2 Quadrupole (Q1)

The quadrupole "Q1" was modeled with 4 sector symmetry to reduce calculation time. The field at the pole tip (labeled 'a' in Figure 5-6) must be 1.492 kG or 1492 G. The strength and size of the coils were modified to prevent an amp-turn above 200. Figure 5-11 illustrates Poisson's generation of the magnetic field. Table 5-9 summarizes the quadrupoles properties and validates its feasibility with amp-turns of 130.5.

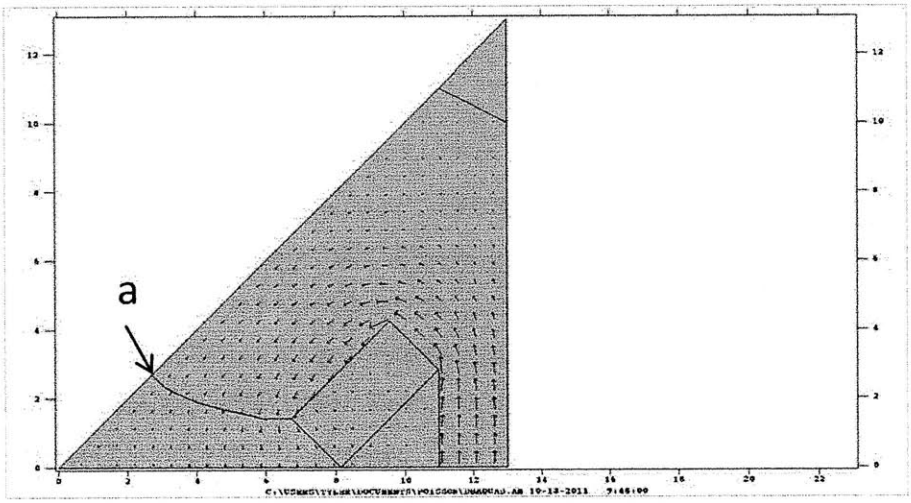


**Figure 5-11: Poisson Generation of magnetic field for quadrupole "Q1". The length of the red arrows denotes its strength and direction.**

**Table 5-9: Summary of quadrupole Properties.**

| Height | Width | Current | Current density | # of ¼" Copper conductors | Amp-turns |
|---|---|---|---|---|---|
| 4 cm | 2 cm | 2350 A | 294 A/cm$^2$ | 18 | 130.5 |

# 6 Concluding Remarks

## 6.1 Summary of project

The goal of this thesis was to develop and optimize a beam transport and delivery system with two superconducting cyclotrons (a 36 MeV proton and 100 MeV helium) in the M²TF concept. Proton and helium beams were needed to conduct a multitude of irradiation experiments. Duel cyclotrons would allow for the production of high DPA rates, a flexible helium/DPA ratio, and rapid helium implantation. This facility would allow the study of almost any reactor system and material condition. Both cyclotrons were chosen to be isochronous machines because of the need for a continuous wave of particles and high intensity beam. The cyclotrons were optimized around 4T, stronger magnetic field machines had issues with orbital stability. A detailed shielding analysis, conducted with MCNPX, showed that the facility would be safe and under the legal limits pertaining to the total effective dose rate. The shielding layout also allows for maintenance on one of the cyclotrons while the other is in operation, increasing the facility's reliability. The beam transport system was designed using TRANSPORT and optimized with short travelling distances, minimal turns and bends, and minimal focusing elements.

Many of the configurations and results of this thesis can be scaled to cope with changes in beam current density or the use of other materials. Tenth value layers can be added to account for the addition of lead plates or thicker concrete walls if additional shielding is needed. The cyclotrons and beam transport system were designed based on the particles final energy. If the beam current density was increased by an order of magnitude there would be no changes in the overall design. The issue would be in particle losses during beam extraction.

There are still many arguments that proton irradiation does not fully replicate all effects of neutron irradiation. Regardless of the arguments, M²TF can be used to benchmark proton irradiation as a tool for simulation neutron damage.

## 6.2 Future work

During the study of the design and optimization of a multi-particle beam transport delivery system for M²TF, many opportunities for future work have been noted. The following sub-sections briefly discuss a few of these ideas.

### 6.2.1 Activation of Material Study

The activation of the materials would be of great interest to know. Every material in the chamber will be exposed to radiation and will become activated. A sample that is irradiated for over a year will be extremely 'hot' and may require significant time before it can be handled. Such activation timeframes need to be completed in order to determine time frames for safe entry of chambers and safe handling of the sample.

### 6.2.2 Beam Extraction

Most commonly, positive ions are extracted by an electrostatic detector. The electrostatic detector consists of two electrodes located at the extraction radius of the cyclotron [Strijckmans, 2001]. On the ion's last rotation, the ion experiences a strong electric field that directs it outward, tangential from its orbit. The limits and details of the beam extraction process have not been researched. It would be important to investigate the efficiency of extraction of higher power beams greater than 0.1mA/cm².

### 6.2.3 Energy Degrader Option

Section 2.3 indicates that the helium energy needs to be varied in order to create a uniform deposition. There are many ways that this can be done. Some possible ideas are using a rotating step or wedged wheel, a movable wedge, or a stack of foils [ASTM E942-96, 2011]. Similar to the helium implantation calculations, heat removal will be an issue because at times the degrader will stop 100% of the beam. Issues in employing titanium windows to separate it from the vacuum beam pipe and scattering analysis of the beam would need to be investigated. The choices of materials for the degrader accepted in practice by ASTM E942-96 are aluminum, beryllium, and graphite. The stopping power of these materials is well known and simulations with MCNPX and

SRIM could provide some insight into the feasibility of this idea and the engineering details of the degrader.

### 6.2.4 More Accurate Shielding Calculation

The current shielding layout design is sufficient for providing a safe work environment during operation. More detail could be added to the MCNPX model to improve accuracy. The concrete modeled in MCNPX is ordinary concrete without rebar. A 1 m thick concrete slab, due to mechanical reasons, will require rebar reinforcement. Since rebar is made of steel, it will have an effect on the scattering and production of particles travelling through the concrete. Another MCNPX analysis could be conducted with the addition and placement of rebar inside the concrete and actually concrete characteristics from an outside provider. Another shielding calculation will need to be completed that includes the beam transport system. The addition of this material will affect the shielding calculations. For each cyclotron modeled, the energy of the source was the final energy; this is not true in reality. A more accurate calculation would incorporate a source that consisted of a range of energies. As discussed in the "Addressing the Concern of Damage Cascade Timescales," for an isochronous cyclotron there will be an instantaneous rate of damage one order of magnitude greater than the average. The instantaneous current was not incorporated into the shielding results and its effect should be studied further.

The proposed shielding design was modeled for concrete removable doors, not a maze design. If a maze design is adapted more work must be completed to investigate the potential scatter of particles through the maze. The maze design is well established in the medical field and many details and scalable designs can be found in [Patton, 2007]. A MCNPX model of the new maze design can validate its safe use.

The affect of the introduction of unwanted particles in the beam due to radiation is unknown and should be further analyzed. The report published by Fermilab cautions that the beam path be shielded from any strong sources of radiation. Radiation could introduce particles into the beam path, disrupting beam transport [Cossairt, 2007]. Since the beam is controlled magnetically as opposed to electronically, no stray particles should be accelerated in the beam, but these stray particles could cause unnecessary collisions in the beam pipe.

# 7 Bibliography


Abromeit, C. (1994). Aspects of simulation of neutron damage by ion irradiation. *Journel of Nuclear Materials* (216), 78-96.

Adams, J. B. (1994). Atomic-Level Computer Simulation. *Journal of Nuclear Materials* , 265-274.

Antaya, T. (2010). Comprehensive Introduction to Cyclotron Science and Technology. M.I.T, U.S.A.

Antaya, T. (2011, July 25). Cost Estimate of Cyclotron. (T. Sordelet, Interviewer)

ASTM E112-10. (2010). *Standard Test Methods for Determining Average Grain Size.* West Conshohocken: ASTM International.

ASTM E521-96. (2000). *Standard Practice for Neutron Radiation Damage Simulation by Charged-Particle Irradiation.* West Conshohocken: ASTM International.

ASTM E942-96. (2011). *Standard Guide for Simulation of Helium Effects in Irradiated Metals.* West Conshohocken: ASTM International.

Barnard, H., Ferry, S., & Payne, J. (2010). *TSTARC: The site for Testing of Advanced Reactor Material Concepts.* Nuclear Science and Engineering. Cambridge: MIT.

Block, R. (2011). *Acfields: Semi-Analytics Cyclotron Fields using a Python/Fortran Hybrid Code.* Cambridge: MIT PSFC.

Block, R. (2011). *Thesis-Electron Beam Dynamics for the ISIS Bremsstrahlung Beam Generation System* . Cambridge: MIT.

Britannica. (2011). *Particle Accelerator.* Retrieved October 5, 2011, from Encyclopaedia Britannica: http://www.britannica.com/EBchecked/topic/445045/particle-accelerator

Bruker. (2011). *Low Temperature Super Conductors.* Retrieved Oct 28, 2011, from Bruker Coorporation: http://www.bruker-est.com/nbti.html

Callister, W. D. (2010). *Materials Science and Engineering, An Introduction* (8th ed.). New York: John Wiley & Sons.

Cossairt, J. D. (2007). *Radiation Physics for Personnel and Environmental Protection: Fermilab Report TM-1834 Revision 9B.* 1-336: Fermi Natiaonl Accelerator Laboratory.

Ferrari, A., Fasso, A., & Birattari, C. (1988). *Shielding Calculations for the Milan Superconducting Cyclotron.* Geneva: CERN.

Griffiths, R. (1989). A Superconducting Cyclotron. *Nuclear Instruments and Methods in Physics Research* , 881-883.

Grunder, H. A., & Selph, F. B. (1977). Heavy-Ion Accelerators. *Annular Review of Nuclear Science* , 353-92.

Grunder, H., & Selph, F. (1977). Heavy-Ion Accelerators. *Annual Review of Nuclear Science* , 353-92.

Heinisch, S., & Martinez, C. (1986). Spectral Effects in Low-dose Fission and Fusion Neutron Irradiated Metals and Alloys. *Journal of Nuclear MAterials* , 807-815.

IEA. (2011). *Main Parameters.* Retrieved January 10, 2011, from The International Fusion Materials Irradiation Facility (IFMIF): http://www.frascati.enea.it/ifmif/

K, Katoh, Y., Ando, M., & Kohyama, A. (2003). Radiation and Helium Effects on Microstructures nan-indentation Properties and Deformation Behavior in Ferrous Alloys. *Journal of Nuclear Materials* , 251-262.

Kleuh, R., Ehrlich, K., & Abe, F. (1992). Ferritic/Martensitic Steels: Promises and Problems. *Journal of Nuclear Materials* , 191-194.

Kulcinsji, G., Brimhall, J., & Kissinger, H. (1972). Production of voids in pure metals by high-energy heavy-ion bombardment. *Proceedings of Radiation-Induced Voids in Metals, CONF-710601* , 453.

LAACG, L. A. (1976). Poisson Superfish.

Lamarsh, J. (2001). *Introduction to Nuclear Engineering.* Upper Saddle River, NJ: Prentice Hall.
Lee-Whiting, G., & Davies, W. (1994). Analytic Representation of Cyclotron Magnetic Field. *IEEE Transactions on Magnetics, 30* (4), 1663-68.
Lindhard, J., & Scharff, M. (1963). Material Fys. Medd. Dan. Vid. *Selsk, 33* (10).
Logan, C. (1973). Proton Simulation of Displacement Effects Induced in Metals by 14 MeV Protons. *Journal of Nuclear Materials*, 223-232.
Mass.gov. (1998). *105 CMR: Department of Public Health, Standards for Proetcion against Radiation.* Retrieved from Health and Human Services: http://www.mass.gov/Eeohhs2/docs/dph/regs/105cmr120_200.pdf
MCNPX. (2008). *MCNPX User's Manual.* Los Alamos National Laboratory.
Miller, J. (2003). Proton and Heavy Ion Accelerator Facilities for Space Radiation Research. *Gravitational and Space Biology Bulletin*, 19-28.
MIT. (n.d.). *Plasma Science and Fusion Center (NW21) Floorplan.* Retrieved October 5, 2011, from MIT Campus Map: whereismit.edu
MSU. (2011). *National Superconducting Cyclotron Laboratory.* Retrieved Oct 18, 2011, from http://www.nscl.msu.edu/
Nelson, R. (1970). The use of Ion Accelerators to Simulate Fast- Neutron Voidage in Materials. *Journal of Nuclear Materials*, 1-12.
Nolen, J. A. (2003). Charged-Particle Optics. *Encylopedia of Applied Physics*, pp. 273-305.
NRC. (2011, August). *Lethal Dose (LD).* Retrieved September 15, 2011, from U.S.NRC: http://www.nrc.gov/reading-rm/basic-ref/glossary/lethal-dose-ld.html
NRC. (1988, May). *Regulatory Guide 1.00, Revision 2.* Retrieved October 12, 2011, from U.S. NRC: http://pbadupws.nrc.gov/docs/ML0037/ML003740284.pdf
Opera-3d. (2009). *Opera-3d Reference Manual.* ERA Technology Limited Trading as Cobham Technical Services.
Patton, H. M. (2007). Shilding Techniques for Radiation Oncology Facilities. *Medical Physiscs*.
Raj, B., & Vijayalakshmi, M. (2009). Challenges in Materials Research for Sustainable Nuclear Energy. *Materials Research Society, 33*, 327-342.
Robinson, M. T., & Torrens, I. M. (1974). Computer Simulation of Atomic-displacement Cascades in Solids in the Binar-collision Approximation. *Physical Review B, 9* (22), 1-17.
Robinson, M., & Norgett, M. (1975). A Proposed Method of Calculating Diplacements Dose Rates. *Nuclear Engineering and Design, 33*, 50-54.
San, J.-Y. (1997). Impingement cooling of a confined circular air jet. *International Journal of Heat Mass Transfer*, 1355-1364.
San, J.-Y., Huang, C.-H., & Shu, M.-H. (1997). Impingement Cooling of a Confined Circular Air Jet. *Journal of Heat and Mass Transfer*, 1355-1364.
Sickafus, K. E., Kotomin, E. A., & Uberuaga, B. P. (2007). *Radiation Effects in Solids.* Netherlands: Springer.
Streun, A. (2007). *Beam Dynamics Overview 3: Transverse Beam Dynamics.* Retrieved Oct 25, 2011, from People.Web: http://people.web.psi.ch/streun/empp/hpart3.pdf
Strijckmans, K. (2001). The isochronous cyclotron: principles and recent developments. *Computerized Medical Imaging and Graphics*, 69-78.
*Supercon Inc.* (2011). Retrieved October 4, 2011, from Standard NbTi Supercon Conductors: http://www.supercon-wire.com/products_nbti.html
TRANSPORT. (1972). A Computer program for designing charged particle beam transport systems. Standford Linear Accelerator Center.
Was, G. (2002). Emulation of Neutron effects with Protons: Validation of the Principle. *Journal of Nuclear Materials*, 198-216.
Was, G. S. (2007). *Fundamentals of Radiation Material Science.* New York: Springer.
Whyte, D. (2010, Septemeber 20). Helium Displacement Levels. (T. Sordelet, Interviewer)

Youngblood, D., & Bronson, J. (1994). Beam Analysis system for Texas A&M K500 cyclotron. *Nuclear Instruments & Methods in Physics Research* , 37-45.

Ziegler, M., & Biersack, J. (1984). SRIM, The Stopping and Range of Ions in Matter.

Zinkle, S. (2007). *OECD NEA Workshop on Structural MAterials for Innovative Nuclear Energy Systems*. Retrieved November 15, 2010, from Stanford: http://gcep.stanford.edu/pdfs/UVaodfDrAb3BdgeRCpoy-w/10-Zinkle-GCEP-Workshop.pdf

# Appendix A: *Acfields* Code

## A.1 Proton Cyclotron

```
## ------------------------------------------------------------
## Proton Model
## Program Created By: R.E. Block, reblock@alum.mit.edu
## ------------------------------------------------------------

## MODULE IMPORTS ----------------------------------------------
import datetime
now = datetime.datetime.now
from numpy import pi

## USER DEFINE ALL CONSTANTS HERE ------------------------------
# Units should be in cm, Tesla, and radians

# First Define cyclotron parameters - - - - - - - - - - - - - - - - - - -
spiral = True # Set to false for simple radial sectors
rmax = 24.5    # Pole radius for spiral
rmin = 1.5    # Diameter of central hole in spiral
nr = 35       # Number of segments on side of spiral
nt = 15       # Number of segments on arc of spiral/ radial sector
a1 = 3.51     # Spiral angle of front edge (theta_0=0) (leave even if sector)
a2 = 3.51     # Spiral angle of back (theta_0= pi/nsectors) edge
nsector = 3.0  # Number of sectors in 360 degrees
ntrings= nt*2*nsector # number of points in a ring
mat1 = 'Ho'    # Material label for face of pole
M1 = 2.06     # Magnetization, 3.00 for Ho, 2.06 for Fe
gap = 1.5     # One-half gap height in centimeters
top = 10.5    # Yoke height
# Dimensions and parameters for field points - - - - - - - - - - - - - - - -
nft = 150     # Number theta plot from ftmin to ftmax-(ftmax/ntheta)
nfr = 100     # Number of points to plot in radius from 0 to RMAX
ftmin = 0     # Starting theta value for plot
ftmax = 2*pi/nsector # End theta value for plot
frmin = 0.01     # Starting r value for plot
frmax = 21    # max r to plot
z = 0.0       # z height for plot
numcontour=25  # Number of contours in contour plot
# Other inputs - - - - - - - - - - - - - - - - - - - - - - - - - - - - - -
mo = 938.272   # Proton rest mass energy in MeV
mass = 1.0     # Mass relative to proton
charge = 1.0   # Charge relative to proton.  Always positive
energy = 36.0     # Final energy in MeV
bo = 4.28      # Estimated B0 for isochronous field
nmoments=9     # Number of moments for expansion of yoke fields
yokefile='5t_high_cd'  # table file where yoke field is stored
yokescale=1.0  # Factor which artificially scales the yoke fields
modelname='5trev3' # a unique model name

## THIS SECTION FOR DEFINING RINGS AND CUTS TO THE POLES ------------

## Cuts to the poles and rings are defined in two lists, each with values
## defining the cylinder (r,t,h1,h2) where r is the max radius, t is thickness
## (set t to 0 for a full cylinder), h1 is starting z, h2 is ending z

rings=[]#[24.5,0.5,8,top,M1]]#[[14.0,2.5,3.0,top,M1]]#[[52.0,5.0,5.0,top,M1]]

# Ringparams are [material name, element size, data storage level]
# Must be specified for each ring
#ringparams=[[mat1,1.5,90]]
```

```
# Cuts just use [r,t,h1,M],
# list cuts by increasing radius
# r is outer radius, t is radial thickness of cut, h1 is height
cuts=[[5,5-rmin,top,M1],[10.0,5.0,top-1.6,M1],[15.0,5.0,top-3.8,M1],[18.0,3.0,top-5.75,M1],[19,1,top-6.9,M1],[20,1,top-
6,M1],[22.5,2.5,top-0.01,M1],[24.5,2,top,M1]]#[[13,2,10.8,M1]] #[[35.0,35.0-rmin,12.0,M1],[42.0,42.0-35.0,11.0,M1]]

## THIS SECTION FOR CODE PARAMETER AND OUTPUT CONTROL ----------
plotlines= True# Used for plotting of integration lines
plotyoke= True # Plot yoke fields and approximation
plotfields3d=False# Generate 3d surface plot of fields
plotfieldscont=False # Contour plot of fields
plotiso= True  # Plot isochronous field
plotparams= True # Plot cyclotron parameters
savedata=False   # Save data to .out file
loaddata=False  # Load external fields, not implemented
```

## A.2 Helium Cyclotron

```
## ----------
## Helium Model
## Program Created By: R.E. Block, reblock@alum.mit.edu
## ----------

## MODULE IMPORTS ----------
import datetime
now = datetime.datetime.now
from numpy import pi

## USER DEFINE ALL CONSTANTS HERE ----------
# Units should be in cm, Tesla, and radians

# First Define cyclotron parameters ----------
spiral = True # Set to false for simple radial sectors
rmax = 57.5    # Pole radius for spiral
rmin = 1.5    # Diameter of central hole in spiral
nr = 35       # Number of segments on side of spiral
nt = 15       # Number of segments on arc of spiral/ radial sector
a1 = 4.81     # Spiral angle of front edge (theta_0=0) (leave even if sector)
a2 = 4.81     # Spiral angle of back (theta_0= pi/nsectors) edge
nsector = 3.0  # Number of sectors in 360 degrees
ntrings= nt*2*nsector # number of points in a ring
mat1 = 'Ho'    # Material label for face of pole
M1 = 2.06     # Magnetization, 3.00 for Ho, 2.06 for Fe
gap = 1.5     # One-half gap height in centimeters
top = 25    # Yoke height
# Dimensions and parameters for field points ----------
nft = 150      # Number theta plot from ftmin to ftmax-(ftmax/ntheta)
nfr = 100      # Number of points to plot in radius from 0 to RMAX
ftmin = 0      # Starting theta value for plot
ftmax = 2*pi/nsector # End theta value for plot
frmin = 0.01     # Starting r value for plot
frmax = 45   # max r to plot
z = 0.0       # z height for plot
numcontour=25  # Number of contours in contour plot
# Other inputs ----------
mo = 938.272   # Proton rest mass energy in MeV
mass = 4.0     # Mass relative to proton
charge = 2.0   # Charge relative to proton.  Always positive
energy = 100.0     # Final energy in MeV
bo = 3.885     # Estimated B0 for isochronous field
nmoments=9     # Number of moments for expansion of yoke fields
```

```
yokefile='helium_med_5' # table file where yoke field is stored
yokescale=1.0  # Factor which artificially scales the yoke fields
modelname='helium_med' # a unique model name

## THIS SECTION FOR DEFINING RINGS AND CUTS TO THE POLES ----------

## Cuts to the poles and rings are defined in two lists, each with values
## defining the cylinder (r,t,h1,h2) where r is the max radius, t is thickness
## (set t to 0 for a full cylinder), h1 is starting z, h2 is ending z

rings=[[50,5,16,top,M1],[57.5,7.5,16,top,M1]]#[[14.0,2.5,3.0,top,M1]]#[[52.0,5.0,5.0,top,M1]]

# Ringparams are [material name, element size, data storage level]
# Must be specified for each ring
#ringparams=[[mat1,1.5,90]]

# Cuts just use [r,t,h1,M],
# list cuts by increasing radius
# r is outer radius, t is radial thickness of cut, h1 is height
cuts=[[5,5-rmin,top,M1],[10.0,5.0,top,M1],[15.0,5.0,top,M1],[20.0,5.0,top,M1],[25,5,top-3.5,M1],[30,5,top-4.8,M1],[35,5,top-
5.5,M1],[45.5,10.5,top-6.5,M1]]#[[13,2,10.8,M1]] #[[35.0,35.0-rmin,12.0,M1],[42.0,42.0-35.0,11.0,M1]]

## THIS SECTION FOR CODE PARAMETER AND OUTPUT CONTROL ----------
plotlines= True# Used for plotting of integration lines
plotyoke= False # Plot yoke fields and approximation
plotfields3d=False# Generate 3d surface plot of fields
plotfieldscont=False # Contour plot of fields
plotiso= True  # Plot isochronous field
plotparams= True # Plot cyclotron parameters
savedata=False   # Save data to .out file
loaddata=False  # Load external fields, not implemented
```

# Appendix B: Opera Instructions

1. Create Model in SolidWorks
    a. Save as .igs
2. Create Model in 3D modeler
    a. Create→ load 3d model→ .igs
    b. Rotate model until Z axis is center axis
    c. Assign material properties
        i. Right click→cell properties→Mesh and Data Storage
            1. Mesh of 2
            2. Data Storage # >10
3. Create Conductor
    a. Use conductor tab, insert (x,y) corners
    b. 0,0,0,0 curves
    c. Current density 20,000-44,000 A/cm$^2$
    d. Symmetry in YZ
    e. Rotate conductor until Z axis is center axis
4. Create Air Cylinder
    a. Use cylinder tab
    b. Assign as air
    c. Right click→cell properties→Mesh and Data Storage
        i. Mesh of 2
        ii. Data Storage # <10
5. Assign remaining material properties for other objects if applicable
6. Model→Material properties
    a. Select Iron Pieces→Select Non-Linear→Name
7. Model →Set BH curve properties
    a. Select Iron Pieces→Load→tenten.bh
8. Model → Model Symmetry
    a. Select boundary Sphere, Radius >10
    b. Symmetry around Z-axis, 4 cuts, Z-positive
    c. XY perpendicular

9. Model → Create Model Body
10. Model→TOSCA Magnet statics settings
    a. Select →Non-linear
11. Model →Generate surface mesh
    a. Chose background size of 10-15
12. Model → Generate volume mesh
    a. Choose Default
13. Model → Create analysis Database
    a. Save in different folder
    b. Run
    c. Open Post Processor
14. Plot →polar patch at (r,0, complete disk)
    a. Select Bz, if not it will default to X
    b. Chose Radius and number of pts
15. Tables→ Read/Write
    a. Choose X, Y, Bz
    b. Change units of Bz to Flux
    c. Change number of columns to 3
    d. Saves as name.table
16. Start Matlab program
    a. Load data and hit solve button

# Appendix C: Matlab Code for Opera Data

## C.1 Inner Coil Field Contribution

```
% Matlab code to find avg Bz and Btheta given X,Y,Bz from Opera 3D
% add field bump
% created by Tyler Sordelet

clc
close all
clear all

labels=['r','b','g','k','y','c'];          %plot labels
names=['helium_3.9T.table'];
BZ={};                                     %Creating Magnetic Cell
R={};                                      %Creating Radius Cell

for k=1:size(names,1);
   imported_data=importfile(names(k,:));     %Imports Opera Table
   data=imported_data.data;                  %Extracts Data

   x=importdata(names(k,:));                 %grabs n
   n=x(1,1);                                 %radius points
   nt=x(1,2);                                %Theta Points
   bz=zeros(nt,n);
for i=1:n
   for j=1:nt
   bz(j,i)=data((j-1)*n+i,3);                %Builds Bz Matrix
   end
end
   r_p=sqrt(data(1:n,1).^2+data(1:n,2).^2);  %Builds R Matrix
   R{k}=r_p';
   BZ{k}=mean(bz)./1e+4;                     %Converts & Stores in cell
end

% Adding Bump
bump=importdata('INNER_900.TXT)';
bump_r=bump(1,:);
bump_b=bump(2,:)/10000;
bump_field=bump_b+BZ{1};

% For theoretical
B_o=3.895;
a=938.2723/(299*B_o);
r_f=sqrt(a^2*(1-1/1.02614^2)*4)*100;
rr=0.1:0.05:r_f;
ideal=B_o./sqrt((1-(rr./(100*2*a)).^2));

hold on
for l=1:size(names,1);
plot(R{l},BZ{l},labels(l))
title('Avg Bz(r) for all theta')
ylabel('Avg Magnetic Field (T)')
xlabel('Radius (cm)')
legend(names,'location','NorthWest')
grid on
end
plot(rr,ideal,'k')
plot(R{l},bump_b+BZ{l},'b')
hold off
```

## C.2 Comparison of Multiple Opera-3D Designs

```
% Matlab code to find avg Bz and Btheta given X,Y,Bz from Opera 3D
% created by Tyler Sordelet
$ Comparision of Design

clc
close all

labels=['r','b','g','k','y','c'];          %plot labels
names=['rev29_5T.table';'rev30_5T.table'];
BZ={};                                     %Creating Magnetic Cell
R={};                                      %Creating Radius Cell

for k=1:size(names,1);
   imported_data=importfile(names(k,:));     %Imports Opera Table
   data=imported_data.data;                  %Extracts Data

   x=importdata(names(k,:));                 %grabs n
   n=x(1,1);                                 %radius points
   nt=x(1,2);                                %Theta Points
   bz=zeros(nt,n);
for i=1:n
   for j=1:nt
   bz(j,i)=data((j-1)*n+i,3);                %Builds Bz Matrix
   end
end
   r_p=sqrt(data(1:n,1).^2+data(1:n,2).^2);  %Builds R Matrix
   R{k}=r_p';
   BZ{k}=mean(bz)./1e+4;                     %Converts & Stores in cell
end

%load hs5txt.txt

% For 5T theoretical
rr=0.1:0.1:13.8;                           %Ideal calculations
a=0.523005747; %6T
ideal=6./sqrt((1-(rr/(100*a)).^2));

hold on
for l=1:size(names,1);
plot(R{l},BZ{l},labels(l))
title('Avg Bz(r) for all theta')
ylabel('Avg Magnetic Field (T)')
xlabel('Radius (cm)')
legend(names,'location','NorthWest')
grid on
end
plot(rr,ideal,'k*')
%plot(hs5txt(:,1),hs5txt(:,3)/10000,'c')
hold off
```

# Appendix D: Layout Drawings

## D.1 Proton Cyclotron

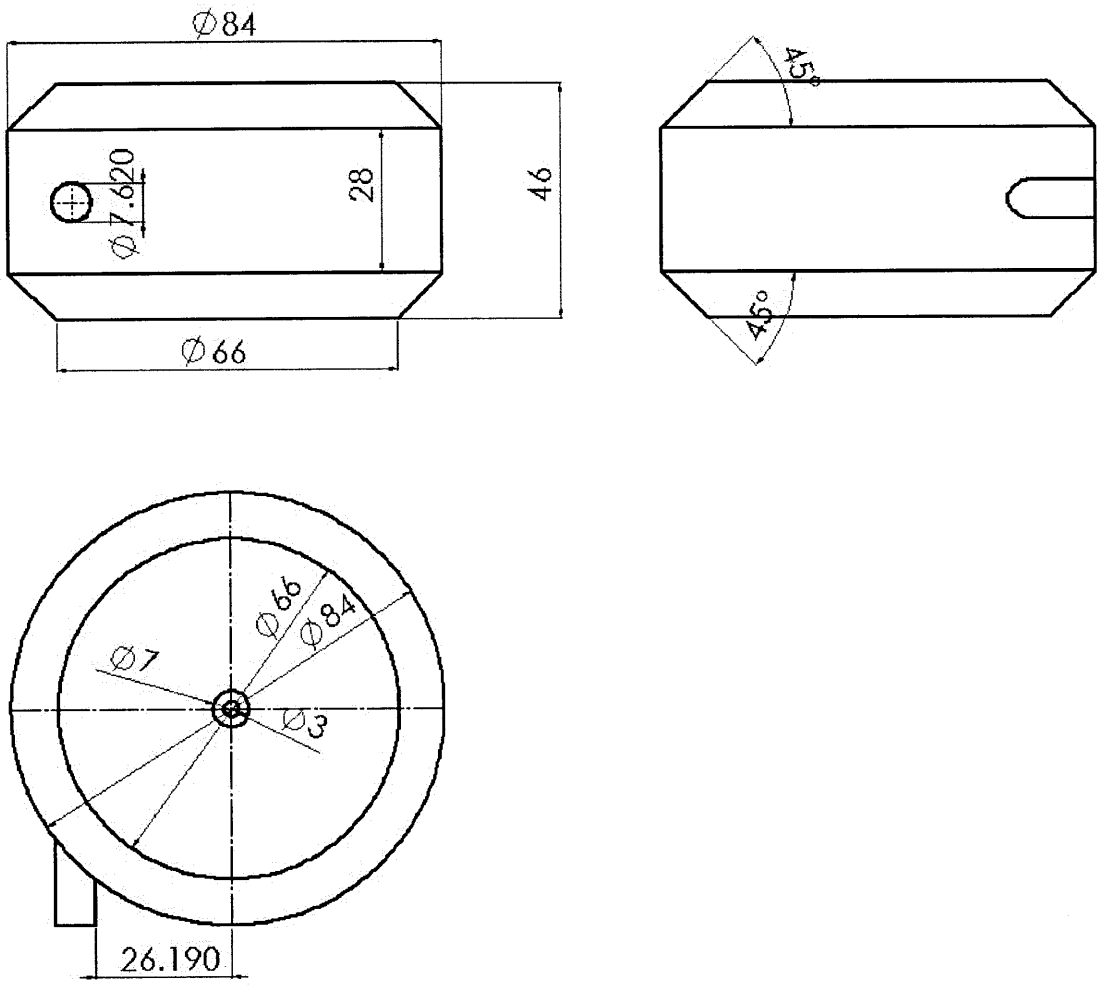

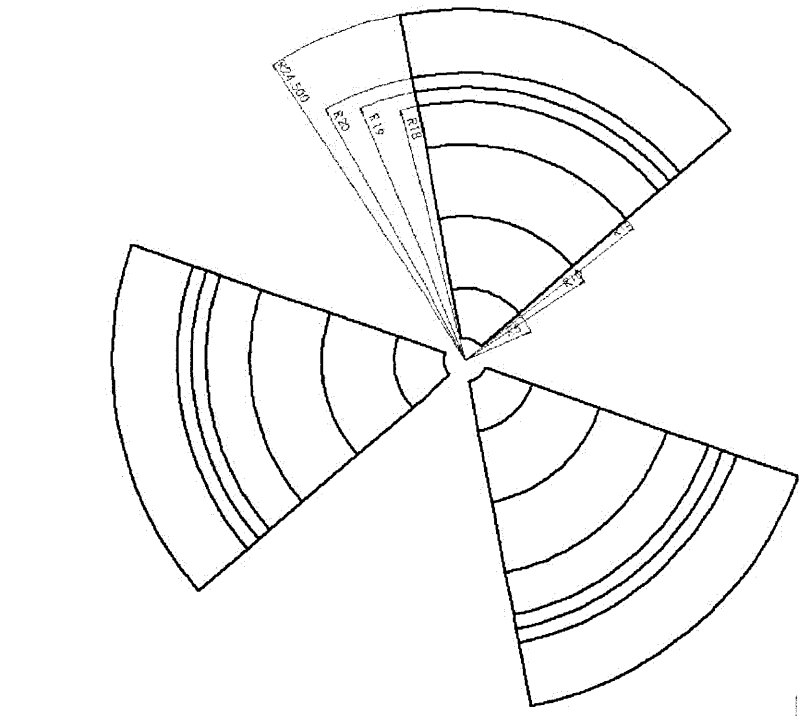
R24.50
R20
R19
R18

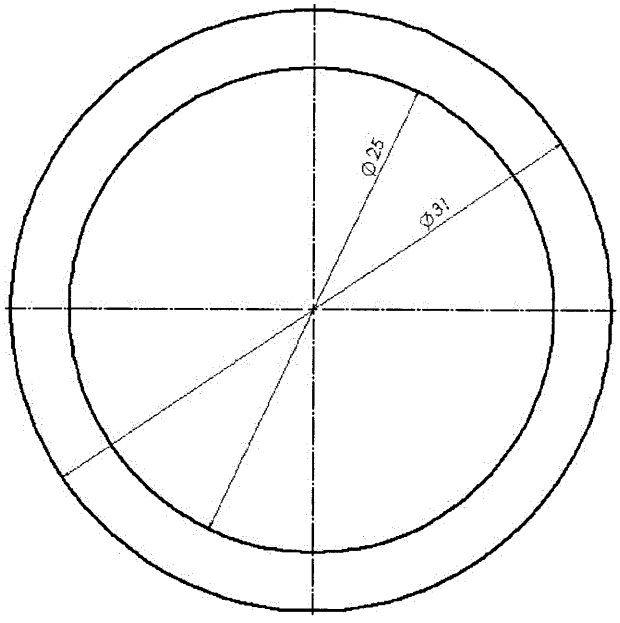
Ø25
Ø31


3

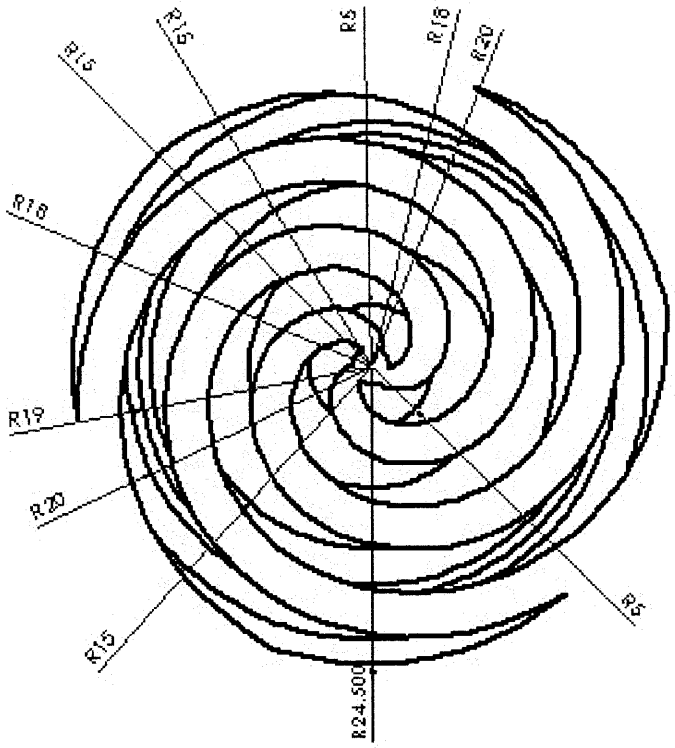


| Modification | Specification |
|---|---|
| Cut 1 | 5,5-$R_{min}$, Top |
| Cut 2 | 10,5,top-1.6 |
| Cut 3 | 15,5,top-3.8 |
| Cut 4 | 18,3,top-5.75 |
| Cut 5 | 19,1,top-6.9 |
| Cut 6 | 20,1,top-6 |

Cut are read: [Outer Radius, Thickness of cut inward, Height of cut] in units of cm
$R_{min}$= 1.5 cm and top=top of the sector (in units of cm)

## D.2 Helium Cyclotron

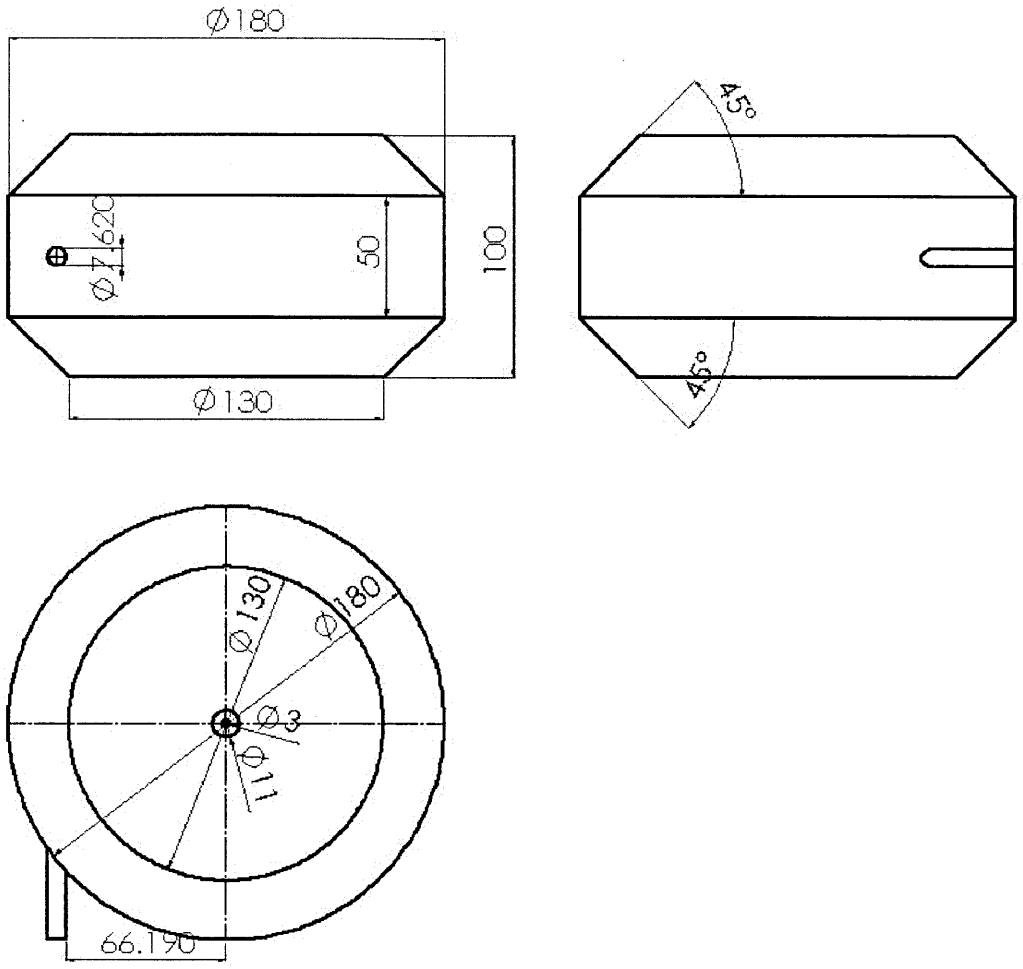

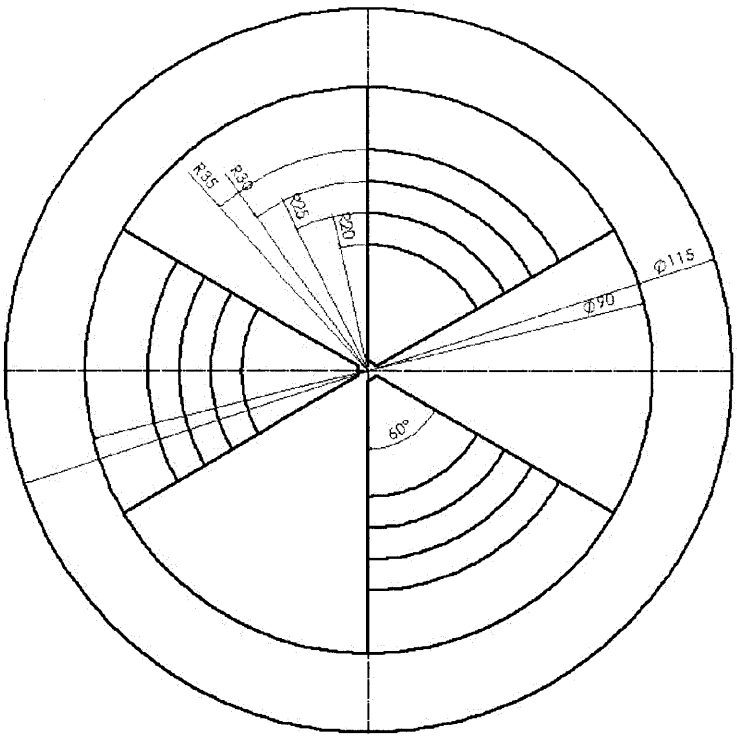
R35
R30
R25
R20
Ø115
Ø90
60°

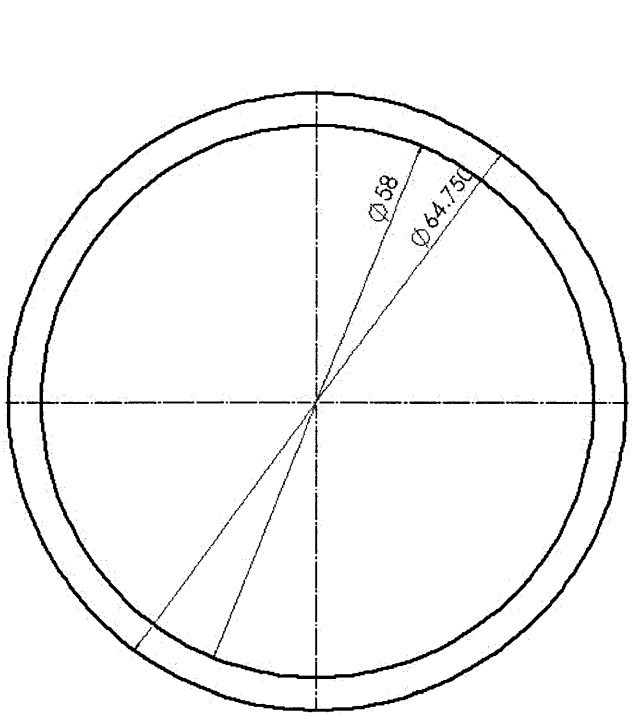
Ø58
Ø64.75
5

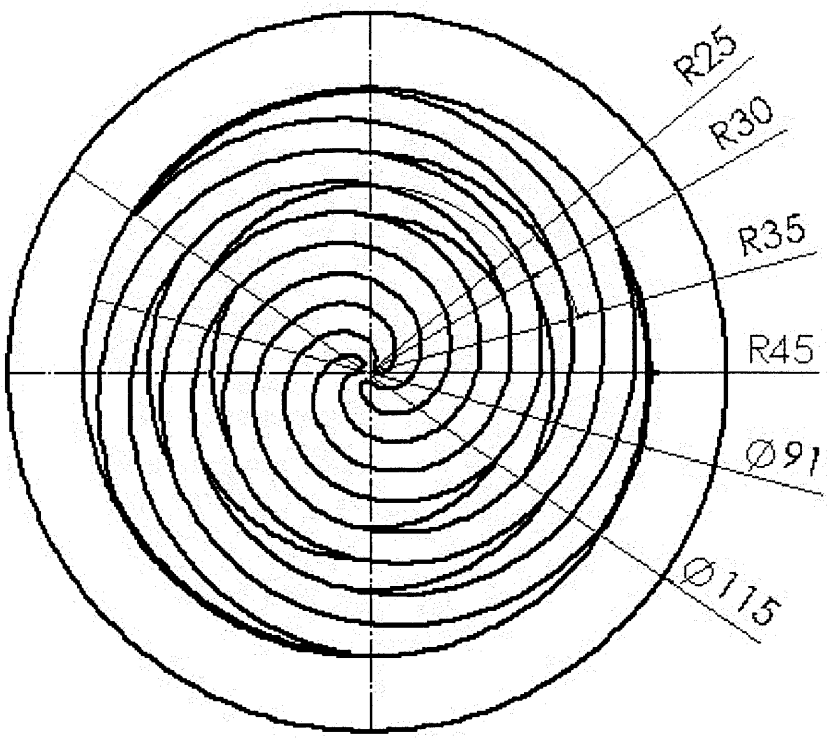


| Modification | Specification |
|---|---|
| Cut 1 | 5,5-$R_{min}$, top |
| Cut 2 | 25,5,top-3.5 |
| Cut 3 | 30,5,top-4.8 |
| Cut 4 | 35,5,top-5.5 |
| Cut 5 | 45.5,10.5,top-6.5 |
| Ring 1 | 57.5,12.5,16,top |

Cut are read: [Outer Radius, Thickness of cut inward, Height of cut] in units of cm
Rings are read: [Radius, Thickness, Height 1, Height 2] in units of cm
$R_{min}$= 1.5 cm and top=top of the sector

# Appendix E: MCNPX Descriptions and Code

## E.1 Descriptions of MCNPX Inputs

The input for MCNPX is patterned after the original punch card system that has not been modified or changed. The learning curve is very steep but MCNPX is a very well known program used by many universities and research labs. Help is readily accessible online. The "punch card" is organized into 5 sections: title, cell, surface, data and anything else. The input card is shown below.

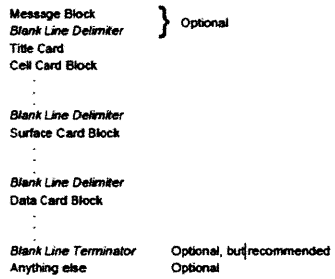


It is important to note that although MCNPX input is not case sensitive, it is highly sensitive to spaces, empty lines, and the placement of characters. Caution must be taking when programming; many characters have duel meanings i.e. 9 can signify the type of particle (proton), the number, the type of tally, or serve as a reference to another cell or surface. It is highly recommended that programs such as VisEd and Xming be used for debugging. These programs offer 3D representation of models and well as 3D particle simulation. 3D models allow for easier geometry checking where as 3D simulation can check source strength, location, and collision path.

MCNPX has a multiple of tallies, functions, conversion, etc for the use of capturing and analyzing data. Their minute details and uses can be found in the MCNPX and MCNP5 manual. A few of the inputs will be briefly defined in the sections below. An understanding of these inputs is needed in order to understand the steps made in the following design process and results sections.

Each time a particle crosses a user specified surface, it is added to the tally [MCNP Primer]. The sum of the particle and their weight (its total contribution) is then reported as the F1 Tally in the MCNPX output. F1 tallies do not make a distinction between the directions of the surface crossing. It is mainly used to verify conservation of energy or to illustrate a distribution of particles.

A point detector tally is similar to a surface tally but it has a built in "next event estimator (NEE)." NEE is a tally of the flux at a point as if the next event were a particle trajectory directly to the detector point without further collision. The proceeding trajectory that is tallied is not the actual particle but a "pseudo particles" of low weight [MCNP VOL1-94]. Pseudo particles allow point detectors tally to have low variance when few actually particles can reach the detector. F5 detectors also assume isotropic scatter for contribution from collision within the model regime. They require the angular distribution data for particles especially when using a Surface Source Write/Read input.

The SSW card is used to write a surface source file for use in a subsequent MCNPX calculation. SSW card are computational intensive because they store the particles position, direction, and energy. All data and results are stored into a RSSA file that can be read by a Surface Source Read (SSR) card. The SSW card allows programmer to perform one computational intensive model and then reference it in later code more quickly than starting from the initial source parameters. SSW cards are written only with respect to a specified surface. Symmetrical surfaces are advised as computational time will be reduced. Referenced surface also cannot be surfaces from marcobodies.

The Surface Source Read card purpose is to read the SSW output file. With the SSR card, one can select the particles to follow, assign a distribution, transpose the source on to a similar surface, and increase the number of particles. By selecting a number greater than the starting number of particle histories (nps), every track stored in the SSW output is then doubled. A number less than the starting nps will reduce a number of the particles. The larger the value of nps on the SSR card will decrease the tally errors until the weight variance contained on the RSSA file dominates [MCNP vol2-75]..Therefore if the SSW file does not contain enough particles to begin with the tally error can never improve beyond a certain point.

Importances are user defined numerical values that define the particle's worth based on its position for the MCNPX program. If a particle is in a area of high importance, MCNPX will spend more computational time following the particle than if it was in a less importance. An importance of zero terminates the problem.

A few common variance reduction techniques that were utilized in the code were geometry splitting, Russian roulette, energy cutoff and the use of point detector tallies. Geometry splitting is the process of sectioning the geometry and increasing the weight of their importance as it approaches the tally [MCNP vol1]. Increasing the importance of a cell speeds up computation time by only following the particles in location that are important to the specific calculation. Russian roulette can then be used when there is a gradient between two cell importances. If particles are

travelling from high to low importance, some of them will terminated from the run, with the assumption that they will probably contribute little to the desire problem result. If particles travel from a low to high importance some of them will be split into two or more particles, each with less weight. In both cases the total weight is conserved. Energy cutoff is applied to particles whose energy is out of range of interest. These particles are terminated from the problem and no longer followed to reduce computation time. Point detectors, as stated above, increase the number of particles or pseudo-particles to reach the tally, decreasing variance.

In MNCPX, the only particles recorded, weighted and tracked will be those specified by the user. For the proton cyclotron, the particles tracked were protons, neutrons, and photons. For the helium cyclotron and target chamber, the particles tracked were protons, neutrons, photons, deuterium, tritium, and alphas. For tracking particles, the user must track all particles smaller in mass than the source particle for accurate representation of data. These smaller secondary reactions have a significant influence in the data. For example, excluding alpha particles in the helium cyclotron would eliminate (n, $\alpha$) reactions. Although with each selection of particles, computation time will increase, it is important that all particles smaller in mass than the source particle be inputted. If computation time is an issue, when utilizing the SSR card, the particle type selection (PTY) input can be used to select only the particles of interest.

Source selection is straight forward for both cyclotrons. Both cyclotrons were modeled with a disk source in the beam space at maximum energy. With the source being at maximum energy, it provides a conservative estimate of the dose rate because in reality the particle is speeding up as the radius increases. MCNPS offers methods to vary the intensity with position but these methods couldn't be accomplished due to programming issues. The target chamber was modeled with an incoming beam 1 mm in radius, with a certain direction and position. The design simulated a beam of incoming particles with proper emittances. Since two sources can't be defined at once, the target chamber consisted of separate models for the proton and helium beam that were later added to determine a simultaneous operation.

The material selection is very straight forward in most cases. All data was used in the model was taken from the Compendium of Material Composition. The Compendium offers a wide range of pure metals as well as mixtures and alloys. Pure Iron, Aluminum, and Copper were used for the materials of the cyclotron. The concrete selected for shielding calculations was listed as "ordinary concrete" with a density of 2.3 g/cm$^3$. Its specifications can be seen in the table below.

| Element | Atom Fraction |
|---|---|
| H | 0.022100 |
| C | 0.002484 |
| O | 0.574930 |
| Na | 0.015208 |
| Mg | 0.001266 |
| Al | 0.019953 |
| Si | 0.304627 |
| K | 0.010045 |
| Ca | 0.042951 |
| Fe | 0.006435 |

If a tally is present in the code, the output MCNPX file will contain a tally statistical check table. The table consists of ten different checks to determine whether the tally data is reliable. These checks are based on mean behavior, relative error, variance of the variance, and figure of merit. The results of each check are marked by a "yes" for pass and "no" for failure. These checks do not guarantee the absolute reliability of the tally, but they assist in identifying tallies that have not been sampled well [MCNPX]. An example a table generated from a point detector tally can be seen below. Data generally wasn't accepted unless it has passed 9 of 10 statistics.

| tfc bin behavior | --mean-- behavior | ---------relative error--------- value | decrease | decrease rate | ----variance of the variance----- value | decrease | decrease rate | --figure of merit-- value | behavior | -pdf- slope |
|---|---|---|---|---|---|---|---|---|---|---|
| desired | random | <0.05 | yes | 1/sqrt(nps) | <0.10 | yes | 1/nps | constant | random | >3.00 |
| observed | random | 0.09 | yes | yes | 0.42 | yes | yes | constant | random | 2.56 |
| passed? | yes | no | yes | yes | no | yes | yes | yes | yes | no |

Along with the tally statistical table another table consisting of user tallied data is also displayed with its associated variance. Depending on the type of tally MCNPX recommends certain variances in the data. Below is a figure taken from the MCNPX manual specifying the variance need for certain conclusions. Note, for shielding calculations, less than 0.2 or 20% is deemed acceptable [MCNPX].

| Range of R | Quality of the Tally |
|---|---|
| 0.5 to 1.0 | Not meaningful |
| 0.2 to 0.5 | Factor of a few |
| 0.1 to 0.2 | Questionable |
| < 0.10 | Generally reliable |
| < 0.05 | Generally reliable for point detectors |

MCNPX provides a "macrobody" capability along with other coding shortcuts to limit the amount of code. Marcobodies allow the users to program reference preset geometric shapes in MCNPX rather than defining a shape by the use of planes. Other coding shortcuts such as "like # but #" allow for code to be repeated without inserting new lines. These shortcuts should be avoided for

the most applications. Macrobodies, although quick and easy to use, can't be used in conjunction with many important MCNPX input such as SSW and SSR and a majority of the tallies. The coding shortcuts slow computation and are not worth a few minutes it saves programming the punch card.

Simplicity is important for MCNPX programming. Unlike today's CAD programs, it is difficult to create detailed designs in MCNPX quickly and accurately. MCNPX's surface card is not limited on the number of surfaces or their shape; the issue arises when trying to define cells. Unlike other programs, MCNPX must have all space defined, including voids. This is very difficult when you have edges, cliffs, or overlaps. It becomes even more difficult when a space is defined by a few surfaces. How to define cells as well as its nomenclature will not be discussed here but the recommendation is to have a simplified model. Both cyclotrons and parts of the target chamber were slightly simplified in order to reduce the errors MCNPX creates when dealing with splines and facets in air-gaps. The simplifications included the elimination of the air gap around each coil and modeling the pole sectors as a cylinder as opposed to a spiral.

MCNPX, as stated above, tracks all particles selected through all collisions for all energy ranges. Due to the high number of collisions and also number of particles, computation time for a multiple processor computer can take days. Due to poor variance in tallies or data, the number of particles must be increased and other variance reduction techniques must be applied. As expected, computation time increases linearly as the number particles increase. To solve this issue it is recommended to run the code on a multiprocessing cluster. A cluster can reduce calculation time by an order of magnitude, allowing for quicker iterations.

## E.2 Proton Cyclotron Shielding Code

```
just proton cyclotron
c ----------cell card----------
c proton cyclotron
   1    1   -8.92 1 -2  imp:n,h,p=1 $coil proton top
   8    1   -8.92 -31 30 imp:n,h,p=1 $coil proton bottom
   2    2  -7.874 3 -4  imp:n,h,p=1 $bottom yoke proton
   3    1   -8.92 -5  imp:n,h,p=1 $conductor plate proton
  11    0    -34 imp:n,h,p=1 $conductor air gap top
  12    0    -35 imp:n,h,p=1 $conductor air gap bot
   4    2  -7.874 -6 imp:n,h,p=1 $top yoke proton
   9    2  -7.874 -32 imp:n,h,p=1 $bottom yoke proton
   7    2  -7.874 -11 6 imp:n,h,p=1 $sloped edge proton
  10    2  -7.874 -33 32 imp:n,h,p=1 $sloped edge proton bot
  14    2  -7.874 -21 imp:n,h,p=1 $pole top
  15    2  -7.874 -36 imp:n,h,p=1 $pole bot
 141    3  -2.70  -27 26 imp:n,h,p=1 $air gap top, made it AL
 142    3  -2.70  -38 37 imp:n,h,p=1 $air gap bot
c universe
  90    0       ( 33.1:32.3:11.1:6.2:4.1 ) -8 imp:n,h,p=1
  91    0        7 imp:n,h,p=0
  92    4  -2.3 8 -7 imp:n,h,p=1

c ----surface card----------
c proton
   1     rcc 0 0 4 0 0 6.5 24.5  $inner coil radius upper
   2     rcc 0 0 4 0 0 6.5 28.5  $outer coil radius upper
  30     rcc 0 0 -10.5 0 0 6.5 24.5  $inner coil radius bot
  31     rcc 0 0 -10.5 0 0 6.5 28.5  $outer coil radius bot
   3     rcc 0 0 -10.5 0 0 21 28.5  $inner yoke radius
   4     rcc 0 0 -10.5 0 0 21 42  $outer yoke radius
   5     rcc 0 0 -1 0 0 2 28.5  $conductor plate
  34     rcc 0 0 1 0 0 0.5 28.5 $conductor air gap top
  35     rcc 0 0 -1.5 0 0 0.5 28.5 $conductor air gap bot
   6     rcc 0 0 10.5 0 0 12.5 28.5  $ top yoke
  32     rcc 0 0 -23 0 0 12.5 28.5  $ bottom yoke
  11     trc 0 0 10.5 0 0 12.5 42 28.5  $cone for sloped sides top
  33     trc 0 0 -23 0 0 12.5 28.5 42  $cone for sloped sides bot
  21     rcc 0 0 1.5 0 0 9 24.5  $pole radius top
  36     rcc 0 0 -10.5 0 0 9 24.5 $pole radius bot
  26     rcc 0 0 1.5 0 0 2.5 24.5  $air gap top
  27     rcc 0 0 1.5 0 0 2.5 28.5  $air gap top
  37     rcc 0 0 -4 0 0 2.5 24.5 $air gap botom
  38     rcc 0 0 -4 0 0 2.5 28.5 $air gap botom
c concrete
 100      so 45
   7     rpp -400 400 -400 400 -300 300  $outer box proton
   8     rpp -300 300 -300 300 -200 200  $inner box 1m thick proton

mode  n h p
c ----material card-------
m1   29063.              1  $MAT1
     nlib=.70c
     hlib=.70h
     plib=.04p
m2   26054.       -0.0585
     26056.       -0.9175
     26057.       -0.0212
     26058.       -0.0028
     nlib=.70c
     hlib=.70h
     plib=.04p
m3   13027.       -1
     nlib=.70c
     hlib=.70h
     plib=.04p
```

```
m4   1001        -0.022100  $MAT3
     6000        -0.002484
     8016        -0.574930
     11023       -0.015208
     12024.      -0.001000
     12025.      -0.000139
     12026.      -0.000126
     13027       -0.019953
     14028.      -0.281260
     14029.      -0.014226
     14030.      -0.009443
     19039.      -0.009367
     19040.      -0.000001
     19041.      -0.000676
     20040.      -0.041637
     20042.      -0.000277
     20043.      -0.000579
     20044.      -0.000895
     20046.      -0.000001
     20048.      -0.000080
     26054.      -0.000376
     26056.      -0.005804
     26057.      -0.000136
     26058.      -0.000018
     nlib=.70c
     hlib=.70h
     plib=.04p
sdef  pos= 0 0 1.25 axs 0 0 1 ext=0 rad=d1 par=9 erg=36
si1 0 24.5
sp1 -21 1
nps 50000000
c    PHYS:N  30 0 0 -1 -1 0 3
F12:n 8.3
c ----neutron flux to dose (rem/hr) conversion factors
E12  2.50e-8 1.00e-7 1.00e-6 1.00e-5 1.00e-4 1.00e-3
     1.00e-2 1.00e-1 5.00e-1 1.00e+0 2.50e+0 5.00e+0
     7.00e+0 1.00e+1 1.40e+1 2.00e+1
DE12 2.50e-8 1.00e-7 1.00e-6 1.00e-5 1.00e-4 1.00e-3
     1.00e-2 1.00e-1 5.00e-1 1.00e+0 2.50e+0 5.00e+0
     7.00e+0 1.00e+1 1.40e+1 2.00e+1
DF12 3.67e-6 3.67e-6 4.46e-6 4.54e-6 4.18e-6 3.76e-6
     3.56e-6 2.17e-5 9.26e-5 1.32e-4 1.25e-4 1.56e-4
     1.47e-4 1.47e-4 2.08e-4 2.27e-4
F22:p  8.3
c    gamma flux to dose (rem/hr) factors
E22  2.50e-8 1.00e-7 1.00e-6 1.00e-5 1.00e-4 1.00e-3
     1.00e-2 1.00e-1 5.00e-1 1.00e+0 2.50e+0 5.00e+0
     7.00e+0 1.00e+1 1.40e+1 2.00e+1
DE22 .01 .03 .05 .07 .1 .15 .2 .25 .3 .35 .4 .45 .5
     .55 .6 .65 .7 .8 1. 1.4 1.8 2.2 2.6 2.8 3.25 3.75
     4.25 4.75 5. 5.25 5.75 6.25 6.75 7.5 9. 11. 13. 15.
DF22 3.96e-6 5.82e-7 2.9e-7 2.58e-7 2.83e-7 3.79e-7
     5.01e-7 6.31e-7 7.59e-7 8.78e-7 9.85e-7 1.08e-6 1.17e-6
     1.27e-6 1.36e-6 1.44e-6 1.52e-6 1.68e-6 1.98e-6 2.51e-6
     2.99e-6 3.42e-6 3.82e-6 4.01e-6 4.41e-6 4.83e-6 5.23e-6
     5.60e-6 5.80e-6 6.01e-6 6.37e-6 6.74e-6 7.11e-6 7.66e-6
     8.77e-6 1.03e-5 1.18e-5 1.33e-5
F32:n 7.3
c -----neutron flux to dose (rem/hr) conversion factors
E32  2.50e-8 1.00e-7 1.00e-6 1.00e-5 1.00e-4 1.00e-3
     1.00e-2 1.00e-1 5.00e-1 1.00e+0 2.50e+0 5.00e+0
     7.00e+0 1.00e+1 1.40e+1 2.00e+1
DE32 2.50e-8 1.00e-7 1.00e-6 1.00e-5 1.00e-4 1.00e-3
     1.00e-2 1.00e-1 5.00e-1 1.00e+0 2.50e+0 5.00e+0
     7.00e+0 1.00e+1 1.40e+1 2.00e+1
DF32 3.67e-6 3.67e-6 4.46e-6 4.54e-6 4.18e-6 3.76e-6
     3.56e-6 2.17e-5 9.26e-5 1.32e-4 1.25e-4 1.56e-4
     1.47e-4 1.47e-4 2.08e-4 2.27e-4
F42:p  7.3
c    gamma flux to dose (rem/hr) factors
```

```
E42  2.50e-8  1.00e-7  1.00e-6  1.00e-5  1.00e-4  1.00e-3
     1.00e-2  1.00e-1  5.00e-1  1.00e+0  2.50e+0  5.00e+0
     7.00e+0  1.00e+1  1.40e+1  2.00e+1
DE42  .01  .03  .05  .07  .1  .15  .2  .25  .3  .35  .4  .45  .5
      .55  .6  .65  .7  .8  1.  1.4  1.8  2.2  2.6  2.8  3.25  3.75
      4.25  4.75  5.  5.25  5.75  6.25  6.75  7.5  9.  11.  13.  15.
DF42  3.96e-6  5.82e-7  2.9e-7  2.58e-7  2.83e-7  3.79e-7
      5.01e-7  6.31e-7  7.59e-7  8.78e-7  9.85e-7  1.08e-6  1.17e-6
      1.27e-6  1.36e-6  1.44e-6  1.52e-6  1.68e-6  1.98e-6  2.51e-6
      2.99e-6  3.42e-6  3.82e-6  4.01e-6  4.41e-6  4.83e-6  5.23e-6
      5.60e-6  5.80e-6  6.01e-6  6.37e-6  6.74e-6  7.11e-6  7.66e-6
      8.77e-6  1.03e-5  1.18e-5  1.33e-5
```

## E.3 Helium Cyclotron Shielding Code

```
Just helium cyclotron
c -------cell card------------
c helium
   8    1   -8.92 -14 13 imp:n,a,p,d,t=1 $coil helium top
  81    1    -8.92 -141 131 imp:n,a,p,d,t=1 $coil helium bot
   9    2  -7.874 -16 15 imp:n,a,p,d,t=1 $ botom yoke helium
  10    2  -7.874 -17 imp:n,a,p,d,t=1 $conductor plate helium
  11    0        -171 imp:n,a,p,d,t=1 $airgap condutor
  12    0        -172 imp:n,a,p,d,t=1 $airgap conductor
  13    2  -7.874 -18 imp:n,a,p,d,t=1 $top yoke
  14    2  -7.874 -181 imp:n,a,p,d,t=1 $bot yoke
  15    2  -7.874 -19 18 imp:n,a,p,d,t=1 $sloped sides
  16    2  -7.874 -191 181 imp:n,a,p,d,t=1 $sloped sides
  17    2  -7.874 -20 imp:n,a,p,d,t=1 $pole top
  18    2  -7.874 -201 imp:n,a,p,d,t=1 $pole bot
  19    3  -2.70  -23 22 imp:n,a,p,d,t=1 $airgap below coil top
  20    3  -2.70  -231 221 imp:n,a,p,d,t=1 $airgap below coil top
c concrete
  100    0  (16.1 :191.1 :19.1 :18.2 :181.3) -101 imp:n,a,p,d,t=1
  101    4  -2.3    101 -100 imp:n,a,p,d,t=1 $concrete wall helium
  991    0         100 imp:n,a,p,d,t=0

c -----surface card------------
c helium material
   13      rcc 0 0 16 0 0 9 57.5  $inner coil radius top
   14      rcc 0 0 16 0 0 9 65  $outer coil radius top
  131      rcc 0 0 -25 0 0 9 57.5  $inner coil radius bot
  141      rcc 0 0 -25 0 0 9 65  $outer coil radius bot
   15      rcc 0 0 -25 0 0 50 65  $inner yoke radius
   16      rcc 0 0 -25 0 0 50 90  $outer yoke radius
   17      rcc 0 0 -1 0 0 2 65  $conductor plate
  171      rcc 0 0 -1.5 0 0 .5 65  $conductor plate air gap bot
  172      rcc 0 0 1 0 0 .5 65  $conductor plate air gap top
   18      rcc 0 0 25 0 0 25 65  $top yoke
  181      rcc 0 0 -50 0 0 25 65  $bot yoke
   19      trc 0 0 25 0 0 25 90 65  $sloped sides
  191      trc 0 0 -50 0 0 25 65 90  $sloped sides
   20      rcc 0 0 1.5 0 0 23.5 57.5  $pole radius top
  201      rcc 0 0 -25 0 0 23.5 57.5  $pole radius bot
   22      rcc 0 0 1.5 0 0 14.5 57.5  $air gap top
  221      rcc 0 0 -16 0 0 14.5 57.5  $air gap top
   23      rcc 0 0 1.5 0 0 14.5 65  $ air gap top
  231      rcc 0 0 -16 0 0 14.5 65  $ air gap top
c universe
  999      so 100
c concrete
  100      rpp -400 400 -400 400 -300 300  $outer box proton
  101      rpp -300 300 -300 300 -200 200  $inner box 1m thick

mode  n a p d t
c -----material card-------
m1   29063.              1
     nlib=.70c
     plib=.04p
m2   26054.        -0.0585
     26056.        -0.9175
     26057.        -0.0212
     26058.        -0.0028
     nlib=.70c
     plib=.04p
m3   13027.        -1
     nlib=.70c
     plib=.04p
m4   1001          -0.022100
     6000          -0.002484
```

```
     8016        -0.574930
     11023       -0.015208
     12024.      -0.001000
     12025.      -0.000139
     12026.      -0.000126
     13027       -0.019953
     14028.      -0.281260
     14029.      -0.014226
     14030.      -0.009443
     19039.      -0.009367
     19040.      -0.000001
     19041.      -0.000676
     20040.      -0.041637
     20042.      -0.000277
     20043.      -0.000579
     20044.      -0.000895
     20046.      -0.000001
     20048.      -0.000080
     26054.      -0.000376
     26056.      -0.005804
     26057.      -0.000136
     26058.      -0.000018
     nlib=.70c
     plib=.04p
sdef  pos= 0 0 1.55 axs 0 0 1 ext=0 rad=d1 par=34 erg=100
si1 0 57.5
sp1 -21 1
nps 50000000
c    PHYS:N  30 0 0 -1 -1 0 3
F12:n 100.3
c ----neutron flux to dose (rem/hr) conversion factors
E12  2.50e-8  1.00e-7  1.00e-6  1.00e-5  1.00e-4  1.00e-3
     1.00e-2  1.00e-1  5.00e-1  1.00e+0  2.50e+0  5.00e+0
     7.00e+0  1.00e+1  1.40e+1  2.00e+1
DE12  2.50e-8  1.00e-7  1.00e-6  1.00e-5  1.00e-4  1.00e-3
     1.00e-2  1.00e-1  5.00e-1  1.00e+0  2.50e+0  5.00e+0
     7.00e+0  1.00e+1  1.40e+1  2.00e+1
DF12  3.67e-6  3.67e-6  4.46e-6  4.54e-6  4.18e-6  3.76e-6
     3.56e-6  2.17e-5  9.26e-5  1.32e-4  1.25e-4  1.56e-4
     1.47e-4  1.47e-4  2.08e-4  2.27e-4
F22:p  100.3
c     gamma flux to dose (rem/hr) factors
E22  2.50e-8  1.00e-7  1.00e-6  1.00e-5  1.00e-4  1.00e-3
     1.00e-2  1.00e-1  5.00e-1  1.00e+0  2.50e+0  5.00e+0
     7.00e+0  1.00e+1  1.40e+1  2.00e+1
DE22  .01  .03  .05  .07  .1  .15  .2  .25  .3  .35  .4  .45  .5
      .55  .6  .65  .7  .8  1.  1.4  1.8  2.2  2.6  2.8  3.25  3.75
      4.25  4.75  5.  5.25  5.75  6.25  6.75  7.5  9.  11.  13.  15.
DF22  3.96e-6  5.82e-7  2.9e-7  2.58e-7  2.83e-7  3.79e-7
      5.01e-7  6.31e-7  7.59e-7  8.78e-7  9.85e-7  1.08e-6  1.17e-6
      1.27e-6  1.36e-6  1.44e-6  1.52e-6  1.68e-6  1.98e-6  2.51e-6
      2.99e-6  3.42e-6  3.82e-6  4.01e-6  4.41e-6  4.83e-6  5.23e-6
      5.60e-6  5.80e-6  6.01e-6  6.37e-6  6.74e-6  7.11e-6  7.66e-6
      8.77e-6  1.03e-5  1.18e-5  1.33e-5
F32:n 101.3
c ----neutron flux to dose (rem/hr) conversion factors
E32  2.50e-8  1.00e-7  1.00e-6  1.00e-5  1.00e-4  1.00e-3
     1.00e-2  1.00e-1  5.00e-1  1.00e+0  2.50e+0  5.00e+0
     7.00e+0  1.00e+1  1.40e+1  2.00e+1
DE32  2.50e-8  1.00e-7  1.00e-6  1.00e-5  1.00e-4  1.00e-3
     1.00e-2  1.00e-1  5.00e-1  1.00e+0  2.50e+0  5.00e+0
     7.00e+0  1.00e+1  1.40e+1  2.00e+1
DF32  3.67e-6  3.67e-6  4.46e-6  4.54e-6  4.18e-6  3.76e-6
     3.56e-6  2.17e-5  9.26e-5  1.32e-4  1.25e-4  1.56e-4
     1.47e-4  1.47e-4  2.08e-4  2.27e-4
F42:p  101.3
c     gamma flux to dose (rem/hr) factors
E42  2.50e-8  1.00e-7  1.00e-6  1.00e-5  1.00e-4  1.00e-3
     1.00e-2  1.00e-1  5.00e-1  1.00e+0  2.50e+0  5.00e+0
     7.00e+0  1.00e+1  1.40e+1  2.00e+1
```

```
DE42 .01 .03 .05 .07 .1 .15 .2 .25 .3 .35 .4 .45 .5
   .55 .6 .65 .7 .8 1. 1.4 1.8 2.2 2.6 2.8 3.25 3.75
   4.25 4.75 5. 5.25 5.75 6.25 6.75 7.5 9. 11. 13. 15.
DF42 3.96e-6 5.82e-7 2.9e-7 2.58e-7 2.83e-7 3.79e-7
   5.01e-7 6.31e-7 7.59e-7 8.78e-7 9.85e-7 1.08e-6 1.17e-6
   1.27e-6 1.36e-6 1.44e-6 1.52e-6 1.68e-6 1.98e-6 2.51e-6
   2.99e-6 3.42e-6 3.82e-6 4.01e-6 4.41e-6 4.83e-6 5.23e-6
   5.60e-6 5.80e-6 6.01e-6 6.37e-6 6.74e-6 7.11e-6 7.66e-6
   8.77e-6 1.03e-5 1.18e-5 1.33e-5
```

## E.4 Example Target Chamber Shielding Code for Helium

```
Target Chamber
c -------cell---------
1    1   -7.92   -1 imp:n,a,p,d,t,h=1 $target wall side1
2    1   -7.92   -2 imp:n,a,p,d,t,h=1 $target wall side2
3    1   -7.92   -3 imp:n,a,p,d,t,h=1 $target back
4    2   -4.54  -4 imp:n,a,p,d,t,h=1 $titanium window
5    3   -7.87  -5 imp:n,a,p,d,t,h=1$ iron sample 1mm thick
6    4   -.01544       -6 5 imp:n,a,p,d,t,h=1 $helium chamber
7    0          1 2 3 4 5 6 9 10 -12 imp:n,a,p,d,t,h=1 $inside universe
9    1   -7.92   -9 imp:n,a,p,d,t,h=1 $target wall top
10   1   -7.92   -10 imp:n,a,p,d,t,h=1$target wall bottom
11   5   -2.3    -11 12 imp:n,a,p,d,t,h=1 $concrete wall
12   5   -2.3    -13 imp:n,a,p,d,t,h=4 $concrete wall
13   5   -2.3    -14 imp:n,a,p,d,t,h=8 $concrete wall
14   5   -2.3    -15 imp:n,a,p,d,t,h=16 $concrete wall
15   5   -2.3    -16 imp:n,a,p,d,t,h=32 $concrete wall
16   0   -17 imp:n,a,p,d,t,h=64 $concrete wall
8    0          (11.2:11.6:11.1:17.5:11.4:11.3) imp:n,a,p,d,t,h=0

c ------surface--------
1        rpp -35 -27 -35 35 -100 100 $side1
2        rpp 27 35 -35 35 -100 100 $side2
3        rpp -27 27 -27 27 92 100 $back
4        rpp -27 27 -27 27 -100 -99.95 $titanium window
5        rpp -5 5 -5 5 -95 -94.9 $ sample
6        rpp -27 27 -27 27 -99.95 92 $helium box
8        so 120
9        rpp -27 27 -35 -27 -100 100 $side3
10       rpp -27 27 27 35 -100 100 $side4
11       rpp -550 550 -800 800 -335 235 $target chamber out
12       rpp -400 400 -650 650 -185 185 $Target chamber in
13       rpp -550 550 -800 800  235 245
14       rpp -550 550 -800 800 245 285
15       rpp -550 550 -800 800 285 305
16       rpp -550 550 -800 800 305 335
17       rpp -550 550 -800 800 335 345

mode  n a p d t h
c ------ m1 is stainless steel
m1    24000.    -0.190 $ Cr
      25055.    -0.020 $ Mn
      26000.    -0.695 $ Fe
      28000.    -0.095 $ Ni
      nlib=.70c
      hlib=.70h
      plib=.04p
c ---- m2 is titanium
m2    22046.    -.0825
      22047.    -.0744
      22048.    -.7372
      22049.    -.0541
      22050.    -.0518
      nlib=.70c
      hlib=.70h
      plib=.04p
c ------m3 is iron
m3    26054.        -0.0585
      26056.        -0.9175
      26057.        -0.0212
      26058.        -0.0028
      nlib=.70c
      hlib=.70h
      plib=.04p
c ---- m4 is helium at 10mpa
m4    2004.     -1.00
```

```
     nlib=.70c
     hlib=.70h
     plib=.04p
c -----m5 is concrete
m5   1001        -0.022100
     6000        -0.002484
     8016        -0.574930
     11023       -0.015208
     12024.      -0.001000
     12025.      -0.000139
     12026.      -0.000126
     13027       -0.019953
     14028.      -0.281260
     14029.      -0.014226
     14030.      -0.009443
     19039.      -0.009367
     19040.      -0.000001
     19041.      -0.000676
     20040.      -0.041637
     20042.      -0.000277
     20043.      -0.000579
     20044.      -0.000895
     20046.      -0.000001
     20048.      -0.000080
     26054.      -0.000376
     26056.      -0.005804
     26057.      -0.000136
     26058.      -0.000018
     nlib=.70c
     hlib=.70h
     plib=.04p
sdef erg = 100 par = 34 dir = 1 pos = 0 0 -100.5 rad = .3 vec = 0 0 1
nps 10000000
c    PHYS:N  30 0 0 -1 -1 0 3
F12:n 16.5
c -----neutron flux to dose (rem/hr) conversion factors
E12  2.50e-8  1.00e-7  1.00e-6  1.00e-5  1.00e-4  1.00e-3
     1.00e-2  1.00e-1  5.00e-1  1.00e+0  2.50e+0  5.00e+0
     7.00e+0  1.00e+1  1.40e+1  2.00e+1
DE12 2.50e-8  1.00e-7  1.00e-6  1.00e-5  1.00e-4  1.00e-3
     1.00e-2  1.00e-1  5.00e-1  1.00e+0  2.50e+0  5.00e+0
     7.00e+0  1.00e+1  1.40e+1  2.00e+1
DF12 3.67e-6  3.67e-6  4.46e-6  4.54e-6  4.18e-6  3.76e-6
     3.56e-6  2.17e-5  9.26e-5  1.32e-4  1.25e-4  1.56e-4
     1.47e-4  1.47e-4  2.08e-4  2.27e-4
F22:p  16.5
c    gamma flux to dose (rem/hr) factors
E22  2.50e-8  1.00e-7  1.00e-6  1.00e-5  1.00e-4  1.00e-3
     1.00e-2  1.00e-1  5.00e-1  1.00e+0  2.50e+0  5.00e+0
     7.00e+0  1.00e+1  1.40e+1  2.00e+1
DE22 .01  .03  .05  .07  .1  .15  .2  .25  .3  .35  .4  .45  .5
     .55  .6  .65  .7  .8  1.  1.4  1.8  2.2  2.6  2.8  3.25  3.75
     4.25  4.75  5.  5.25  5.75  6.25  6.75  7.5  9.  11.  13.  15.
DF22 3.96e-6  5.82e-7  2.9e-7  2.58e-7  2.83e-7  3.79e-7
     5.01e-7  6.31e-7  7.59e-7  8.78e-7  9.85e-7  1.08e-6  1.17e-6
     1.27e-6  1.36e-6  1.44e-6  1.52e-6  1.68e-6  1.98e-6  2.51e-6
     2.99e-6  3.42e-6  3.82e-6  4.01e-6  4.41e-6  4.83e-6  5.23e-6
     5.60e-6  5.80e-6  6.01e-6  6.37e-6  6.74e-6  7.11e-6  7.66e-6
     8.77e-6  1.03e-5  1.18e-5  1.33e-5
F32:n 12.5
c -----neutron flux to dose (rem/hr) conversion factors
E32  2.50e-8  1.00e-7  1.00e-6  1.00e-5  1.00e-4  1.00e-3
     1.00e-2  1.00e-1  5.00e-1  1.00e+0  2.50e+0  5.00e+0
     7.00e+0  1.00e+1  1.40e+1  2.00e+1
DE32 2.50e-8  1.00e-7  1.00e-6  1.00e-5  1.00e-4  1.00e-3
     1.00e-2  1.00e-1  5.00e-1  1.00e+0  2.50e+0  5.00e+0
     7.00e+0  1.00e+1  1.40e+1  2.00e+1
DF32 3.67e-6  3.67e-6  4.46e-6  4.54e-6  4.18e-6  3.76e-6
     3.56e-6  2.17e-5  9.26e-5  1.32e-4  1.25e-4  1.56e-4
     1.47e-4  1.47e-4  2.08e-4  2.27e-4
```

```
F42:p  12.5
c    gamma flux to dose (rem/hr) factors
E42  2.50e-8  1.00e-7  1.00e-6  1.00e-5  1.00e-4  1.00e-3
     1.00e-2  1.00e-1  5.00e-1  1.00e+0  2.50e+0  5.00e+0
     7.00e+0  1.00e+1  1.40e+1  2.00e+1
DE42 .01  .03  .05  .07  .1  .15  .2  .25  .3  .35  .4  .45  .5
     .55  .6  .65  .7  .8  1.  1.4  1.8  2.2  2.6  2.8  3.25  3.75
     4.25  4.75  5.  5.25  5.75  6.25  6.75  7.5  9.  11.  13.  15.
DF42 3.96e-6  5.82e-7  2.9e-7  2.58e-7  2.83e-7  3.79e-7
     5.01e-7  6.31e-7  7.59e-7  8.78e-7  9.85e-7  1.08e-6  1.17e-6
     1.27e-6  1.36e-6  1.44e-6  1.52e-6  1.68e-6  1.98e-6  2.51e-6
     2.99e-6  3.42e-6  3.82e-6  4.01e-6  4.41e-6  4.83e-6  5.23e-6
     5.60e-6  5.80e-6  6.01e-6  6.37e-6  6.74e-6  7.11e-6  7.66e-6
     8.77e-6  1.03e-5  1.18e-5  1.33e-5
```

# Appendix F: Transport Code

## F.1 Proton Beam Transport Code

```
/Proton Beam/
(Tyler Sordelet)
0

16. 22. 200000; (max no of iterations)
16. 3.0 1 ; (mass of proton)
16. 7.0 .1667 ; (k1 finge)
16. 8.0 3.8 ; (k2 fringe)
13. 48. ; (dipole bends in deg)

(Beam entry)
1. 0.2 5 0.2 5 0.0 0.03 0.036 /BEAM/ ; (36mev proton beam)

3.0 .3 /D1/ ; (mand Drift Space)

5.110 0.23 .2 3.81 /Q1/;(Quad 1)

3. .2 /D2/ ; (Drift Space between quads 1 and 2)

5.110 0.2 -.1 3.81 /Q2/; (Quad 2)

3.0 .2 /D3/ ; (mand Drift Space so it doesn't hit concrete )

10. 0. 0. 3 1.5 ; (system length constraint in meters)

3.0 1.9 /D4/ ; (Drift Space thru concrete to bend)

2.1 15. ;
4.00 .500 60 0 ; (bending magnet for proton)
2.1 15. ;

(-----common space for both beams-----)

3.0 .2 /D5/ ; (mand Drift Space)

5.110 0.3 .8 3.81 /Q3/; (Quad 3)

3.1 0.2 /D6/ ; (Drift Space between quads 3 and 4)

5.110 0.3 -.5 3.81 /Q4/; (Quad 4)

3.1 .2 /D7/ ; (Drift Space)

10. 0. 0. 6. 2. ; (system length constraint in meters)

10. 1 1 .5 .001 'F3' ; (fit x in this parm)
10. 3 3 .2 .001 'F4' ; (fit y in this parm)


SENTINEL
/*PLOT*/
-1
SENTINEL
SENTINEL
```

## F.2 Helium Beam Transport Code

```
/Helium Beam/
(Tyler Sordelet)
0

16. 22. 200000; (max no of iterations)
16. 3.0 4 ; (mass of helium)
16. 7.0 .1667 ; (k1 finge)
16. 8.0 3.8 ; (k2 fringe)
13. 48. ; (dipole bends in deg)

(Beam entry)
1. 0.2 5 0.2 5 0.0 0.03 0.100 /BEAM/ ; (100 mev he beam)

3.1 1 /D1/ ; (Drift Space)

5.110 0.2 1.0 3.81 /Q1/;(Quad 1)

3. 0.16 /D2/ ; (Drift Space between quads 1 and 2)

5.110 0.2 -.01 3.81 /Q2/; (Quad 2)

3. .1 /D3/ ; (Drift Space so quad doesn't hit wall)

10. 0. 0. 1. .5 ; (system length constraint in meters)

(------concrete wall begins--------)

3. 1.7 /D4/ ; (mand Drift Space thru concrete)

(------concrete wall ends 1.5 meters later---------)

3. .3 /D5/ ; (thru dipole)

(-----copy from proton --------)

3. 0.2 /D6/ ; (Drift Space)

5. 0.30 0.10326 3.81 /Q5/; (Quad 3)

3. 0.1904 /D7/ ; (Drift Space between quads 3 and 4)

5. 0.2239 -.37080 3.81 /Q6/; (Quad 4)

3. .20 /D8/ ; (Drift Space)

10. 1 1 .5 .001 'F3' ; (fit x in this parm)
10. 3 3 .2 .001 'F4' ; (fit y in this parm)


SENTINEL
/*PLOT*/
-1
SENTINEL
SENTINEL
```

# Appendix G: Poisson Code

## G.1 Dipole

```
Dipole for MMTF

; Copyright 2004, Massachusetts Institute of Technology
; Unauthorized commercial use is prohibited.

&reg kprob=0,          ; Poisson or Pandira problem
mode=0,               ; Use internal table for material 2
mat=1,                ; First region is material air
nbslo=1,              ; Neumann boundary condition on lower edge
nbsup=0,              ; Dirichlet boundary condition on upper edge
nbslf=0,              ; Dirichlet boundary condition on left edge
nbsrt=0,              ; Dirichlet boundary condition on right edge
icylin=1,             ; cylindrical symmetry
ienergy=1,            ; calculate the stored energy
;ktop=60,             ; Field interpolation at 4 points along X
;ltop=3,              ; Field interpolation at 3 points along Y
;xminf=0,xmaxf=12.5,     ; X range for field interpolation
;yminf=0,ymaxf=0.5,      ; Y range for field interpolation
dx=0.2 &              ; X mesh size for problem and dy set off dx

&po x=0.,y=0. &     ; Entire geometry is air, initially
&po x=80.,y=0. &
&po x=80.,y=28. &
&po x=0.,y=28. &
&po x=0.,y=0. &

&reg mat=2, mtid=0 & ;yoke iron
&po x=35.,y=0. &
&po x=40.,y=0. &
&po x=40.,y=7.08 &
&po x=44.,y=7.08 &
&po x=44.,y=4. &
&po x=52.,y=4. &
&po x=52.,y=7.08 &
&po x=56.,y=7.08 &
&po x=56.,y=0. &
&po x=61.,y=0. &
&po x=61.,y=15. &
&po x=35.,y=15. &
&po x=35.,y=0. &

&reg mat=1,cur=-8400 &     ; inner coil
&po x=40.,y=2.0 &
&po x=44.,y=2.0 &
&po x=44.,y=7.08 &
&po x=40.,y=7.08 &
&po x=40.,y=2.0 &

&reg mat=1,cur=8400 &     ; outer coil
&po x=52.,y=2.0 &
&po x=56.,y=2.0 &
&po x=56.,y=7.08 &
&po x=52.,y=7.08 &
&po x=52.,y=2.0 &
```

## G.2 Quadrupole

```
Quad for mTTF

; Copyright 2004, Massachusetts Institute of Technology
; Unauthorized commercial use is prohibited.

&reg kprob=0,
mode=0
dx=.05,dy=.05,        ; Mesh intervals
yminf=0,ymaxf=0       ; Fixed Y for field interpolation
xminf=0,xmaxf=12.85   ; X range for field interpolation
;; The next 6 terms refer to the harmonic analysis:
ktype=4,              ; Quadrupole symmetry
nterm=10,             ; Number of coefficients
nptc=10,              ; Number of arc points for interpolation
rint=1.9,             ; Radius of the arc for interpolation
angle=45,             ; Angular extent of arc (default start = 0)
rnorm=1.0 &           ; Aperture radius for normalization

&po x=0.0,y=0.0 &
&po x=13.,y=0.0 &
&po x=13.,y=13. &
&po x=0.0,y=0.0 &

&reg mat=2,mtid=0 &
&po x=2.694,y=2.694 &
&po x=3.11,y=2.3 &
&po x=4.0,y=1.9 &
&po x=4.70,y=1.7 &
&po x=6,y=1.4 &
&po x=6.72,y=1.41421 &      ;start outline for coil
&po x=9.548,y=4.24264 &
&po x=10.9622,y=2.8284&
&po x=10.9622,y=0.0  &
&po x=13,y=0.0 &
&po x=13.,y=10. &
&po x=11, y=11. &
&po x=2.694,y=2.694 &

&reg mat=1,cur=2350. &
&po x=6.72,y=1.41421 &      ;start outline for coil
&po x=9.548,y=4.24264 &
&po x=10.9622,y=2.8284&
&po x=8.134,y=0.0 &
&po x=6.72,y=1.41421 &

&reg ibound=0 &
&po x=13.,y=13. &
&po x=2.694,y=2.694 &
&po x=0.0,y=0.0 &
```